Development of a transient CFD methodology for the optimization of CNG engines

Master thesis

R. Maselis

Delft University of Technology

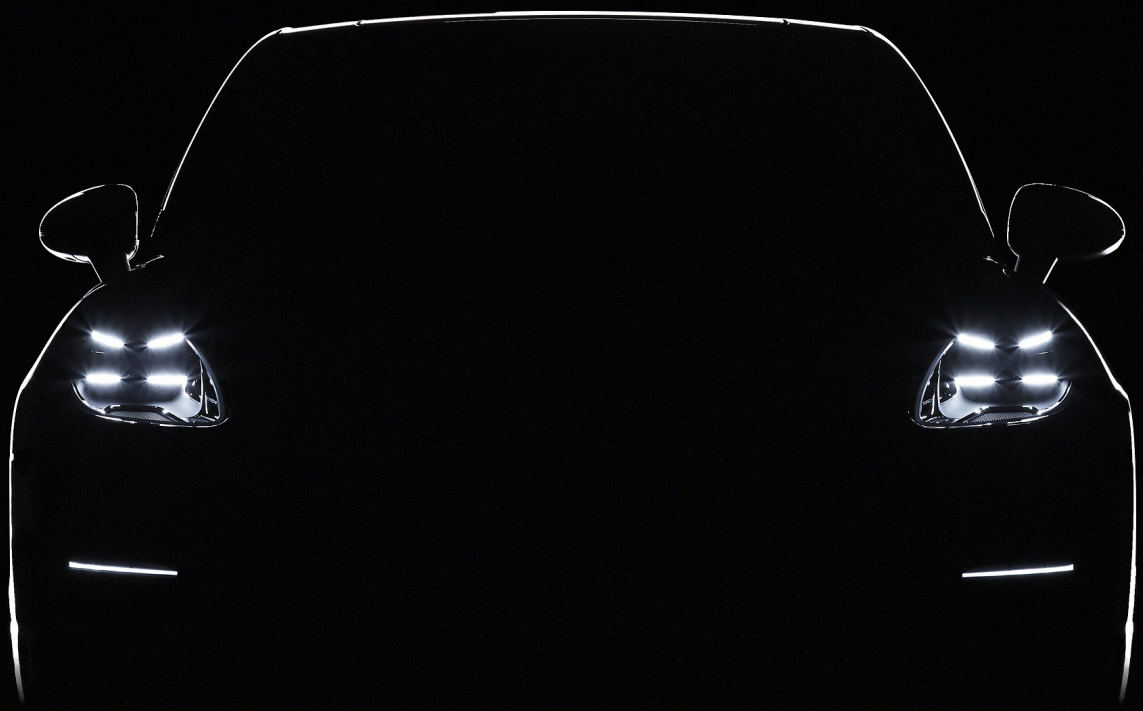

TU Delft

Porsche Engineering
driving technologies

Development of a transient CFD methodology for the optimization of CNG engines

by

R. Maselis

to obtain the degree of Master of Science
at the Delft University of Technology,
to be defended publicly on Friday February 15, 2019 at 14:00.

Student number: 4278224

Supervisors:	Prof. Dr.-Ing. habil. S. Hickel	Delft University of Technology
	Dipl. Ing. M. Böger	Porsche Engineering Services
	Dipl. Ing. V. Bevilacqua	Porsche Engineering Services

TU Delft

Confidentiality clause

This master thesis contains information that is not intended for publishing. All rights to the master thesis, including distribution on electronic media, belong to Porsche Engineering Services GmbH.

In exceptional circumstances and with the explicit written permission of Porsche Engineering Services GmbH, the contents of the master thesis may be passed on to third parties during a barring period of 5 years from the date of submission. After expiration of the barring period, this approval is no longer required.

Sperrklausel

Die vorliegende Masterarbeit enthält zum Teil Informationen, die nicht für die Öffentlichkeit bestimmt sind. Alle Rechte an der Masterarbeit einschließlich der Verbreitung auf elektronischen Medien liegen bei der Porsche Engineering Services GmbH.

Abweichend hiervon darf der Inhalt der Masterarbeit während einer Sperrzeit von 5 Jahren ab dem Abgabedatum mit der ausdrücklichen schriftlichen Genehmigung der Porsche Engineering Services GmbH an Dritte weitergegeben werden. Nach Ablauf der Sperrzeit ist diese Genehmigung nicht mehr erforderlich.

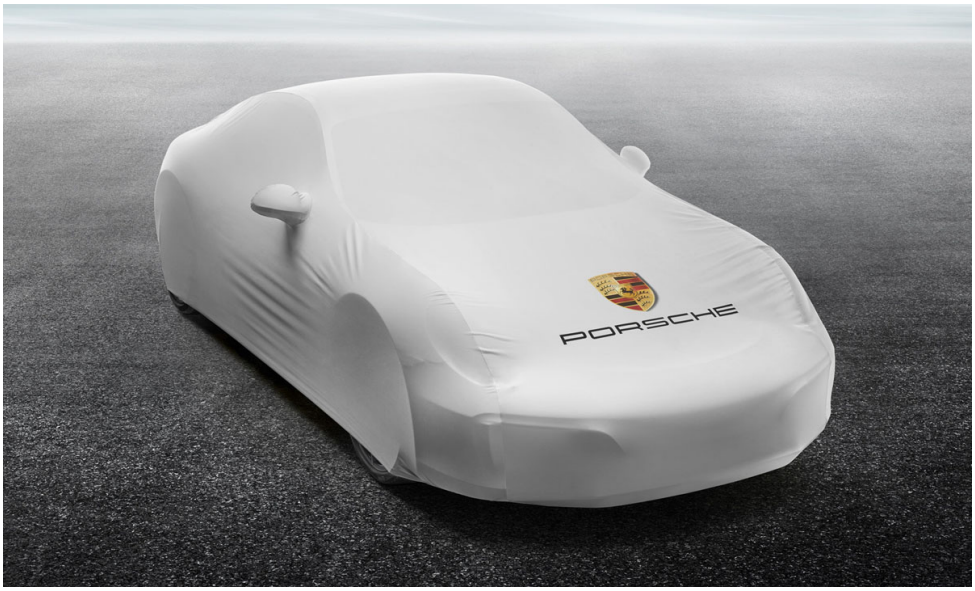

DELFT UNIVERSITY OF TECHNOLOGY
DEPARTMENT OF AERODYNAMICS

The undersigned hereby certify that they have read and recommend to the Faculty of Aerospace Engineering for acceptance the thesis entitled **"Development of a transient CFD methodology for the optimization of CNG engines"** by **Robbe Maselis** in fulfillment of the requirements for the degree of **Master of Science**.

Dated: February 15, 2019

Prof. Dr.-Ing. habil. Stefan Hickel

Dr. ir. Sander van Zuijlen

Dr. ir. Matteo Pini

Preface

This report is the final deliverable of my graduate program in aerospace engineering at the Delft University of Technology. It is the result of a nine-month period that I devoted to a literature study and research about the computational fluid dynamics (CFD) modeling of internal combustion engines.

The project has been carried out in cooperation with the engine simulation department at Porsche Engineering Services GmbH in Bietigheim-Bissingen, Germany. The main objective of the work was to develop a predictive CFD tool for the simulation of the in-cylinder flow in a four-stroke Compressed Natural Gas (CNG) engine. All simulations were carried out in CONVERGE (version 2.4), a software package renowned for its automated immersed-boundary mesh generation and powerful features for combustion engine simulations.

The automotive industry mainly focuses on simulation methods that are easy to implement and maintain, and the projects are usually characterized by the desire to have results in the minimum amount of time and cost. This is in contrast to the academic world, where the projects find themselves on the cutting edge of technology, and the (computational) resources limit to a lesser extent the research that is being conducted. This project bridged the gap between state-of-the-art research and the industrial implementation.

Robbe Maselis
Delft, February 2019

Acknowledgements

First and foremost, I would like to thank Porsche Engineering Services GmbH for giving me the opportunity to write my thesis at the company and for providing me with the necessary resources to carry out my research. Furthermore, I am grateful to my direct supervisors, Vincenzo Bevilacqua and Matthias Böger, for introducing me to the interesting project and sharing their knowledge with me, as well as to my university supervisor, Prof. Dr.-Ing. habil. Stefan Hickel, for providing me with useful theoretical feedback when I needed it.

Thank you, Alessandro, for your assistance in the thesis and for showing so much interest in my work. Thank you, Giovanni, David, Michal, Zio, Frateta, Christoph, Paul, Luca and Johannes; without you I would not have enjoyed my time at the company as much.

Finally, I would like to thank my family, for their never-ending support not only during this thesis, but throughout my entire education.

Abstract

Compressed natural gas (CNG) has been gaining attention in the automotive industry since it allows for a substantial reduction in carbon dioxide emissions. Recent advancements in direct-injection technology have contributed to an increase in volumetric efficiency and engine power, but the physical modeling of such gaseous injection with Computational Fluid Dynamics (CFD) is still challenging. This work describes the development of a CFD methodology for the simulation of CNG engines, an evaluates its predictivity by varying certain simulation parameters.

Firstly, turbulence modelling has been investigated by comparing the RNG k-ε RANS, Dynamic Smagorinsky LES and Delayed DES approaches. The DES provides the best trade-off between computational cost and accuracy during fuel injection, but the model makes abrupt transitions between its RANS and LES-like regions, leading to inaccuracies during combustion. The expensive nature of the LES and the adequate accuracy of the RANS model lead to the preference of the latter. Secondly, the turbulent Schmidt number was investigated. By lowering the number, mixing is more dominant in the simulation and the mixture formation becomes more stoichiometric. The influence on combustion is even larger because of turbulent transport across the flame, with extremely low values even leading to falsely-predicted engine knock. Thirdly, by comparing multiple consecutive engine cycles to each other, it was found that the first cycle still contains a large amount of initialization error in the turbulent field. The second and third cycles show much better agreement to each other. Finally, the amount of turbulent fluctuations at peak power and their influence on laminar flame speed partially lead to flame extinction at the start of combustion. As a consequence, the G-equation model is not justified and does indeed provide inaccurate results for the heat release during combustion. Even though the SAGE detailed chemistry solver in conjunction with the Gri-Mech 3.0 mechanism is assumed to have a larger computational cost, it was found that the opposite is in fact true, and the latter should be preferred.

The aforementioned conclusions are used to calibrate the simulation model against measurement data. The recommended settings are the RANS turbulence model, SAGE detailed chemistry and a turbulent Schmidt number of 0.6, while considering results from a second engine cycle. The Lower Heating Value (LHV) of the fuel was decreased in order to account for an unforeseen inconsistency with the measurement. This ad hoc solution showed that the predictivity of the RANS simulations can substantially be improved, and a good agreement between simulation and measurement was observed. The calibration is however not consistent with other operating conditions, as the part load analysis showed. Finally, the comparison between the peak power and part load operating point have revealed that the engine performance can potentially be improved by altering the piston bowl shape or the position of the injector and the spark plug.

Contents

List of Figures

List of Tables

List of Symbols and Abbreviations

Roman symbols

Δ	Cell size	[m]
B	Bore	[m]
c	Progress variable	[−]
c_p	Specific heat capacity	[J/kg-K]
CR	Compression ratio	[−]
D	Molecular diffusivity	[m^2/s]
D_t	Eddy diffusivity	[m^2/s]
E	Total energy	[J]
E_a	Activation energy	[J]
H	Total enthalpy	[J]
k	Reaction rate coefficient	[−]
k	Turbulent kinetic energy	[m^2/s^2]
Ka	Karlovitz number	[−]
L	Integral length	[m]
ℓ	Turbulence length	[m]
l_{cr}	Conrod length	[m]
ℓ_δ	Inner layer thickness	[m]
ℓ_f	Laminar flame thickness	[m]
$\ell_{k\epsilon}$	k-ϵ lengthscale	[m]
p	Pressure	[Pa]
Pr	Prandtl number	[−]
q	Heat flux	[W/m^2]
Q_{net}	Net heat release	[J]
R	Universal gas constant	[J/mol-K]
Re	Reynolds number	[−]
Re_t	Turbulent Reynolds number	[−]
S	Stroke	[m]
S_{ij}	Strain rate tensor	[1/s]
Sc_t	Turbulent Schmidt number	[−]
T	Temperature	[K]
U	Mean velocity	[m/s]
u	Flow velocity	[m/s]
u_L	Laminar burning velocity	[m/s]
u'	Turbulent intensity	[m/s]
V	Volume	[m^3]
w	Chemical reaction rate	[kg/m^3-s]
y^+	Wall unit	[−]
CFL	Courant number	[−]
CH_4	Methane	

Greek symbols

ε	Turbulent dissipation rate	[m^2/s^3]
η	Kolmogorov lengthscale	[m]
γ	Isentropic coefficient	[−]
κ	Polytropic coefficient	[−]
κ	Turbulent wavenumber	[s]
λ	Air-fuel ratio	[−]
ν	Kinematic viscosity	[m^2/s]
ν_t	Turbulent viscosity	[m^2/s]
ρ	Density	[kg/m^3]
σ_{ij}	Viscous stress tensor	[N/m^2]
τ	Vortex turnover time	[s]
τ_c	Chemical timescale	[s]
τ_η	Kolmogorov timescale	[s]
θ	Crank angle	[deg]

Abbreviations

AMR	Adaptive mesh refinement
BDC	Bottom dead center
CFD	Computational fluid dynamics
CFM	Coherent flame model
CNG	Compressed natural gas
CPU	Central processing unit
DDES	Delayed DES
DES	Detached eddy simulation
DI	Direct injection
DNS	Direct numerical simulation
EBU	Eddy break-up
EOI	End of injection
EVC	Exhaust valve closing
EVM	Eddy viscosity model
EVO	Exhaust valve opening
IVC	Intake valve closing
IVO	Intake valve opening
LES	Large Eddy Simulation
LHV	Lower heating value
NGV	Natural gas vehicles
PFI	Port-fuel injection
RANS	Reynolds-Averaged Navier-Stokes
RNG	ReNormalization Group
rpm	Rotations per minute
SAS	Scale adaptive simulation
SGS	Subgrid-scale
SI	Spark ignition
SOC	Start of combustion
SOI	Start of injection
TDC	Top dead center
TKE	Turbulent kinetic energy
URANS	Unsteady RANS

1 Introduction

The stringent requirements for emissions have led to the use of alternative fuels in the automotive industry. One of the most promising solutions is compressed natural gas (CNG), a gaseous fuel that predominantly consists of methane (CH_4). Burning of CH_4 produces up to 25% less CO_2 emissions than regular gasoline engines, thanks to the more favorable ratio of carbon to hydrogen atoms [Seboldt *et al.*, 2016]. Additionally, the very high octane rating makes this fuel attractive in terms of thermal efficiency, since large compression ratios can be obtained before auto-ignition of the fuel or 'knock' is reached [Chala *et al.*, 2017; Choi *et al.*, 2016]. A drawback is that gaseous fuels require a significant amount of space to install a pressurized fuel tank. A commercially available example is provided in Figure 1.1. This makes CNG a good solution for heavy-duty operations, but not yet for regular automobiles. Moreover, the absence of infrastructure and fuel stations (as compared to other fuels) does not attract people to invest in a CNG-fuelled car.

Several studies have shown that the advantages clearly outweigh the drawbacks in the last decades [Khan *et al.*, 2015]. Figures 1.2 and 1.3 show the global increase in natural gas vehicles (NGVs), and the local increase per continent. With an annual growth of more than 16 percent over the last ten years, both the number of NGVs and fuel stations is set to increase further. Other sources stipulate that, especially after the Dieselgate scandal of 2015, people are looking for an environmentally friendly replacement car [Boretti, 2017]. The strongest growth of NGVs is present in Asia, with leading countries including Iran, China and Pakistan. So far, the popularity of CNG has not yet reached the North American and African continents, as their relative contribution to the global growth is less than one percent.

Previous designs of CNG engines mainly use port fuel injection (PFI) systems. A large drawback of PFI is that the air and fuel are already premixed at the moment the mixture is drawn into the combustion chamber. This reduces the volumetric efficiency of the engine, therefore reducing the peak power [Choi *et al.*, 2016; Seboldt *et al.*, 2016]. The more recently developed direct-injection (DI) strategy circumvents this drawback by taking in fresh air only, and injecting the fuel directly into the cylinder, resulting in a higher volumetric efficiency and a better driveability. In addition, the density of gaseous CNG is much lower compared to liquid fuels such as gasoline. The penetration of the fuel jet is thus largely affected and the loss of momentum needs to be compensated to preserve the optimal amount of fuel. A novel solution is the outward-opening injector, which, similarly to a valve for air intake, opens towards the piston [Seboldt *et al.*, 2016]. The contact area between the fuel and the combustion chamber is thus much larger, allowing a larger injected fuel mass. Despite this solution, it is still challenging to apply rich-burn strategies to CNG engines, such that they operate mostly at stoichiometric conditions.

Experimental studies for CNG are still scarce since the gaseous state makes flow visualization difficult. In the last decades, Computational Fluid Dynamics (CFD) has emerged as an efficient tool to perform preliminary analyses of combustion cycles. Nevertheless, the highly turbulent nature of the flow field after injection poses challenges towards the physical modeling of the engine cycle, as

Figure 1.1: Typical size and position of a pressurized CNG tank, from NGV Depot [2018]

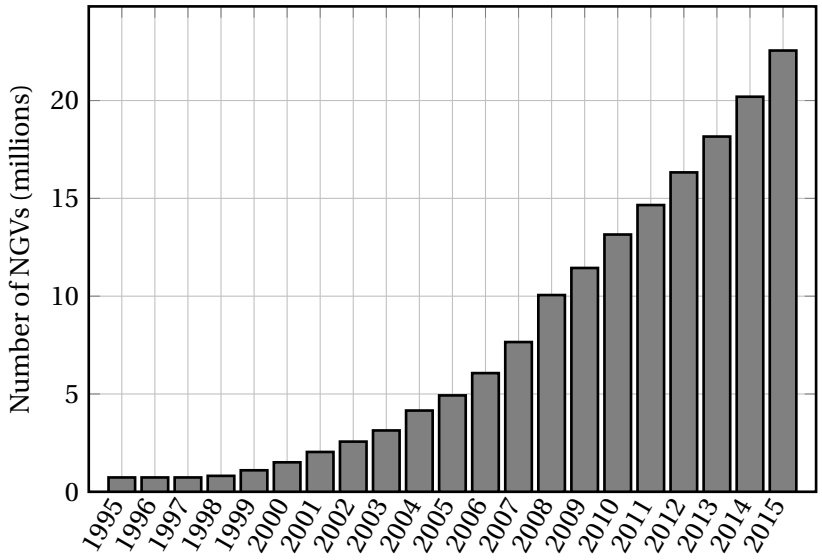

Figure 1.2: Worldwide growth of natural gas vehicles, adapted from Khan *et al.* [2015]

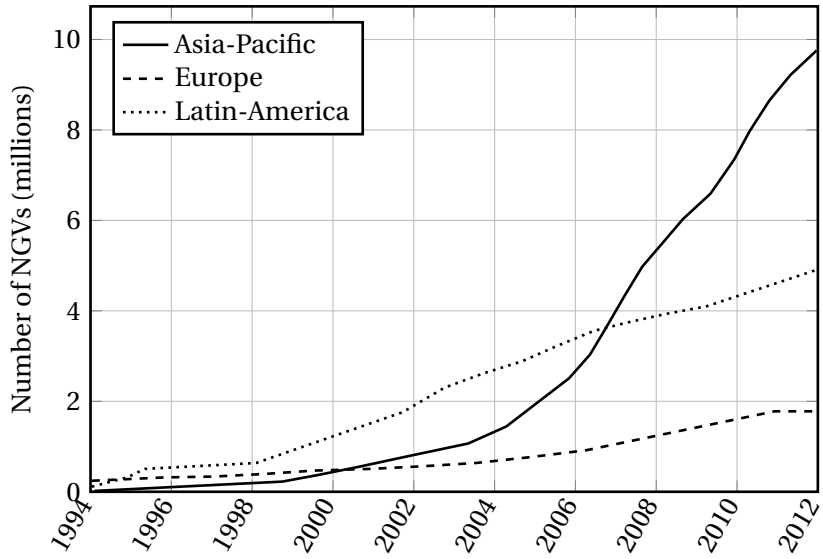

Figure 1.3: Worldwide growth of natural gas vehicles per region, adapted from Khan *et al.* [2015]

fine grids are needed to capture the small-scale dissipative structures, and appropriate models for turbulence and combustion have to be selected. The aim of this project is therefore to set up and evaluate a predictive and computationally efficient engine cycle simulation in the solver CONVERGE. The project uses a practice-oriented approach, in which the focus lies on testing different turbulence and combustion models, validating the simulations with measurement data, and evaluating the sensitivity of global simulation parameters on the predictivity of the model for two operating points.

The report is structured as follows. First, Chapter 2 touches upon the most essential concepts of turbulence and combustion modeling. It gives an overview of the most popular models, the theory behind them and the latest findings in the scientific community. Next, Chapter 3 discusses the development of the simulation methodology that is used to model the engine. The chapter includes an overview of the case set-up, the calibration process with experimental data and a grid convergence study. Furthermore, the turbulence and combustion models that are deemed relevant for this case setup are introduced, and the individual settings for each model are given. The results of the simulations are subsequently presented in Chapter 4, where the sensitivity of several simulation parameters is analyzed. The conclusions to the report are given in Chapter 5, and some notable recommendations are included for researchers who wish to continue the project or start a similar one.

2

Literature study

The present chapter gives a brief overview of the theory and the current state-of-the-art regarding internal combustion engine simulation, with an emphasis on turbulent combustion modeling. Section 2.1 starts by defining the basic concepts of turbulence and which motions are involved. Section 2.2 elaborates the discussion in terms of the physical modeling of those scales with CFD. Subsequently, the basics of combustion modeling are presented in Section 2.3. Here, merely an overview of the relevant combustion and chemistry models is given, without going into detail on the combustion phenomenon or the physics behind it. The claims from literature are summarized in Section 2.4 and used to motivate the scientific relevance of the current project.

2.1 Turbulent motion in internal combustion engines

Turbulence is a chaotic, unsteady, three-dimensional phenomenon that results from instabilities in a flow field. Since 'instabilities' are hard to define, the Reynolds number

$$Re = \frac{u\ell}{\nu} \tag{2.1}$$

is often used to demarcate the difference between a laminar or a turbulent flow. The non-dimensional number can be regarded as the ratio between intertial forces (velocity u) and viscous forces (kinematic viscosity ν). If the Reynolds number is larger than a certain problem-dependent value, the flow may encounter instabilities and make its transition to the turbulent regime.

In a fully turbulent flow field, the instantaneous flow velocity u at a particular point location and a given moment of time can be decomposed into a mean component U and a random turbulent fluctuation u':

$$u = U + u'. \tag{2.2}$$

The turbulent flow field contains coherent vortices or 'eddies' of different sizes that each have a characteristic velocity, length and turnover time, related to each other by

$$u = \frac{\ell}{\tau}. \tag{2.3}$$

The largest scales of the flow, also referred to as the integral scales, contain the majority of the turbulent kinetic energy and have an anisotropic nature [Pope, 2000]. They determine the global motion of the flow field in the combustion chamber, and are mainly produced by tumble or swirl during the intake event. The integral scales are characterized by the integral length L and the integral time T. The velocity is comparable to the mean flow velocity U.

The smaller eddies are responsible for the majority of the dissipation on molecular level. The main characteristics of the small eddies are based on the theory of Kolmogorov [1941], saying that

the small scales are statistically isotropic and are uniquely determined by the dissipation rate [Pope, 2000]. The eddies are thus independent of viscosity and are similar for all high-Reynolds number velocity fields.

A typical turbulent kinetic energy (TKE) spectrum for an internal combustion engine is presented in Figure 2.1. The abscissa represents the wavenumber of a particular eddy, defined as

$$\kappa = \frac{2\pi}{\ell}. \tag{2.4}$$

The integral scales and Kolmogorov scales of the flow are connected by the inertial subrange, where the turbulence undergoes a decay of energy over time, with a reduction of size as a consequence. According to Kolmogorov's theory, the turbulent kinetic energy decays with a slope of $\kappa^{-5/3}$ when the turbulence is isotropic and thus statistically similar. As this is hardly ever the case in automotive engines due to the large amount of turbulence production, the graph shows a slight deviation from the theoretical standpoint.

It is useful to define the wavenumbers (or consequently the lengthscales) that separate the energy-containing integral scales from the statistically isotropic inertial subrange. According to Pope [2000], the demarcation is given by

$$\ell_{\mathrm{EI}} \approx \frac{1}{6} L, \tag{2.5}$$

where E stands for energy-containing and I for inertial subrange. This relation is used in Section 3.4 to define the proper grid size for the turbulence models.

The particular difficulty in the modeling of turbulence in 3D is due to the non-linearity of the convection term in the Navier-Stokes equations, representing the interaction between the integral and Kolmogorov scales. While the majority of the energy is passed from large to small scales through the energy cascade process, the interaction between wavenumbers can cause a 'backscatter' of energy towards the larger scales. The turbulence model should therefore capture enough small scale dissipation in order to model the effect on the large eddies in the flow.

Turbulence is a desirable feature for direct-injection engines, as large turbulent structures promote mixing of the air and the fuel prior to the combustion. Also the turbulent flame speed is largely determined by the motion of the eddies. Turbulent flames propagate faster than laminar ones and the dissipative nature of the vortices causes a more dominant heat transfer with the surroundings [Peters, 2000]. Excessive turbulence can however extinguish the flame.

2.2 Turbulence modeling

Over the last decades, three main methods have emerged for the solution of turbulent flows. The most accurate methods currently available are direct numerical simulations (DNS). They can provide a fully resolved flow field, including the Kolmogorov scales of the flow. The computational cost of this solution method however scales with Re^3 for three-dimensional unsteady simulations [Pope, 2000]. During the intake and injection events, the flow field in high-performance engines can reach velocities up to 300 meters per second, leading to very large Reynolds numbers, thus implying that a practical implementation is hardly possible in industry. Until a sufficient amount of computational resources is available for DNS, the automotive industry tends to focus more on simple turbulence models that require less time, often leading to a loss of accuracy.

In the next three subsections, two simplified modeling approaches are introduced, followed by a hybrid approach that combines both methods. For each approach, a short theoretical description is given, followed by an overview of the state-of-the-art of turbulence modeling in engines.

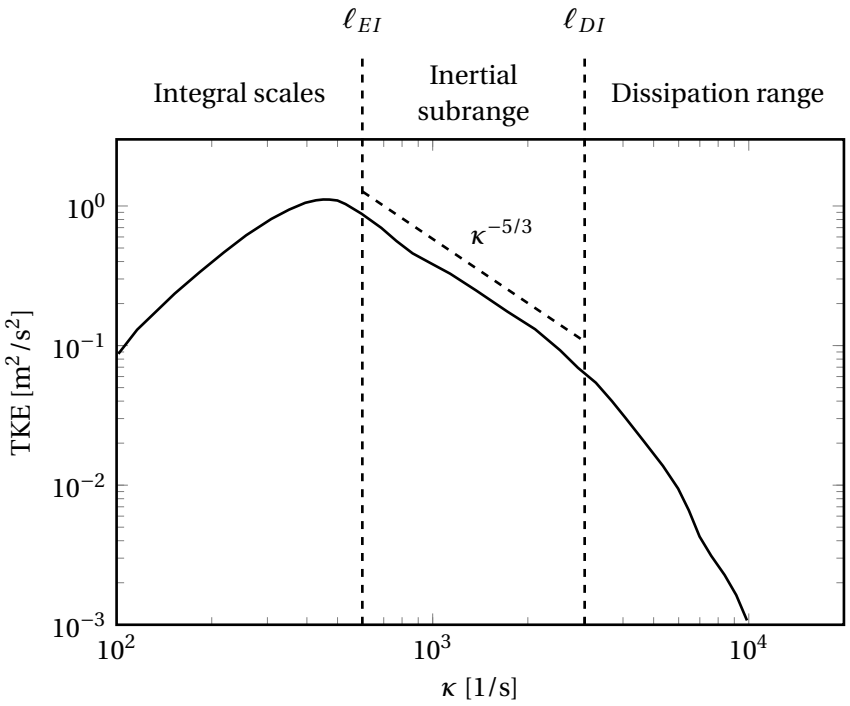

Figure 2.1: Typical kinetic energy spectrum for the intake stroke of an internal combustion engine at part load, adapted from Catania *et al.* [1996]

2.2.1 Reynolds-Averaged Navier-Stokes

Originally introduced by Osborne Reynolds, the Reynolds-Averaged Navier-Stokes (RANS) approach describes the mean velocity component of the flow as an ensemble-averaged solution [Reynolds, 1895]. The corresponding unsteady RANS (URANS) equations are derived by substituting Equation (2.2) into the compressible[(1)] Navier-Stokes equations and once again ensemble-averaging, such that the mass, momentum and energy conservation laws in Equations (2.6a) to (2.6c) are obtained [Gatsky and Bonnet, 2009]:

$$\frac{\partial \overline{\rho}}{\partial t} + \frac{\partial}{\partial x_i}\left(\overline{\rho}\widetilde{u}_i\right) = 0, \tag{2.6a}$$

$$\frac{\partial}{\partial t}\left(\overline{\rho}\widetilde{u}_i\right) + \frac{\partial}{\partial x_j}\left(\overline{\rho}\widetilde{u}_i\widetilde{u}_j\right) = -\frac{\partial \overline{p}}{\partial x_i} + \frac{\partial}{\partial x_j}\Big(\underbrace{\overline{\sigma}_{ij}}_{\substack{\text{viscous}\\ \text{stress}}} - \underbrace{\overline{\rho u_i' u_j'}}_{\substack{\text{Reynolds}\\ \text{stress}}}\Big), \tag{2.6b}$$

$$\frac{\partial}{\partial t}\left(\overline{\rho}\widetilde{E}\right) + \frac{\partial}{\partial x_j}\left(\overline{\rho}\widetilde{u}_j\widetilde{H}\right) = \frac{\partial}{\partial x_j}\Bigg(\widetilde{u}_i\overline{\sigma}_{ij} - \widetilde{u}_i\overline{\rho u_i' u_j'} + \underbrace{\overline{\sigma_{ij}u_i'}}_{\substack{\text{molecular}\\ \text{diffusion}}} - \underbrace{\overline{q}_j}_{\substack{\text{heat}\\ \text{flux}}} - \underbrace{c_p\overline{\rho u_j' T'}}_{\substack{\text{turbulent}\\ \text{heat flux}}} - \underbrace{\frac{1}{2}\overline{\rho u_i' u_i' u_j'}}_{\substack{\text{turbulent}\\ \text{transport}}}\Bigg), \tag{2.6c}$$

where

$$\overline{\sigma}_{ij} \approx 2\widetilde{\mu}\left(\widetilde{S}_{ij} - \frac{1}{3}\frac{\partial \widetilde{u}_k}{\partial x_k}\delta_{ij}\right), \tag{2.7a}$$

$$\widetilde{H} = \widetilde{E} + \frac{\overline{p}}{\overline{\rho}}, \tag{2.7b}$$

$$\overline{q}_j \approx -\frac{c_p\widetilde{\mu}}{Pr}\frac{\partial \widetilde{T}}{\partial x_j}. \tag{2.7c}$$

(1) In internal combustion engines, the induction and compression stroke are characterized by high Reynolds number and high Mach number flows. During gas exchange processes the flow becomes choked for a part of the stroke, especially when operating at high engine speeds [Heywood, 1988].

Note that the time derivative is retained, making the equations unsteady. Definitions and units of the symbols can be found in the list on page xi. In the above system of equations (sometimes also dubbed the Favre-Averaged Navier-Stokes equations due the density weighing) the overbar represents conventional ensemble-averaged variables, while the tilde refers to a density weighted Favre average, defined for an arbitrary flow variable ϕ as

$$\widetilde{\phi}_i = \frac{\overline{\rho\phi_i}}{\overline{\rho}}. \tag{2.8}$$

The unknown turbulent velocity fluctuations that cannot be calculated explicitly appear in Equations (2.6b) and (2.6c) in the terms of Reynolds stress, molecular diffusion, turbulent heat flux and turbulent transport. Nevertheless, most turbulence models only focus on closure of the Reynolds stress tensor $-\overline{\rho u_i' u_j'}$, while the other three are often neglected or modeled using a simple Reynolds analogy [Gatsky and Bonnet, 2009].

It should be noted that, in turbulent flows, the compressibility of turbulent fluctuations can be judged by evaluating the fluctuating Mach number of the flow. It was observed by Spina *et al.* [1994] that, for zero-pressure gradient adiabatic boundary layers, the compressibility effects of the turbulence remain unimportant ($M' < 0.3$) until a freestream Mach number of 4 is obtained. It will become clear in the remainder of this report that the fuel jet coming from the injector reaches very large, locally supersonic velocities. The Mach number reaches maximum local values of 1.8, such that the fluctuations can be treated as incompressible. The mean quantities do require the compressible approach, however.

For the Reynolds stress, a vast amount of URANS turbulence models have been developed that approximate the Reynolds stress. Most models are based on the assumption that the Reynolds stress follows a linear relationship with the mean strain rate $\widetilde{S}_{ij}$. Mathematically, this is expressed by the Boussinesq approximation for compressible flows [Gatsky and Bonnet, 2009]:

$$-\overline{\rho u_i' u_j'} = 2\widetilde{\mu}_t \left(\widetilde{S}_{ij} - \frac{1}{3}\frac{\partial \widetilde{u}_k}{\partial x_k} \right) - \frac{2}{3}\overline{\rho} k \delta_{ij}. \tag{2.9}$$

The eddy viscosity μ_t is the only remaining unknown quantity that needs modeling, either by algebraic modeling or with additional transport equations [Hickel, 2016]. The most renowned linear eddy viscosity model, currently having the largest preference in industry, is the k-ε model by Jones and Launder [1972]. The method introduces two additional transport equations for turbulent kinetic energy and dissipation rate. The k-ε model is particularly advantageous with the prediction of free shear flows, but fails to predict pressure-induced flow separation [Hickel, 2016]. Close to walls the model is less effective due to the strongly anisotropic effects. Under the presence of strong boundary layers, separated flows or anisotropic flow fields in general, the k-ω of Wilcox [1988] provides more reliable results. Both the k-ε and k-ω model can be blended to obtain the zonal shear stress transport (SST) model of Menter [1993]. The Spalart and Allmaras [1994] model is a final example of linear eddy viscosity models, requiring the solution to only one additional transport equation. The model is thus cheaper than its two-equation counterparts and robuster than the k-ω model, but similar to the k-ε model it does not perform well under the presence of free shear layers [Fluent Inc., 2006].

Alternatively, Reynolds stress models (RSM) can be used to calculate the eddy viscosity and close the URANS equations. In terms of computational cost, however, the models are less effective; the standard RSM might need as much as seven additional transport equations [Hickel, 2016]. This underlines the preference of linear eddy viscosity models in the engineering industry.

Results from URANS simulations deliver qualitative results of the ensemble-averaged flow field, but they do not provide local unsteadiness. This means that the solution may provide correct visual representations of the large-scale structures, but the information on small-scale structures is lost. Moreover, the solution might be very dependent on grid size. As the entire turbulent energy spectrum is modeled, a decrease in cell size will not converge towards DNS accuracy [Hickel, 2016]. A way to overcome the information loss is the application of a Scale Adaptive Simulation (SAS) [Menter

and Egorov, 2005]. It essentially consists of a URANS model, with the addition of the von Karman lengthscale

$$\ell_{\mathrm{vK}} = \kappa \left| \frac{\partial U/\partial y}{\partial^2 U/\partial y^2} \right|. \tag{2.10}$$

The simulation uses ℓ_{vK} to adjust the URANS model to the size of the resolved eddies, rather than the thickness of the shear layer (as is done by conventional turbulence models). This way, an LES-like flow field with more meaningful coherent structures is obtained, although the computational cost is lower since the fluctuations are still ensemble-averaged [Menter *et al.*, 2011]. Depending on the problem, however, SAS might locally introduce very small cells, such that the cost is not directly comparable to standard two-equation URANS models.

2.2.2 Large Eddy Simulation

Similarly to the URANS equations, the Large Eddy Simulation (LES) approach sees turbulence as a mean velocity and a fluctuation. Only now, the mean velocity of the large scales is resolved with a filtered solution of the Navier-Stokes equations [Deardorff, 1970; Smagorinsky, 1963]. A subgrid-scale (SGS) model is used to account for mixing and dissipation occurring in the microscales, and the effect they have on the large-scale structures. Therefore, the filtered velocity field contains information on the subgrid-scale motions, resulting in a strong coupling between the grid resolution and the SGS model [Pope, 2000]. Moreover, in engines operating at higher speeds the local Reynolds numbers increase, leading to smaller Kolmogorov scales and the need for further refinement [Nguyen *et al.*, 2016].

The SGS stress tensor can be modeled with several techniques. Firstly, the model can be based on the scale similarity model (SSM) proposed by Bardina *et al.* [1980]. Essentially, the method relates the statistical structure of the unresolved scales to the filtered flow field. It provides good correlations for homogeneous isotropic turbulence and free shear flows, but the dissipation of the SGS is often not large enough [Hickel and Hulshoff, 2017]. The Bardina model is a subclass of the more recently introduced Approximate Deconvolution Method (ADM) [Stolz and Adams, 1999]. Similarly to Bardina, the ADM provides good correlations of the SGS stress tensor for homogeneous turbulence and shear flows.

Secondly, the SGS can be modeled with so-called eddy viscosity models (EVMs), which are based on the molecular diffusion of the gas kinetics. This approach is the most popular because it considerably reduces the modeling effort. The most widely used version was introduced by Smagorinsky [1963]. For wall-bounded turbulence, however, it needs an ad hoc solution for the anisotropic nature of boundary layers. A 'van Driest' damping is often used to account for this. More recent viscosity models are the wall-adapting local eddy (WALE) viscosity model [Nicoud and Ducros, 1999], the Vreman model [Vreman, 2004] and the sigma model [Nicoud *et al.*, 2011]. They take into account the anisotropy of the boundary layer, and do not need an additional damping factor.

The last category consists of the development of a dynamically scaling model constant with the Germano identity [Germano *et al.*, 1991]. The aforementioned EVMs (e.g. Smagorinsky) can be combined with the dynamic procedure, such that the model constants are scaled using information from the resolved turbulence. Consequently, the prediction of dissipation in the boundary layer is improved and no additional damping is required [Pope, 2000].

By increasing the filter width (i.e. decreasing the cell size), more turbulent motions are resolved and an LES will eventually turn into a DNS [Pope, 2000]. No SGS modeling is then required anymore. As opposed to URANS, LES predicts the instantaneous flow features, but this also implies that the method requires more computational overhead. Moreover, the results from just one engine cycle are less meaningful, and at least ten consecutive samples are necessary for the mean velocity to converge [Ameen *et al.*, 2017; Joelsson *et al.*, 2011].

2.2.3 Hybrid models

Hybrid turbulence models employ a combination of RANS and LES models to combine the best features of both methods [Menter *et al.*, 2011]. RANS has proved to be effective in the near-wall region thanks to the calibration with respect to the law of the wall. Far away from walls, where the RANS predictions are much less uniform, the model switches to an LES. The transition between RANS and LES can be covered in a few ways that are described in this section.

Firstly, there is the Detached Eddy Simulation (DES), where the RANS model calculates the entire boundary layer and an LES-like model is applied in the rest of the domain. The method was initally based on the one-equation RANS model from Spalart *et al.* [1997], but works with the majority of two-equation models as well [Fluent Inc., 2006]. The local turbulent lengthscale is compared with the grid spacing at that location, and as soon as the grid spacing is too fine (according to a certain threshold), the model switches to LES mode. The DES limiter can therefore be defined as

$$d^* = \min\{d, C_{DES}\Delta_{max}\}, \tag{2.11}$$

where Δ_{max} is the maximum dimension of each grid cell and d is the distance to the closest wall.

Secondly, there is the possibility to apply RANS only in the inner part of the boundary layer, while the LES part covers a part of the outer boundary layer and the rest of the domain. This method is referred to as wall-modeled LES (WMLES) [Kawai and Larsson, 2012]. Lastly, there exist zonal or embedded LES (ZLES, ELES) methods where the entire field is essentially covered by a RANS model, except for some user-defined regions where the model switches to LES [Cokljat *et al.*, 2009].

Section 2.2.2 mentioned that LES needs a fine grid spacing near the wall to accurately capture the small-scale structures that account for the majority of the turbulent diffusion. By modeling (part of) the boundary layer with URANS, the fine grid requirement is not as stringent, such that computational time is saved. The switch from RANS to LES, however, may lead to inconsistencies such as grid-induced separation [Menter *et al.*, 2003]. When the grid is too fine in a RANS zone, the DES limiter is switched on too soon and the flow is locally resolved by LES. The RANS solution is then affected by the local flow instabilities of the LES solution. This problem usually occurs within the boundary layer. In order to account for this mismatch between both models, the Delayed DES (DDES) [Spalart *et al.*, 2006a] and Improved Delayed DES (IDDES) [Shur *et al.*, 2008] have been developed. Both methods overcome the grid-induced separation by including molecular and turbulent viscosity information and therefore delaying the transition outside the boundary layer. The DDES formulation, for instance, can be obtained by rearranging Equation (2.11) and adding the correction factor f_d for viscosity [Spalart *et al.*, 2006b]:

$$d^* = d - f_d \max\{0, d - C_{DES}\Delta_{max}\} \tag{2.12}$$

The factor f_d is a function of kinematic and turbulent viscosity, the velocity gradient and the wall distance d. For smaller distances to the wall, f_d approaches zero. The expression $d^* = d$ is then obtained, meaning that the original RANS model is solved. The other asymptote at $f_d = 1$ yields Equation (2.11).

Another problem with hybrid models is the loss of information if there is a distinct interface (e.g. for ZLES) [Hickel and Hulshoff, 2017]. Switching from LES output to RANS input is possible, since the LES solution is instantaneous and can be ensemble-averaged. The other way around can pose problems, however, as the averaged RANS solution does not provide the full instantaneous boundary conditions for LES. This can be solved by introducing artificial turbulence at the interface boundary.

2.2.4 Applications to internal combustion engines

Turbulence modeling in internal combustion engines is a topic that has been exploited by many researchers over the last decades, both connected to the academic world and the engineering industry. Nevertheless, the scientific community mainly focuses on established technologies such as liquid

Table 2.1: Comparison between CPU time and grid size for RANS and LES, from Som *et al.* [2012]

	URANS		**LES**	
	Cells	**CPU hours**	**Cells**	**CPU hours**
Chemistry off	150,000	32	2,100,000	320
Chemistry on	550,000	432	3,500,000	3,600

fuel injection of gasoline and diesel, and the novelty of gaseous injection has remained relatively untouched. In the following sections, a brief selection of articles is presented, of which it is believed that their conclusions are also valid for CNG direct-injection.

Benchmark in RANS versus LES

Som *et al.* [2012] carried out a comparison of a Smagorinksy LES and k-ε URANS[(2)] for the injection and ignition in a constant volume diesel vessel. In order to validate the simulations, they used experimental data from the Sandia National Laboratory [Idicheria and Pickett, 2007; Pickett *et al.*, 2011]. Their simulations showed that the LES predicts the instantaneous axial position of the fuel jet very well. Also the URANS simulation is able to predict the penetration length, but only in an ensemble-averaged sense. A lot of instantaneous information is therefore lost. Nevertheless, the general quality of URANS results are of similar level as the ones of the LES.

In terms of quantitative accuracy of the models, the LES predicts the air-fuel ratio more accurately. Especially near the sides of the jet, the LES produces much better agreement with the measurement than the URANS. When it comes to ignition delay, the difference between URANS and LES was found to be even larger. The URANS predictions of the ignition delay are off by ass much as 50% under some conditions. An independent study by Pitsch [2006] confirms this observation. Even though LES has a very expensive nature, the accuracy of the mixing process is very much improved.

The authors documented the computational effort that was required to simulate the above results. The results are given in Table 2.1. The simulated time amounts to 2 milliseconds for each case. The URANS and LES employ grids of different sizes since the authors wanted to reduce the subgrid-scale modeling of the LES by resolving more large-scale structures. The table shows that, for the case including chemistry, the LES took approximately eight times longer than the RANS model.

Banerjee and Rutland [2012] took the aforementioned comparison a bit further and did grid convergence studies for URANS and a dynamic Smagorinsky LES. It turns out that the correct penetration length can be obtained in LES on coarser grids than URANS. They also observed that a further coarsened LES behaves similar to a URANS-like simulation, since a large part of the spectrum is modeled. Very similar coherent structures are obtained in this case.

Benchmark in LES versus DES

A relevant comparison between different scale-resolving turbulence models has recently been carried out by Buhl *et al.* [2017]. The authors compared three classical LES models (Smagorinsky, WALE, sigma) against a hybrid model (DES-SST) and a scale adaptive URANS (SAS-SST), considering only the intake stroke of a simplified two-stroke engine. To their knowledge, it was the first systematic comparison of different scale-resolving models in internal combustion engines.

The LES and DES models produced similar representations of the resolved small-scale structures. After all, in the DES case an LES method is explicitly used to calculate the SGS structures of the flow field. In case of the SAS-SST model, however, less small structures were visible away from the jet. The fact that SAS is essentially still a URANS model with dynamic scaling means that more of the small scales are present compared to the standard URANS, but the flow field is still ensemble-averaged.

[(2)] The Re-Normalization Group (RNG) formulation for the k-ε model was used here [Yakhot *et al.*, 1992]. It consists of a normalization of the production term in the ε equation to distinguish between the dissipation of the large scales and the dissipation of the small scales. It improves the prediction of swirling flows.

The authors conclude that, taking into account the other observations from the article, the sigma model provides the best approximation with respect to the DNS and experimental results. Nevertheless, hybrid methods show a great potential. The authors did not include any information on simulation time, such that no conclusion can be drawn towards the efficiency of the methods.

Controlling the mixture formation

A major advantage of 3D-CFD is that accurate species concentrations, and more specifically the air-to-fuel ratio, can be visualized in each part of the domain. Twellmeyer *et al.* [2017] proposed four parameters that have a major effect on the eventual mixture formation in the cylinder, namely

1. refinement of the computational mesh;
2. use of different (eddy viscosity) turbulence models;
3. modification of the turbulent Schmidt number; and
4. adaptation of the initial turbulence level in the cylinder.

The first criterion merely refers to the fact that the grid should be fine enough to capture the energy drain of the smallest structures in the flow. As mentioned before, further refinement of an LES indeed improves the accuracy of the simulation as less scales are modeled. For a RANS or DES simulation, this is not guaranteed. A proper grid convergence is thus necessary to check the influence of the grid on the eventual mixture formation. The second criterion, requiring different considerations for the computational grid, is closely related to this and has been addressed in the previous subsections.

The turbulent Schmidt number

$$Sc_t = \frac{\nu_t}{D_t} \tag{2.13}$$

is a dimensionless number that determines the relation between turbulent viscosity ν_t and eddy diffusivity D_t. By lowering Sc_t, the relative importance of diffusion on the smallest scales becomes more dominant, and turbulent mixing is enhanced. Analyzing the values of the turbulent Schmidt number is a hot topic in the scientific community, although the applications to internal combustion engines are still scarce. Gualtieri *et al.* [2017] investigated the range of values applicable to certain test cases for environmental flows. They concluded that it is impossible to identify a universal value for Sc_t, and moreover that the Schmidt number varies locally within the flow field. Tominaga and Stathopoulos [2007] confirmed this observation and added that the range of turbulent Schmidt numbers can be as large as 0.2 to 3.5. They indicated that it could be a calibration parameter for RANS simulations to correct for the underestimation of the turbulent momentum diffusion, although this cannot be generalized for other flow states (such as different engine speeds).

Finally, the adaption of the initial turbulence level is considered to influence the mixture formation. This is closely related to cyclic variability and therefore of great importance to CFD. Simulations are often initialized with a constant turbulence intensity, and it was shown by Ameen *et al.* [2017] and Joelsson *et al.* [2011] that the combustion of the first run is still very dependent on that initial field. By running a large number of consecutive cycles, the effect of initialization disappears.

Additional considerations for turbulent combustion

From the previous analyses, it seems that LES and DES are promising methods despite their large(r) computational cost than URANS. Pope [2004] affirms that LES has been gaining a lot of attention, and the computational resources will soon be powerful enough to implement LES in industry. However, he addresses turbulent combustion as a mechanism that cannot be accurately predicted by LES. Most chemical reactions occur on subgrid-scale levels and are therefore not fully resolved. Some combustion models are indeed based on RANS and they use the same calibration coefficients. Nevertheless, in case of direct-injection engines, a well-resolved LES provides better estimations of the fuel mixing and should therefore still be preferred over URANS for combustion. There may however be a mismatch between the smallest resolved structures in LES and the microscales needed for the combustion model.

2.3 Combustion modeling

This section covers the theoretical background on combustion modeling, including the basic principles and the state-of-the-art in engine simulation of combustion cycles. The distinction is made between chemistry models and combustion models. The latter is a category of models that use simplified assumptions to track the flame front, and separate models have been developed for premixed and non-premixed combustion. Premixed combustion, the dominant phenomenon in spark-ignition engines, features a chemistry-controlled mechanism. On the other hand, non-premixed combustion, occurring in compression-ignition engines, is controlled by diffusion on molecular level. According to Zanforlin and Boretti [2015], CNG injection is very similar to gasoline DI in terms of mixture formation, provided the liquid gasoline droplets are of moderate size. With this assumption and the long injection duration in mind, the scope of the current project is limited to the investigation of premixed combustion models and chemistry models. The following two sections elaborate upon their theoretical basis.

2.3.1 Chemistry models

Detailed chemistry models employ a reaction mechanism file that includes the species (and often also the elementary reactions) that are considered important for a particular application. Choosing the correct mechanism file is equally important as choosing the correct chemistry model to handle the mechanism. For CH_4 combustion in particular, tailored reaction mechanisms have been developed. The example with the largest recognition in the scientific community is the GRI-Mech 3.0 solver from Berkeley University [Smith *et al.*, 2018]. It uses 325 reactions and 53 species (including Argon), and is able to accurately predict NO formation. By using this mechanism, there is theoretically no need to calibrate the model to the engine configuration, as is often the case for simplified combustion models.

The reaction mechanism is subsequently used by a chemistry model to specify the rates for each particular reaction. A widely accepted choice is the Chemical Equilibrium model [Kong *et al.*, 1995]. It assumes that the chemistry timescale is infinitely small compared to the diffusive timescale, such that there always exists chemical equilibrium on molecular level. The model does therefore not require specification of individual reaction rates, but only the involved species.

The majority of chemistry models are however based on an additional expression for the chemical reaction rates. Most often, the simple Arrhenius expression

$$k_{fr} = AT^b \exp\left(\frac{-E_a}{RT}\right) \tag{2.14}$$

is used to model the forward rate at which a reaction is occurring. In this equation, R is the universal gas constant, T is the temperature, E_a is the activation energy of the fuel, and A and b are two fuel-dependent constants. The latter three are specified in the reaction mechanism file. The reverse rate can be calculated with a similar formula, although it is computationally cheaper to model it using a fuel-dependent equilibrium coefficient, such that

$$k_{rr} = \frac{k_{fr}}{K_{eq}}, \tag{2.15}$$

where k_{fr} stands for the forward rate coefficient and k_{rr} for the reverse rate. Well-known examples of chemistry models using Arrhenius reaction rates are the Shell model by Halstead *et al.* [1977], the SAGE detailed chemistry solver by Convergent Science [2018] and the HTC code by Lund [1978].

2.3.2 Premixed combustion models

Premixed flames consist of a thin flame front that is highly wrinkled due to the influence of turbulent microscales [Peters, 2000]. This flame front contains an inner layer, typically 10% of the total flame thickness, which keeps the flame 'alive'. It can be seen as a discontinuity surface where there exists a steep gradient of species concentrations and thermodynamic properties [Pitsch, 2006]. The flame

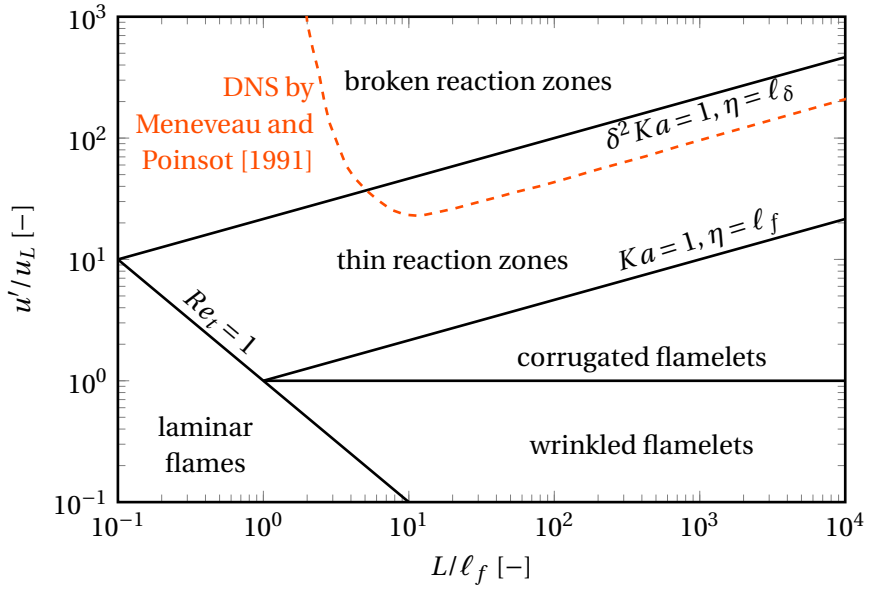

Figure 2.2: Borghi diagram of premixed turbulent combustion regimes

can experience different states, depending on the interaction between the chemical and turbulent lengthscales. A useful way to visualize these regimes is by means of the Borghi diagram in Figure 2.2 [Borghi, 1985; Peters, 2000]. Both axes quantify the relation between the strength of the turbulent structures in the flow, characterized by the turbulent intensity u' and the integral scale L, and the flame properties, characterized by the laminar burning velocity u_L and the laminar flame thickness ℓ_f. The flame regimes are demarcated by isolines of two dimensionless numbers, the first of which is the Karlovitz number

$$Ka = \frac{\tau_c}{\tau_\eta}. \tag{2.16}$$

In this equation, τ_η stands for the turnover time of Kolmogorov timescales and $\tau_c = D/u_L^2$ stands for the chemical timescale, defined as the residence time in the laminar flame. The latter equation makes uses of the molecular diffusivity D.

The second isoline is given by the turbulent Reynolds number, which can be defined for a velocity fluctuation within the wrinkled flame front:

$$Re_t = \frac{u'\ell_f}{\nu}. \tag{2.17}$$

Finally, a modified Karlovitz number is often included as well, based on the inner layer thickness ℓ_δ of the flame. As a rule of thumb, $\ell_\delta = 0.1\ell_f$. The following remarks can be made about the different flame regimes [Lin, 2010; Peters, 2000].

Laminar flames	$Re_t < 1$	As most burning flames are turbulent, this region falls outside the scope of interest.
Wrinkled flamelets	$Re_t > 1$ $u' < u_L$	This region is not of interest as the laminar burning velocity dominates the turbulence. The largest turbulent motions are not fast enough to introduce flame interactions.
Corrugated flamelets	$Re_t > 1$ $Ka < 1$	It follows that $\ell_f < \eta$, such that the turbulent flame structure is contained within the Kolmogorov scales. Turbulent fluctuations are still large in size and have little effect on the flame propagation, thus it remains quasi-steady. The flame can be characterized by a quasi-laminar burning velocity u_L in this region.

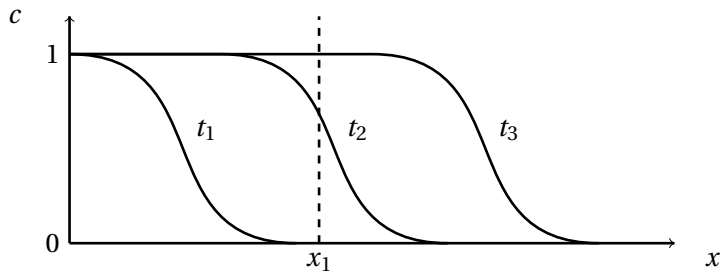

Figure 2.3: Burning profile of the progress variable, adapted from Merker *et al.* [2006]

Thin reaction zones	$Re_t > 1$ $Ka > 1$ $\delta^2 Ka < 1$	As $\ell_f > \eta$, the smallest eddies can penetrate the turbulent layer where the reactions take place. The scales are however still larger than the inner layer thickness ℓ_δ, which is typically around 10% of the turbulent flame thickness. The corresponding Karlovitz number at the upper boundary is $Ka = 100$. Meneveau and Poinsot [1991] argued that the flame structures in this region still propagate with a quasi-laminar burning speed until a Karlovitz number of about 25 before flame quenching locally occurs. The DNS data supporting this hypothesis is plotted in Figure 2.2 with a red dashed line. For Ka larger than this line, the velocity is strongly dependent on the turbulent microscales and may or may not be laminar anymore.
Broken reaction zones	$Re_t > 1$ $\delta^2 Ka > 1$	The chemistry locally breaks down as the smallest eddies can enter the inner layer of the reaction zone. A large amount of heat is released, with the consequence that the flame extinguishes.

A set of models has been developed for the regions where the flame travels with a laminar burning speed. These so-called flamelet models are based on the non-reactive scalar quantities c and G, introduced in the next sections. The applicability of these models is thus only justified in the corrugated flamelet region and a part of the thin reaction zones region or, alternatively, for $Re > 1$, $u' > u_L$ and $Ka < 25$. Note that this is only the case for premixed combustion, as for the non-premixed counterpart no characteristic velocity can be defined.

Modeling based on the progress variable *c*

The progress variable is a normalized mass fraction of the fuel at a given point in the combustion chamber [Merker *et al.*, 2006]. It is represented by a monotonic function from 0 (fresh reactans) to 1 (all reactans converted to fully burned products), illustrated by Figure 2.3[(3)]. For a given point x_1 in the combustion chamber, the charge is fresh ($c = 0$) at t_1, being burned at t_2 and fully burned ($c = 1$) at t_3.

The most general (and perhaps the most practical) definition of c is given by

$$c = \frac{Y_F - Y_{F0}}{Y_{F\infty} - Y_{F0}}, \tag{2.18}$$

where Y_F is the fuel mass fraction, Y_{F0} is the value of Y_F for fresh reactans and $Y_{F\infty}$ is the value of Y_F for burned products. In case the mixture is lean, $Y_{F\infty}$ is equal to zero as it is assumed that all fuel is

[(3)] The flame moves relative to a fixed point x_1 in the combustion chamber.

burned. Using this definition of the progress variable, a general transport equation can be defined for the species mass fractions analogously to the momentum transport equation:

$$\frac{\partial(\rho c)}{\partial t} + \frac{\partial(\rho u_i c)}{\partial x_i} = w + \frac{\partial}{\partial x_i}\left(\rho D_c \frac{\partial c}{\partial x_i}\right). \tag{2.19}$$

In this equation, D_c is the molecular diffusivity of the progress variable. Similarly to the Navier-Stokes equations in turbulence modeling, compressibility effects must be accounted for. Density fluctuations due to the interaction of turbulence and thermal expansion require density weighted averaging in the Favre-Averaged Navier-Stokes (FANS) sense [Bray, 1995; Cant, 2011]. A similar expression to the decomposition in Equation (2.2) is obtained:

$$c = \widetilde{c} + c' \qquad \text{with the Favre mean} \quad \widetilde{c} = \frac{\overline{\rho c}}{\overline{\rho}}. \tag{2.20}$$

All flamelet models based on the progress variable require the solution to an additional transport equation [Peters, 2000]. The Favre-averaged solution is given by

$$\frac{\partial(\overline{\rho}\widetilde{c})}{\partial t} + \frac{\partial(\overline{\rho}\widetilde{u}_i\widetilde{c})}{\partial x_i} = \underbrace{\overline{w}}_{\substack{\text{mean rate of}\\ \text{chemical reactions}}} + \underbrace{\frac{\partial}{\partial x_i}\overline{\left(\rho D_c \frac{\partial c}{\partial x_i}\right)}}_{\substack{\text{mean rate of}\\ \text{molecular transport}}} - \underbrace{\frac{\partial}{\partial x_i}\overline{\rho u_i' c'}}_{\substack{\text{mean rate of}\\ \text{turbulent transport}}}. \tag{2.21}$$

The variables with a tilde denote a Favre-averaged (i.e. density weighted) quantity, while the overbars stand for a conventional ensemble-averaged quantity. The terms on the right-hand side are unknown and must be modeled to provide closure of the transport equation. The molecular transport term is often neglected for high Re flows, such as the ones in combustion engines [Merker *et al.*, 2006].

The turbulent transport term is the first one that needs modeling. The transport consists of two contributions: gradient and countergradient transport [Cant, 2011]. Both can be modeled based on the statistical correlation between density and velocity fluctuations in the thin flame front. Gradient and countergradient transport can locally occur in the same flame front, although the global average is usually used for modeling. Referring back to Figure 2.3, the progress variable c monotonically increases from zero to one in a statistically one-dimensional sense. Due to the heat release across the flame, the downstream density drops and the velocity normal to the flame rises [Zimont and Biagioli, 2006]. The way in which the density and velocity fluctuations interact determines the type of transport.

The gradient transport modeling approach is justified when the heat release across the flame results in a density fluctuation that moves in the same direction as the velocity fluctuation [Bray, 1995; Cant, 2011]. The turbulent transport term is thus positive along the direction of the reaction progress variable, leading to a positive gradient transport. The expression

$$\overline{\rho u_i' c'} \approx \overline{\rho}\widetilde{u_i' c'} = -\overline{\rho}\frac{\nu_t}{Sc_t}\frac{\partial \widetilde{c}}{\partial x_i} \tag{2.22}$$

is often used to model the term in Equation (2.21). The magnitude of the turbulent transport is thus partially controlled by the eddy viscosity μ_t and the turbulent Schmidt number Sc_t.

In reality, however, countergradient transport is usually prevalent [Merker *et al.*, 2006]. This is a pressure-driven process in which the low-density products are moved to the high-density reactans. The Bray number

$$N_B = \frac{\tau}{2\alpha}\frac{u_L}{u'} \tag{2.23}$$

may be used to judge which type of transport is occurring in the flame front, where τ is the flame heat release factor and α an efficiency factor for gradient transport based on the turbulent lengthscale ratio L/ℓ_f [Veynante *et al.*, 1997]. The latter thus indicates the ability of various-size eddies to affect

the flame front, similar to the definition of the Borghi diagram. An empirical relation for α and L/ℓ_F has been established by Veynante *et al.* [1997] using DNS data. Assuming the ideal gas law, the flame heat release factor τ can be expressed in terms of the burned and unburned temperatures of the gas:

$$\tau = \frac{T_b - T_u}{T_u}. \tag{2.24}$$

Gradient transport is thus prevalent if τ is low and the turbulent fluctuations dominate the flame front. Quantitatively, this is the case when the Bray number is smaller than 1.

The defining part about a specific combustion model lies in the model for the reaction rate term in Equation (2.21). It is assumed that the chemical reactions take place in thin flame surfaces that are locally laminar but highly wrinkled due to the presence of small-scale turbulent structures. More turbulence leads to stronger wrinkling of the flamelet, which results in faster burning [Peters, 2000].

The simplest approach consists of the eddy break-up (EBU) model, originally introduced by Magnussen and Hjertager [1976]. The model assumes that the chemistry occurs infinitely fast (chemical timescales are much shorter than turbulent timescales) and the reaction rate is determined by the turbulent dissipation on molecular level ("mixed = burned"). For URANS turbulence modeling, the mixing rate is inversely proportional to the turbulent timescale, such that the chemical reaction rate in Equation (2.21) becomes

$$\overline{w} = C_{EBU} \frac{\widetilde{\varepsilon}}{\widetilde{k}} \overline{\rho c' c'}, \tag{2.25}$$

where $\widetilde{\varepsilon}$ and $\widetilde{k}$ refer to the Favre-averaged turbulent dissipation rate and turbulent kinetic energy, respectively. The simplicity of the EBU model leads to a very low computational effort, although the predictions near the wall can be far off [Merker *et al.*, 2006]. Also, the constant C_{EBU} is fuel-dependent and must be tuned for each individual case, making the model less straight-forward to apply a priori to complex flows. An adaptation for LES exists and still lacks proper accuracy. Nevertheless, the near-wall chemistry is improved because the large-scale transport fluxes are fully resolved, whereas in URANS the entire turbulence spectrum is modeled [Boger *et al.*, 1998]. Unresolved transport fluxes are thus lower for LES and the uncertainty associated with the model constants will have a smaller impact on the results.

A second category, also building further on the infinitely fast chemistry assumption, consists of coherent flame models (CFM) [Marble and Broadwell, 1977]. They provide an algebraic expression for the chemical reaction rate in terms of the density of flame surfaces Σ within the flame. The expression is given by

$$\overline{w} = \overline{\rho}\, u_L I_0 \Sigma. \tag{2.26}$$

In this equation, I_0 is a correction factor for straining and curvature of the flame that, together with the laminar burning velocity u_L, is a known property of the thermochemical reaction. The flame surface Σ, however, has to be modeled with an additional transport equation, given by

$$\frac{\partial \Sigma}{\partial t} + \frac{\partial}{\partial x_i} \langle u_i \rangle_s \Sigma = \underbrace{\langle a_T \rangle_s \Sigma}_{\text{mean strain rate}} \underbrace{- \frac{\partial}{\partial x_i} \langle u_D N_c \rangle_s \Sigma}_{\text{propagation}} + \underbrace{\langle u_D \frac{\partial N_c}{\partial x_i} \rangle_s \Sigma}_{\text{curvature}}. \tag{2.27}$$

Here, a_T represents the hydrodynamic strain rate, N_c is a unit vector based on the progress variable c and u_D is the flame displacement speed. The operator $\langle \cdot \rangle_s$ denotes a surface average [Cant, 2011; Sellmann *et al.*, 2016]. For full closure of the CFM model, it is thus required to solve two additional transport equations (one for c and one for Σ) and to model three unknown terms. On top of that, fine mesh resolutions are required for high Reynolds numbers, rendering the method questionable for internal combustion engines [Manz, 2016].

Modeling based on the scalar function *G*

A second family of premixed combustion models is based on the scalar field function G [Williams, 1985]. Theoretically, it is a mathematical expression rather than a model. The solution is based on a 'level-set' approach [Sethian, 1996], meaning that the value $G(x_f, t) = G_0$ is fixed at the spatial location of the flame surface x_f. Areas in which $G > G_0$ represent regions where the gas is burned, while $G < G_0$ contains fresh reactans. The choice of G is arbitrary, but it remains fixed for a particular combustion event.

The G-equation is given by

$$\frac{\partial G}{\partial t} + u\nabla G = u_D |\nabla G|, \tag{2.28}$$

where u is the fluid velocity and u_D the flame displacement speed. By solving for G, the exact flame position can be identified. There is however no simple relation between u_D and the laminar burning speed u_L. Assuming that the flame is contained within the corrugated flamelet regime the displacement speed can be expanded into three different terms, accounting for the (quasi-)laminar burning speed, strain rate S and curvature κ (similarly to I_0 in the CFM model) [Merker *et al.*, 2006]. The extended G-equation is then obtained:

$$\frac{\partial G}{\partial t} + u\nabla G = \big(\underbrace{u_L^0}_{\substack{\text{uncorrected} \\ \text{laminar speed}}} - \underbrace{u_L^0 \mathscr{L}\kappa}_{\text{curvature}} - \underbrace{\mathscr{L} S}_{\text{strain}} \big) |\nabla G|, \tag{2.29}$$

where $\mathscr{L}$ is the Markstein length, which is proportional to and of the same order of magnitude as the laminar flame thickness.

The extended equation is however only valid in the corrugated flamelet regime where the laminar burning velocity is well-defined. In the thin reaction zones, the turbulent nature of the flow field influences the diffusion of chemical species and temperature in the regions ahead of the flame front, and this in turn has an effect on the burning speed of the flame [Peters, 2000]. It is thus impossible to derive a constant laminar burning speed as was done for Equation (2.29). A second level-set equation can be constructed for the this particular regime using the assumption that the thin reaction zones are equal to the inner reaction layer of the flame. This allows to construct the second extended G-equation based on the similarity with the change in temperature over the flame:

$$\frac{\partial G}{\partial t} + u\nabla G = \big(u_{L,s} - \alpha\kappa \big) |\nabla G|. \tag{2.30}$$

The flame speed $u_{L,s}$ thus contains contributions of normal diffusion and chemical reactions and is of fluctuating nature. It is important to note that $u_L^0 \neq u_{L,s}$, although they are of the same order of magnitude. The magnitudes of the thermal diffusivity α and $u_L^0 \mathscr{L}$ from Equation (2.29) are comparable as well.

The G-equation valid in both regimes can be constructed by assembling the leading terms for each regime in the right-hand side of Equations (2.29) and (2.30). As mentioned before, the Karlovitz number in the thin reaction zones is very large, suggesting that the curvature term is dominant for this type of flames. Indeed, due to the penetration of eddies in the turbulent flame front, the flame becomes highly wrinkled. Instead, for corrugated flamelets the laminar flame speed is more relevant than its wrinkling. The strain term is often neglected for both equations, leading to the following combined formulation that is valid for both the corrugated flamelets and the thin reaction zones:

$$\frac{\partial G}{\partial t} + u\nabla G = \big(u_L^0 - \alpha\kappa \big) |\nabla G|. \tag{2.31}$$

The G-equation method in general is very attractive as it leaves the flame profile and its propagation speed uncorrelated [Manz, 2016]. This implies that the method performs well even with coarse mesh resolutions. A problem of the method, similar to the EBU, is that it predicts very thin, laminar zones near the wall. Moreover, the method requires solving two additional transport equations. It is therefore assumed that the computational time is comparable to the CFM method.

2.3.3 Applications to internal combustion engines

Currently there is no record of a specific comparison of premixed combustion and chemistry models for the case of direct-injection spark-ignition CNG engines. Nevertheless, comparisons have been carried out in literature for simplified engine geometries or simple test cases. The most relevant ones are discussed in the following sections. In the review, it is assumed that the long injection duration of CNG engines results in a homogeneous mixing, according to the observations of Zanforlin and Boretti [2015]. Therefore the focus lies on applications of premixed combustion.

Comparison of premixed combustion models
The EBU model was compared to the CFM model by Brandl *et al.* [2005], who found that, for a constant volume vessel, the two models predict the same flame speeds. There was however no comparison with experimental data available, such that the models could not be validated. Another drawback is the simplicity of the test case, such that the authors indicate that for more complex problems the model constant C_{EBU} might not be justified anymore and the EBU model would not perform well. In that respect, the CFM model should be preferred over the EBU.

The G-equation model was compared to the CFM model in a two-dimensional engine test case by Cornolti [2015]. He found that the G-equation is very effective in predicting the in-cylinder pressure rise for high-load, while the CFM method completely fails. The maximum in-cylinder pressure is however overpredicted by the G-equation. For lower engine loads, the CFM seems to be the preferred method as it correctly estimates the maximum pressure, although the build-up is incorrect.

Judging the results, the author argues that the G-equation is the simpler (most comprehensive) method of the two and should be preferred. It completely decouples the flame structure, the brush thickness and the burning speed, such that they can all be modeled separately using correlations from different authors.

2.4 Motivation of the present work

As gasoline and diesel engines are a well-established technology, there are several studies available for these particular configurations. The use of alternative fuels such as CNG, together with the advent of new injection technologies, introduces uncertainty in the existing simulation methodologies and potential towards the improvement of their predictivity.

The CNG engine in this study uses outward-opening direct-injection to deliver the fuel to the combustion chamber. Not only does DI introduce a significant amount of turbulence in the combustion chamber, it also requires significant tumble from the fresh air entering through the intake port to promote mixing. Several articles confirmed that RANS, being the current standard practice in industry, does not predict the correct shape of the fuel jet and, eventually, the mixture formation, thus providing an unreliable initialization for combustion. A scale-resolving simulation, such as LES or DES is needed to accurately resolve the dissipation of the small scale turbulence. According to the benchmark results, an LES can however take approximately eight times longer than the URANS due to the requirement for fine grids. So far, no record has been found of a systematic comparison between LES, DES and RANS for a complete engine cycle.

According to Twellmeyer *et al.* [2017], other factors that influence the mixture formation of CNG are density of the computational grid, the turbulent Schmidt number and the initial turbulence level in the cylinder. The former can be ruled out by doing a proper grid convergence study, such that the simulation result is independent of the cell size (to a certain threshold). The latter two are useful parameters to investigate once the base model is set up.

Based on the foregoing remarks, a first research question can be defined.

Research question 1 *How is the mixture formation of direct CNG injection affected by turbulence modeling?*

- **Subquestion 1** *Does the novel Detached Eddy Simulation approach provide a distinct advantage in computational time compared to LES and in accuracy compared to RANS?*

- **Subquestion 2** *How does the turbulent Schmidt number affect the prediction of turbulent diffusion?*

Research question 2 *How sensitive are the mixture formation and combustion to the results of the previous engine cycle?*

As soon as a reliable method for the mixture formation is obtained, its influence on the combustion should be treated in detail. The gaseous state of the fuel results in reduced gas jet momentum during the direct-injection of the fuel. A long injection timing is necessary to compensate the momentum loss of the gaseous injection and to obtain a close-to-stoichiometric mixture. Especially at high engine loads, the start of injection is thus moved forward within the cycle, such that the gases have more time to form a homogeneous mixture. Given the long injection durations, it is therefore assumed that premixed combustion is prevalent. This is conform to the observations of Zanforlin and Boretti [2015].

From the presented premixed combustion models, the *G*-equation provides the best agreement at high engine loads. In addition, the claim from Manz [2016] that the model performs well on coarse grids means that it is potentially less expensive compared to chemistry solvers. The *G*-equation is however based on the fact that the flame propagates in a laminar fashion, which is not the case when there are local pockets of unmixed air and fuel in the combustion chamber, and excessive turbulence can render the model invalid. The following research question is obtained.

Research question 3 *Does the premixed G-equation model provide distinct advantages over the potentially more expensive chemistry solvers for CNG combustion under high engine loads?*

Finally, most observations from literature were made at engine speeds of around 2000 rpm, representing the part load operating point. It is not clear whether or not the turbulence and combustion models are equally predictive at different rotational speeds. High engine speeds are more critical to obtain a homogeneous mixture, as very little time is available to obtain a homogeneous mixture. Part load characteristics are however equally important, as they can provide insight in engine-out emissions. The possibility to generalize the observations for both operating conditions should therefore be investigated, leading to the final research question.

Research question 4 *Can the results of the analysis at high engine speeds be generalized to predict other operating conditions?*

In summary, a reliable and cost-effective CFD methodology could have large implications on the development of alternative fuel engines. Since gathering instantaneous measurement data in 3D for gaseous injection is hardly possible, the result of this work could stimulate the implementation of CNG engines in the automotive industry.

3

Simulation methodology

The development of the simulation methodology was done systematically using information from literature and an experiment conducted on the engine test bench. The workflow of the methodology setup is depicted in Figure 3.1, which was built according to the main assumptions in Section 3.1. Next, Section 3.2 presents the implementation of the computational domain in CONVERGE, with a description of the relevant boundary conditions, initial conditions and the definition of the moving surfaces. The verification and validation of the base model is subsequently treated in Section 3.3, where a grid convergence study motivates the choice of the base grid size for the different turbulence models. The simulation is compared to experimental data in order to calibrate the model and use a meaningful initial flow field at the start of combustion. Finally, Sections 3.4 and 3.5 discuss the configuration of the turbulence and combustion models, respectively, and a motivation on the choice of different submodels. A description on the calibration of the second operating point can be found in Chapter 4.

3.1 Engine configuration

This section provides the necessary fundamentals to understand the setup of the CFD methodology. First of all, a short description of the working principles of an internal combustion engine is presented. Next, the measurement data are introduced, and their information is subsequently used to come up with the main assumptions of this work.

3.1.1 Definitions

Each engine cycle consists of four strokes performed by a reciprocating piston, as depicted in Figure 3.2. During the intake stroke, the intake valves are opened, and the downward motion of the piston draws a charge of fresh air into the engine. Towards the end of the intake stroke, a cloud of fuel is injected for a duration depending on the operating condition. When the valves are closed, the air-fuel mixture is subsequently compressed by the piston and ignited at the top dead center (TDC). The spark creates a turbulent flame that propagates throughout the combustion chamber. During combustion, the piston is pushed down and power is generated. The burned mixture is then removed from the cylinder through the exhaust valves in the last of the four strokes. Strokes (a) and (d) combined are typically referred to as the gas exchange process. As a convention, the ignition top dead center is located at 0 degrees in the remainder of this report.

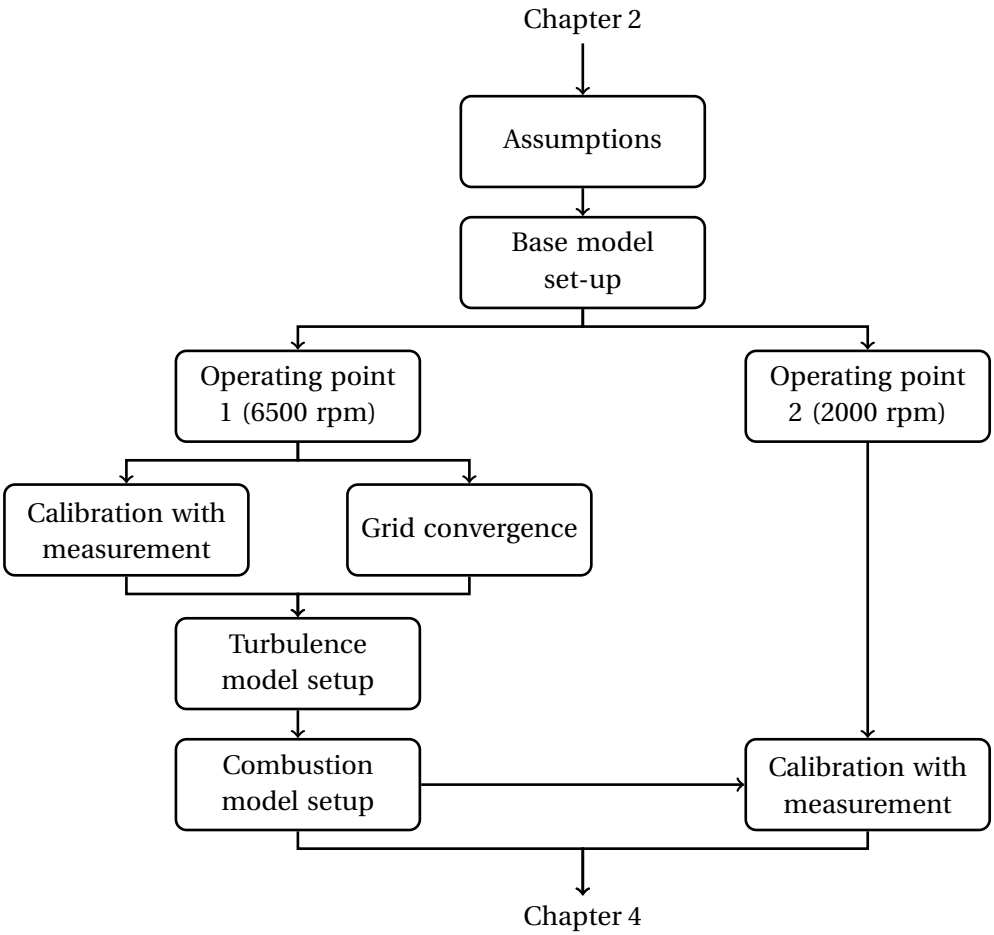

Figure 3.1: Breakdown of Chapter 3

Some important geometrical features of the cylinder have been indicated in Figure 3.2. The bore B is the diameter of the piston and the stroke S defines the distance between the top and bottom positions of the piston. The connection rod or conrod with length l_{cr} transfers the reciprocating motion of the piston to the rotating motion of the crankshaft. These three measures determine the displacement volume of the cylinder based on the crankshaft angle θ:

$$V_d = \frac{\pi B^2}{4} l_{cr} \left[1 + \frac{S}{2l_{cr}} (1 - \cos\theta) - \sqrt{1 - \left(\frac{S}{2l_{cr}} \right)^2 \sin^2\theta} \right]. \tag{3.1}$$

The compression ratio CR, fixed by the experiment, can be used to calculate the clearance volume:

$$V_c = \frac{\max\{V_d\}}{CR - 1}. \tag{3.2}$$

Finally, by combining Equations (3.1) and (3.2) the total in-cylinder volume is obtained:

$$V = V_d + V_c. \tag{3.3}$$

In the remainder of this report, the in-cylinder pressure is often plotted against the volume on logarithmic axes for calibration purposes. An example of such graph can be found in Figure 3.4. This visual representation has the advantage that the fluctuations in the gas exchange process are enlarged and are thus clearly visible. In addition, the slope of the compression stroke is (ideally) constant and can easily be related to the polytropic coefficient.

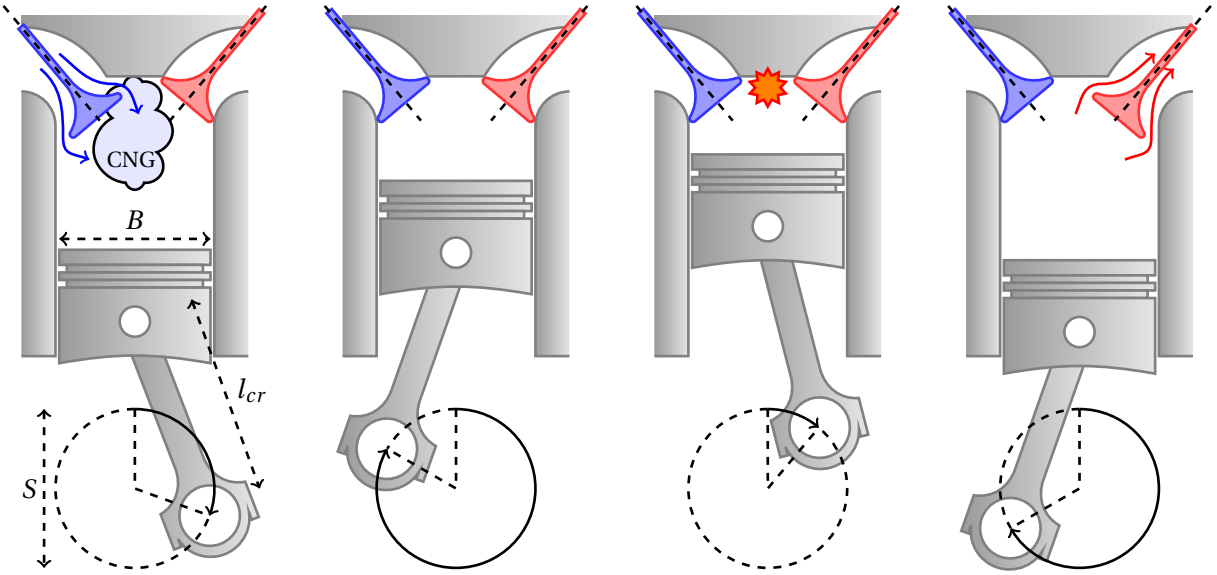

(a) Intake stroke (b) Compression stroke (c) Expansion stroke (d) Exhaust stroke

Figure 3.2: The four-stroke cycle

3.1.2 Measurement data

This report considers an existing V6 gasoline direct-injection engine with four valves per cylinder that was modified to accommodate CNG fuel. The implementation of CNG poses some challenges to the operating conditions of the engine, mainly because the fuel has a much lower density than gasoline. To achieve a sufficient amount of fuel for stoichiometric combustion, an outward-opening injector is used. The injector has a larger contact area between the combustion chamber and the fuel rail, allowing more fuel to enter at a given time, therefore compensating the deficit in fuel density.

The engine configuration was tested on the test bench and the in-cylinder pressure was recorded to validate the simulation results. Table 3.1 summarizes the boundary conditions from the experiment that were used to set up the simulation model. The fuel used in the measurement was a blend of 96% methane and marginal contributions of ethane and other compounds. For simplicity, it has been assumed that the fuel solely consists of CH_4.

Due to the low fuel density, CNG engines are usually run at a stoichiometric air-fuel ratio. Under this condition, the amount of fuel and oxidizer are fully consumed and converted to reaction products, as indicated by

$$CH_4 + 2O_2 + 7.52N_2 \longrightarrow CO_2 + 2H_2O + 7.52N_2. \tag{3.4}$$

Nitrogen is an inert gas, and its concentration should in theory stay constant throughout the combustion. Assuming an initial air concentration by volume of 79% nitrogen and 21% oxygen, the stoichiometric air-fuel ratio by volume calculated from Equation (3.4) amounts to 9.7.

The stoichiometry can be expressed by the air-fuel ratio of the mixture, defined as

$$\lambda = \frac{m_a/m_f}{(m_a/m_f)_s}, \tag{3.5}$$

where the subscripts a, f and s denote air, fuel and a stoichiometric quantity, respectively. A ratio of $\lambda = 1$ means that the mixture is stoichiometric. For $\lambda > 1$, there is excessive air and the mixture is referred to as lean. Instead, mixtures with $\lambda < 1$ are rich and contain an excessive amount of fuel.

Table 3.1: Summary of measurement data

Variable	**Value**	
Bore	84.5 mm	
Stroke	86.0 mm	
Conrod length	155 mm	
Compression ratio	12.9	
Fuel species	CH_4	
Lower heating value	48.55 MJ/kg	
Engine speeds	2000 rpm	6500 rpm
Pressure	Not shown	Figure 3.3a
Valve lift	Not shown	Figure 3.3b
Start of injection	468 deg	345 deg
End of injection	500 deg	600 deg
Spark timing	-26.2 deg	-24.3 deg
Injection pressure	7.0 bar	19.8 bar
Air-fuel ratio	1	1
Exhaust CO_2	10.9%	10.9%

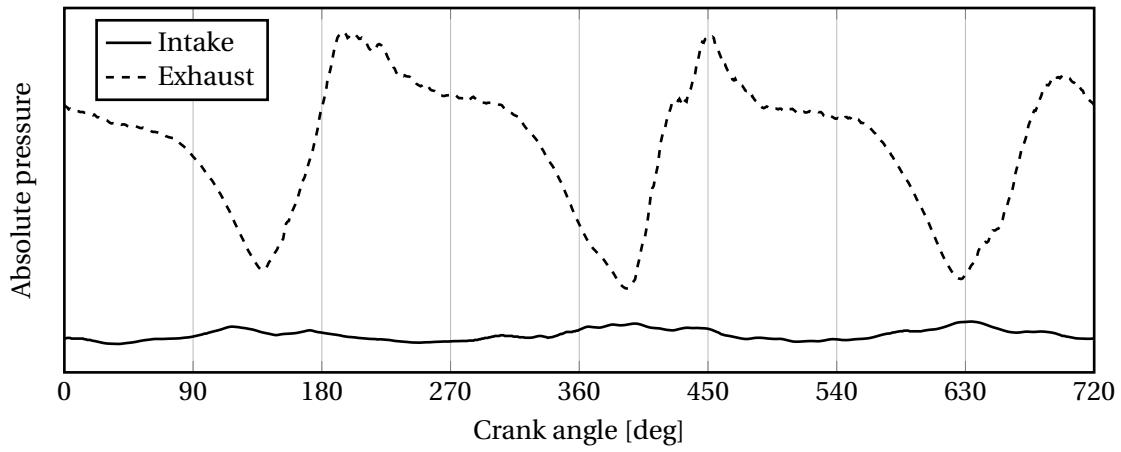

(a) Static pressure at intake and exhaust

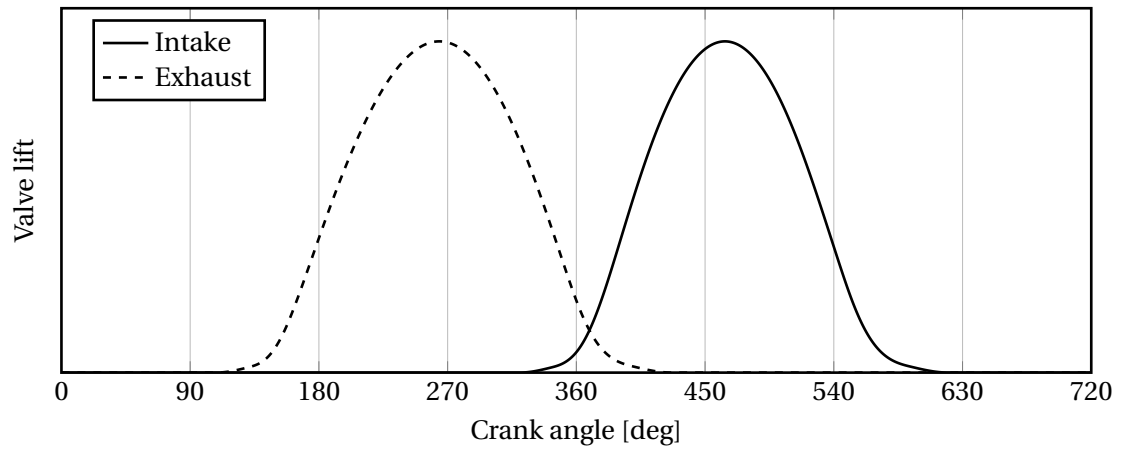

(b) Valve lift profiles

Figure 3.3: Measurement data for the peak power operating point

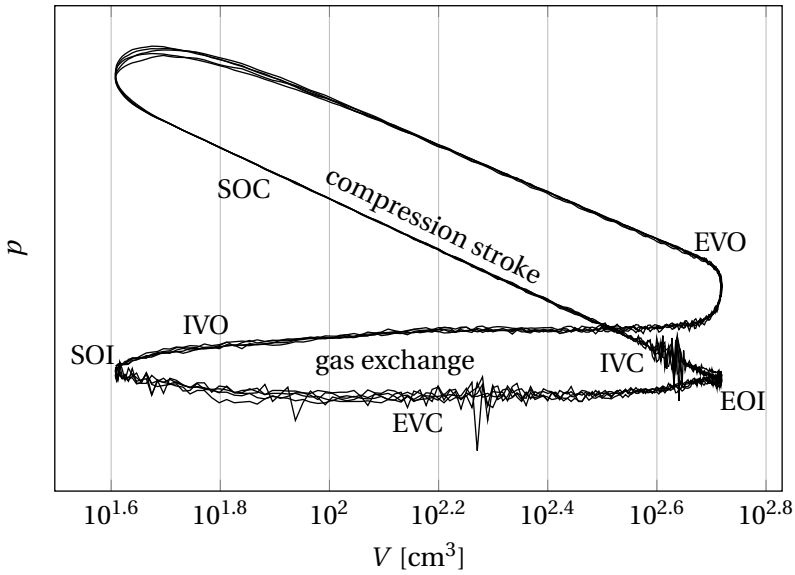

EVO:	Exhaust valve opening	EVC:	Exhaust valve closing
IVO:	Intake valve opening	IVC:	Intake valve closing
SOI:	Start of injection	EOI:	End of injection
SOC:	Start of combustion		

Figure 3.4: Cycle-to-cycle variations for cylinder 1

3.1.3 Assumptions

Even though the studied engine has a total of six cylinders, the simulation only considers one cylinder for the duration of one cycle. With this one-cylinder-one-cycle approach, the computational time is greatly reduced but the simulation relies on the fact that the cylinders and cycles are statistically the same. Even though this is theoretically the case, there exist a large amount of fluctuations in the measured quantities that are therefore not captured by the simulation. Such fluctuations are visualized in Figures 3.4 and 3.5, where the measured in-cylinder pressure is plotted versus the corresponding in-cylinder volume. The former plot indicates the cyclic variations that exist in the first of the six cylinders, recorded during five consecutive cycles. The lower loop, depicting the gas exchange process, is very similar for all cycles. Some small fluctuations can be noticed, corresponding to the pressure waves that propagate when the valves are opened and closed. The combustion loop, however, shows more variability. The maximum in-cylinder pressure differs by as much as 20%. This means that, for the simulation to be reliable, the pressure trace of the simulation should lie within the minimum and maximum values of the experiment.

Figure 3.5 presents the in-cylinder pressure measurement for each cylinder, averaged over 200 cycles. The difference in combustion pressure is less apparent, but the gas exchange loop is prone to variations at the end of the intake stroke. This is caused by the pressure waves coming from other cylinders through the intake manifold. It should however be noted that the difference is exaggerated by the logarithmic scale of the y-axis, such that the cylinder-to-cylinder variations can be considered negligible.

Despite the variability, the variations recorded in both graphs have a few similarities that can be used to calibrate the simulation to the measurement data. It seems that the in-cylinder pressure at bottom dead center (right limit) and top dead center (left limit) hardly changes between the cycles or the cylinders. Also the slope of the compression stroke, largely determined by the compression ratio of the engine, coincides and is therefore independent of the cyclic variations. The calibration of the simulation, treated in Section 3.3.1, is therefore based on these two remarks.

Another main assumption is that the cycles were run at a constant rotational speed of the engine. Since the main challenge of CNG is the simulation of turbulence, careful attention should be

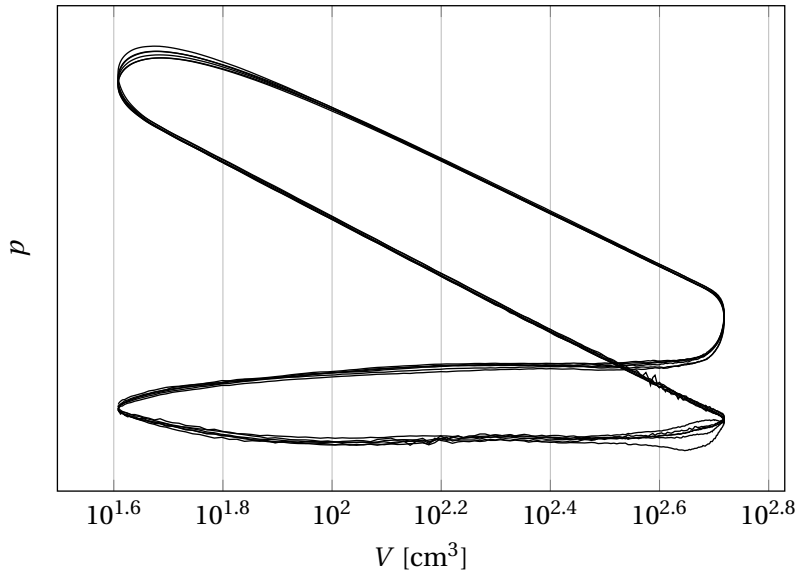

Figure 3.5: Cylinder-to-cylinder variations of cycle-averaged pressure

devoted to the formation of the mixture between the start injection and the start of combustion. The peak power operating point of the engine is the most critical in terms of mixture formation as very little time is available to form a homogeneous mixture, and it was therefore chosen to carry out the sensitivity analysis of different turbulence and combustion models. For this particular engine, peak power is achieved when the driver engages full throttle at a rotational speed of 6500 rpm. Nevertheless, this is only a small and very extreme condition in the operating envelope. To model the part load characteristics of the engine, and hence the normal driving characteristics on long stretches, a second operating condition was chosen at 2000 rpm and 2 bar mean effective pressure. This condition is more representative to study the formation of emissions. In the remainder of this chapter, the setup of the CFD method is based on the 6500 rpm operating point, thus referring to peak power. In Chapter 4, the scope is expanded to include both the 6500 and 2000 rpm conditions.

3.2 Base model setup

This section describes the configuration of the base model of the simulation, including the geometry preparation, the specification of boundary conditions and the considerations for grid generation of the moving boundaries. The software package CONVERGE that is used for the calculations is a general-purpose CFD solver developed by Convergent Science since 2008. The key feature of CONVERGE is the automatic grid generation process, where a stationary immersed-boundary mesh is generated at runtime. In addition, the presence of physical models connected to spray injection in the Eulerian-Lagrangian reference frame make the software package especially suitable for internal combustion engine applications.

The following sections describe the steps that have been taken to set up the base model of the simulation, and the key features of CONVERGE that distinguish it from other solvers.

3.2.1 Boundary conditions and initialization

The computational domain is depicted in Figure 3.6. The four evaluation planes that are highlighted with different colors are used in Chapter 4 to visualize certain parameters of interest. Since one isolated cylinder is simulated, the pressure and temperature boundary conditions are imposed directly at the intake and exhaust port. Pressure measurements at the test bench are done using static pressure probes. Applying static conditions at both boundaries however introduces a risk on numerical stability and divergence of the results. Indeed, since there was a slight amount of backflow into the

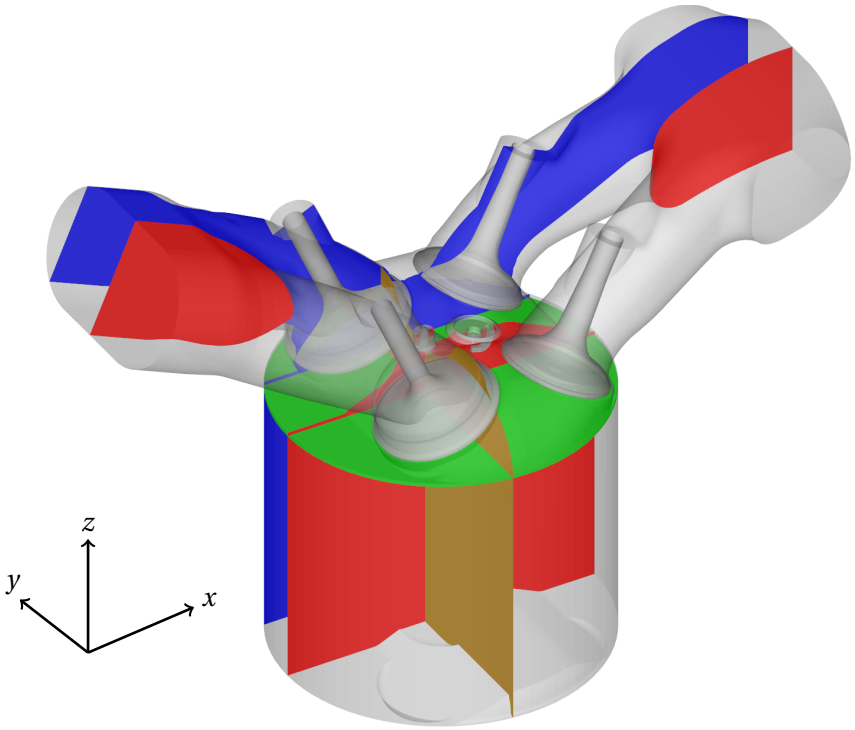

Figure 3.6: Computational domain including evaluation planes (left side: intake, right side: exhaust)

intake port, the simulation was found to be unstable with the static boundary conditions. Instead, the inlet condition was changed to total pressure, given by the profile in Figure 3.3a. At the exhaust, the static pressure was imposed. The remaining fuel inlet features a total pressure boundary condition with the constant value from Table 3.1. The temperature at the flow boundaries cannot be recorded during measurements, and reference values had to be obtained from a 1D-CFD simulation. A constant air composition of 79% N_2 and 21% O_2 (by volume) is assumed at the inlet, derived from the stoichiometric reaction in Equation (3.4).

The simulation is initialized at 120 degrees crank angle after ignition TDC, right before the exhaust valve opens. This moment was chosen because the large pressure difference between the cylinder and the outlet boundary is more dominant than the tumble motion that still exists inside the combustion chamber. Most of the existing turbulence is dissipated during combustion, therefore removing the influence on the rest of the engine cycle. Similarly to the boundary conditions, the initial pressure is obtained from the measurement, and the initial temperature from a reference 1D-CFD simulation. The initial CO_2 and H_2O concentrations are set according to the stoichiometric reaction in Equation (3.4), and any further reaction products are neglected for simplicity.

Table 3.2 shows the imposed wall temperatures for the surfaces bounding the computational domain. All values are obtained from a reference steady-state 1D-CFD simulation. As some of the surfaces are moving throughout the cycle, CONVERGE requires the creation of specific 'valve events', to make sure that none of the faces intersect each other. The valve motion is controlled by the profiles given by Figure 3.3b.

3.2.2 Grid generation

Even though the grid generation is done at runtime and thus isolated from the user, there are still plenty of options to control the final grid. CONVERGE supports grid embedding at certain boundaries or within specified volumes, either permanent or cyclic. Embedding in CONVERGE is done by specifying an integer that scales the grid relative to the base size Δ as

$$\Delta_{\text{embed}} = \frac{\Delta}{2^{\text{scale}}}. \tag{3.6}$$

Table 3.2: Wall boundary conditions

Boundary	**Motion**	***T* [K]**
Piston	Translating	560
Head	Stationary	540
Liner	Stationary	420
Intake port	Stationary	350
Exhaust port	Stationary	540
Intake valves (top)	Translating	460
Intake valves (bottom)	Translating	600
Exhuast valves (top)	Translating	740
Exhaust valves (bottom)	Translating	700
Spark plug	Stationary	750
Electrode	Stationary	950
Injector channel	Stationary	360
Injector valve (top)	Translating	420
Injector valve (bottom)	Translating	600

Despite being very user friendly, this formulation has the disadvantage that a moderate refinement by a factor less than 2 is impossible unless the base grid size is modified. This prohibits the comparison of different base grids and can thus have serious consequences on time step size, as is pointed out in Section 3.2.3.

The grid for the baseline simulation was constructed in a few stages. As initial step, a base grid was set up with a permanent fixed embedding of scale 2 on each boundary of the domain. The maximum lift of the injector is one order of magnitude smaller than the typical base mesh size, such that additional refinement is paramount to capture the large pressure difference between the injector rail and the combustion chamber. During the injection event, a cyclic maximum embedding of scale 4 is added at the injector seat to ensure a sufficient amount of cells in the channel. In addition, a cyclic fixed embedding of scale 3 is added within a cylinder shape around the injector to accurately capture the spray cone angle. Similarly, a sphere with a fixed embedding of scale 4 is added around the spark plug to record the chemistry occurring within the microscales. A more modest refinement of one level was added to the intake port and the cylinder region during the intake stroke. An image of the resulting base grid can be found in Figure 3.7. Depending on the turbulence model used, more regions of embedding were added in order to resolve the turbulent eddies and the turbulent flame position in regions of interest. In Section 3.4, this refinement is described in detail.

The innovative adaptive mesh refinement (AMR) technique that is available in CONVERGE takes embedding one step further by refining the mesh at the locations where the solver detects steep gradients in the flow field. A region of choice can be refined by specifying a maximum scale for embedding based on velocity and temperature gradients. This option is particularly suitable for cases in which the flow field is unknown a priori or very time-dependent.

Due to the spatial discretization of the domain, there are unavoidable discretization errors. By decreasing the grid size, however, one can find an optimum between computational time and accuracy. Ideally, the solution of the flow field should be independent of the grid size, and the grid is considered converged once a step in grid size does not change the solution significantly. The procedure that was followed to obtain a converged grid is explained in Section 3.3.2.

3.2.3 Time stepping algorithm

Time stepping in CONVERGE is done using a first order implicit finite difference scheme. The choice was made to enable a variable time step for the entire duration of the simulation. CONVERGE uses several formulations of the Courant-Friedrichs-Lewy (CFL) number to limit the time step size. It is a

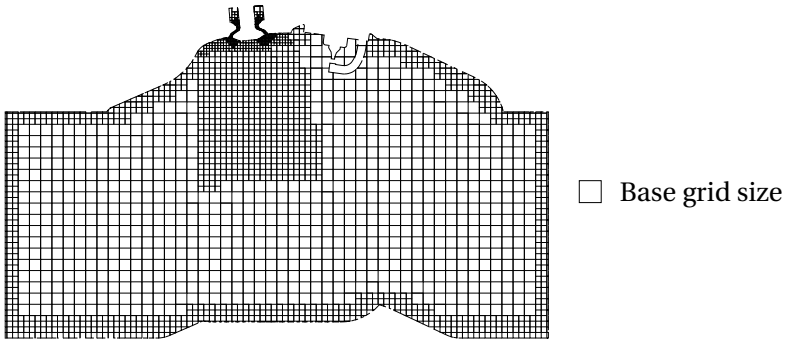

Figure 3.7: Base grid of the simulation during the intake stroke, showing the fixed embedding downstream of the injector

dimensionless quantity that, based on the Navier-Stokes equations, relates the local grid refinement to flow variables. By imposing a maximum allowed value to the CFL number, one can make sure that a quantity related to one fluid particle does not exceed more than one computational cell per time step.

During injection, the maximum CFL number is limited by the convective term of the Navier-Stokes equations. The convective CFL number can be expressed as

$$\mathrm{CFL}_c = u\frac{\Delta t}{\Delta x}. \tag{3.7}$$

Even though CFL numbers larger than one can be employed thanks to the unconditional stability of the implicit discretization scheme, the choice was made to set the convective CFL number to one for the RANS simulations. A slightly lower value of 0.7 was selected for the scale-resolving simulations, to decrease the second order temporal discretization error from the time stepping scheme Fluent Inc. [2006].

During combustion, the time step is mostly limited by the diffusive CFL number, defined as

$$\mathrm{CFL}_d = \nu\frac{\Delta t}{\Delta x^2}. \tag{3.8}$$

In general, the observed wall times of the simulations in this report were mostly limited by the CFL_c condition. The very small cell sizes around the injector seat combined with the large velocities through the channel resulted in time steps of 0.01 microseconds, leading to a total of more than 200,000 time steps for one engine cycle at 6500 rpm.

3.3 Verification and validation

In order to keep the simulation methodology as close as possible to the real-life conditions, the boundary conditions from the measurement were used to verify and validate the simulation results. The following steps were considered:

1. validation of the gas exchange and compression stroke by performing a calibration based on the measured in-cylinder pressure on a coarse computational grid;

2. verification of the computational grid, by performing a grid convergence study, taking into account the embedding of the injector, spark plug and the rest of the domain; and

3. validation of the air-fuel ratio by performing a calibration based on the stoichiometry of the measurement.

The next subsections elaborate upon these aspects.

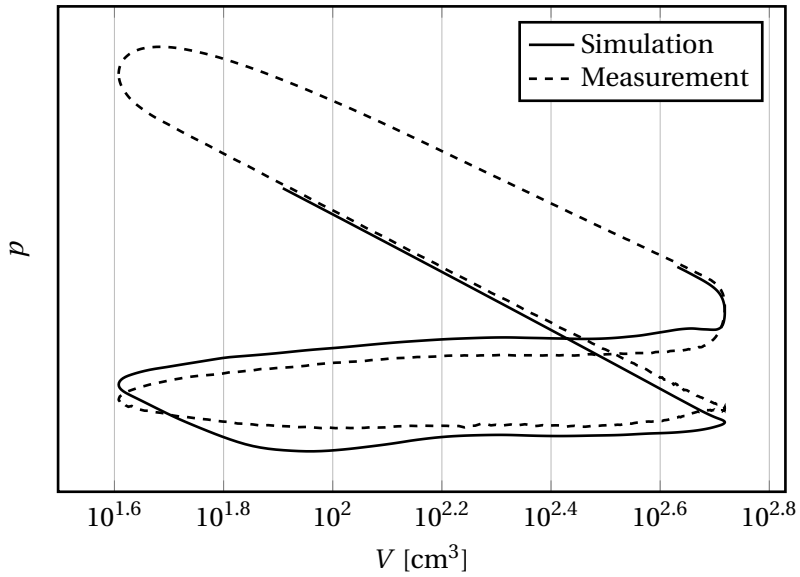

Figure 3.8: Log-log diagram of the in-cylinder pressure for the initial run with original boundary conditions

3.3.1 Calibration of the gas exchange

As introduced in Section 3.1, the calibration of the gas exchange is based on the cyclic variations obtained in the measurement. It was observed that the in-cylinder pressure at bottom dead center of the piston right before the exhaust stroke and the the top dead center right before the intake stroke are independent of the cycle or the cylinder for which they are measured. Additionally, the slope of the logarithmic p-V diagram should be identical between the simulation and the measurement.

Figure 3.8 shows the measured in-cylinder pressure of the first cylinder, averaged over 200 cycles. The second curve refers to the simulation result after specifying all boundary conditions in the experiment as they were presented in Section 3.2. A large disagreement between the two curves can be noticed. In fact, none of the above conditions are fulfilled, leading to a bad approximation of the real cycle.

Assuming nominal values for the species concentrations in the intake and exhaust at the start of the simulation, the in-cylinder pressure during the gas exchange is largely determined by the intake and exhaust port pressures. The latter two are once again shown in Figure 3.9. Referring back to the logarithmic p-V diagram, it seems that the exhaust pressure is overestimated and the intake pressure slightly underestimated. The reason for this is the location of the pressure probes in the experiment. The highly curved pipes upstream and downstream of the cylinder cause the pressure to drop significantly, leading to a deviation between the locations where the pressure is measured and imposed in the simulation. Taking this into account, the pressure measurements in Figure 3.9 were scaled around their mean value and translated in amplitude until the correct in-cylinder pressure was obtained. The resulting profiles are added with a dashed line to Figure 3.9.

In addition, the slope of the p-V diagram is overestimated by the simulation. The main factors that influence this inclination are

1. the compression ratio of the engine.

2. the heat transfer with the environment, possibly also influenced by the turbulence model; and

3. the species concentrations, since they determine the value of the polytropic coefficient κ;

The compression ratio of the engine can immediately be ruled out as contributing factor, as it is fixed by the experiment and confirmed by comparison between the measured and simulated in-cylinder

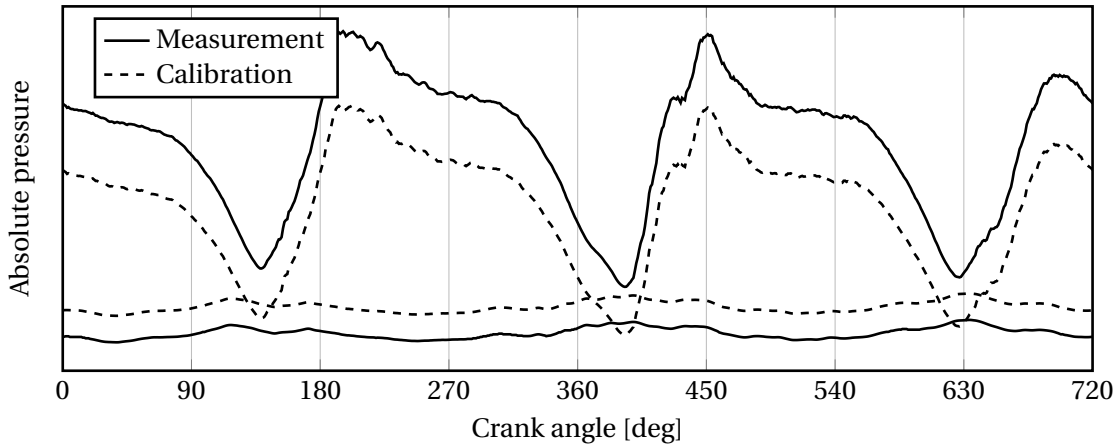

Figure 3.9: Original and calibrated pressure boundary conditions (upper: exhaust, lower: intake)

volume. In addition, several test cases were conducted with different wall temperatures and heat transfer models, and they did not cause any observable difference between the simulations.

A large deviation was however found between the polytropic coefficients of the simulation and the measurements. In an isotropic compression, the relation between pressure and volume can be expressed as

$$\frac{p_2}{p_1} = \left(\frac{V_1}{V_2}\right)^{\gamma}. \tag{3.9}$$

The isentropic coefficient γ takes the value 1.4 for air. For an internal combustion engine, in which the heat transfer with the walls overrules the adiabatic and reversible assumptions, the processes are referred to as polytropic, with corresponding coefficient $1 \leq \kappa \leq \gamma$. The simulation predicted the value of the polytropic coefficient to be 1.38; a reasonable value given the heat transfer between the walls and the gas. The value from the measurement corresponded to $\kappa = 1.31$. To obtain such low value would imply a drastic change in air concentration, such that the variation in species was not considered a plausible reason. Instead, the focus was shifted towards an inconsistency of the measurement rather than a simulation error.

A potential source for the different slope can be a measurement error of the top dead center location. The measurements are recorded time-based and converted to a crank-angle based format for further calculations. If the approximation for the top dead center location is slightly off, there exists a constant shift of the crank angle signal with respect to the pressure signal. It was found that a backward shift of three crank angle degrees is sufficient for the measurement error to be accounted for. Since the three physical parameters from the list did not seem to affect the diagram, it was assumed that the top dead center measurement was indeed the reason for the difference in slope.

Figure 3.10 shows the calibrated simulation, again in a logarithmic p-V diagram. By imposing the scaled pressure measurements to the simulation and the shift of minus three degrees to the measurement, a good agreement for the in-cylinder pressure during the gas exchange is obtained.

3.3.2 Grid convergence

The grid convergence for the RANS simulation is carried out by taking the base grid introduced in Section 3.2 and changing the base mesh size with increments of 0.5 mm. It should be noted that this step is explicitly carried out before the calibration of the injected fuel quantity, because it is assumed that the grid dependence can cause large deviations in air-fuel ratio. The following criteria were used to judge convergence of the grid:

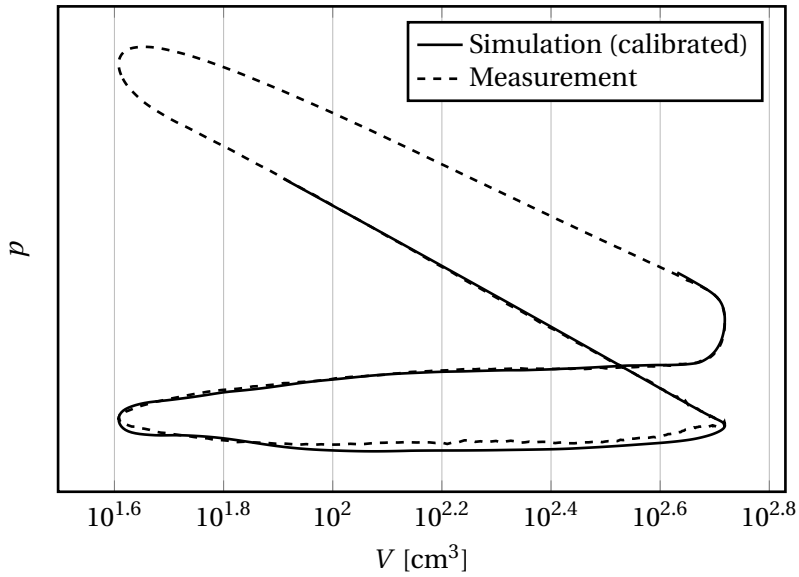

Figure 3.10: Log-log diagram of the in-cylinder pressure for the calibrated boundary conditions

C1. the dimensionless wall unit y^+ should lie within the constraints of the wall model;

C2. the mean air-fuel ratio shall not vary by more than 3% at the start of combustion;

C3. the velocity field shall visually look similar to discern tumble motions; and

C4. the amount of cylinder volume containing the most dominant air-fuel ratio shall not vary by more than 3% at the start of combustion.

In the following, all four criteria are elaborated upon, and a quantitative summary of the grid convergence can subsequently be found in Table 3.3. The error measures in criteria 2 and 4 were determined based on the cyclic variability in the measurement. Figures 3.4 and 3.5 showed that the peak pressure can vary as much as 20% between different cycles or cylinders. This variation should however be translated into the maximum allowable variation in air-fuel ratio. It is thus assumed that the air-fuel ratio is proportional to the heat release rate during combustion, which is in turn proportional to the change in pressure rather than its absolute value. Section 3.5 elaborates upon this relation. The variation of heat release between the different cycles was found to be 3%.

The dimensionless wall unit is defined as

$$y^+ = \frac{u^* y}{\nu}, \tag{3.10}$$

where u^* is the friction velocity at the wall and y the distance to the nearest wall. The value of y^+ describes how well the simulation resolves the boundary layer. Values lower than one are generally required to resolve the viscous sublayer, and therefore lead to extremely small cell sizes. Most turbulence models can be coupled with a wall model that, instead of resolving the sublayer, provides an approximation for it with empirical relations. For the RANS model, the standard wall function is used, which approximates the boundary layer with logarithmic functions. The LES makes use of the Werner-Wengle model instead, which uses power laws. Both models require $30 \leq y^+ \leq 100$ and they can thus be used to keep the computational time acceptable. Eventually, in internal combustion engine applications, one is less interested in accurately obtaining the boundary layer, but rather the mixing layers and the tumbling motion of the flow. The y^+ criterion is an important aspect of the base grid architecture treated in Section 3.2.2. In fact, the embedding scale at the walls of the domain was chosen such that the value of y^+ is always within the bounds of the wall model. For lower values of the embedding, slight variations of the amount of air entering the cylinder were observed.

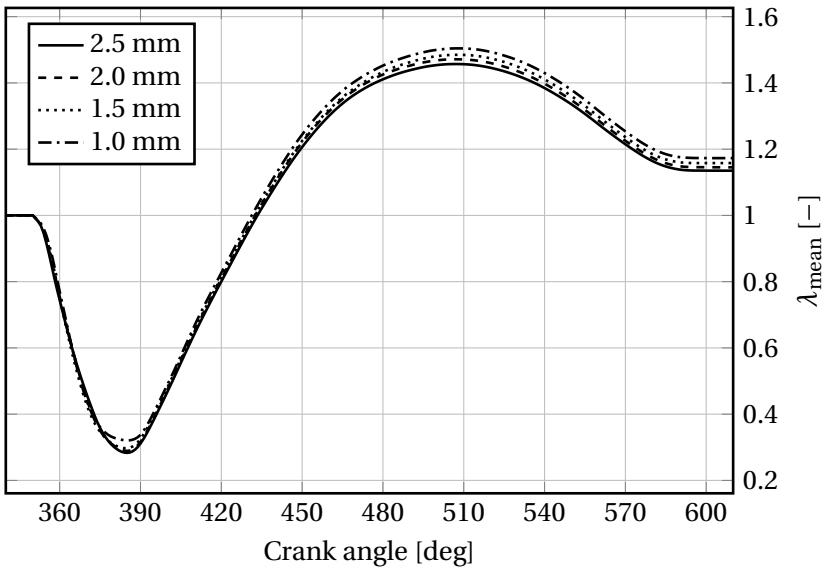

Figure 3.11: Evolution of the air-fuel ratio during injection for different base grid sizes

The second criterion is a direct consequence of the resolution of the injected fuel mass across the injector and the accuracy of the air flow through the intake port. Since the mass of air that enters the cylinder is grid-converged according to criterion 1, the bottleneck is given by the resolution around the location of the injector. Indeed, the fuel flow is overestimated for coarse grids, leading to a rich air-fuel ratio. This is confirmed by the Figure 3.11, where the history of the mean λ in the combustion chamber is plotted during the injection event. The difference is small (Table 3.3 provides the error magnitudes), and all four grids provide a good approximation.

Much larger deviations can be observed in Figure 3.12, where each grid is represented by two y-normal planes[4], one through the injector and one through a pair of valves. The snapshot is taken at 430 degrees, since this is the moment in the cycle where the injector is fully open, thus ruling out any of the transient effects of the start-up of the plume. When refining the grid from Figure 3.12a to Figure 3.12d, a velocity peak appears downstream of the injector, slightly inclined to the right due to the influence of the tumbling motion of the air intake. According to this criterion, the coarsest two grids can now be discarded since they produce a very different flow field compared to the fine grids. The difference between the 1.5 mm and 1 mm grid is less apparent since they both resolve the velocity peak at the injector and the detached flow field behind the intake valves. Even though the flow fields do not look identical, criteria 2 and 4 ensure that the error of the grid convergence is smaller than the deviation one would get by simulating multiple consecutive cycles. Moreover, since the 1.5 mm grid and the refinement at the injector already require serious computational effort, the 1.5 mm grid was chosen as baseline.

Finally, when considering the distribution of air-fuel ratio at the start of combustion, the relatively small difference between the 1.5 mm and 1 mm grids shows that the previous assumption is indeed justified. The 1.5 mm and 1 mm grid are able to predict both the values of the maximum volume fraction and their corresponding air-fuel ratio, while the coarser two grids clearly overestimate the former and underestimate the latter. In the lean part of the mixture ($\lambda > 1$) the predictions of the 1.5 mm and 1 mm grids are somewhat different, but it will be shown in Chapter 4 that this is an effect of the RANS turbulence model and, again, cyclic variations rather than the grid dependence.

[4] The location of the planes is defined in Figure 3.6.

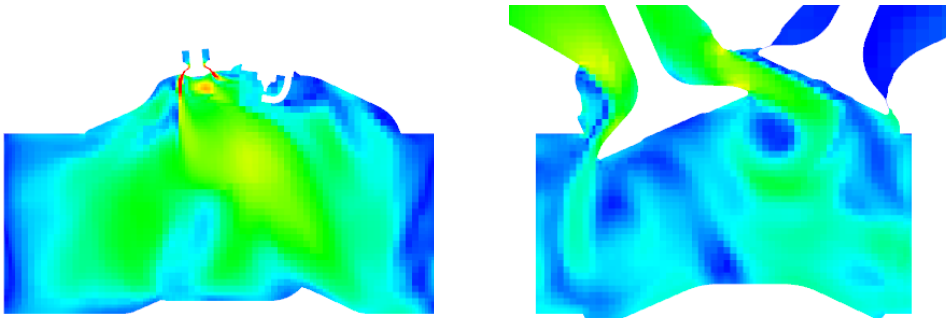

(a) 2.5 mm base size

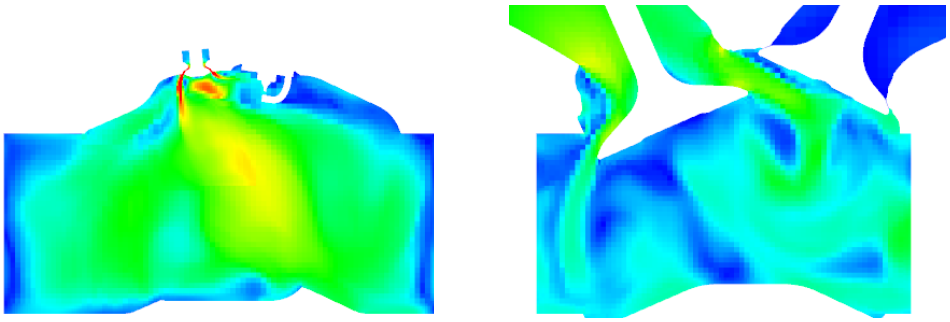

(b) 2 mm base size

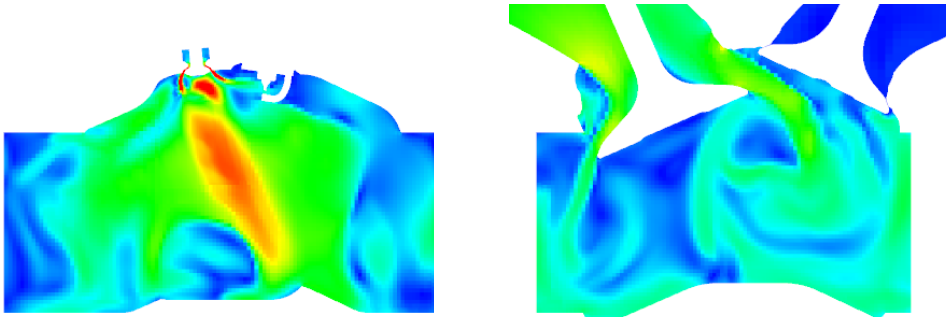

(c) 1.5 mm base size

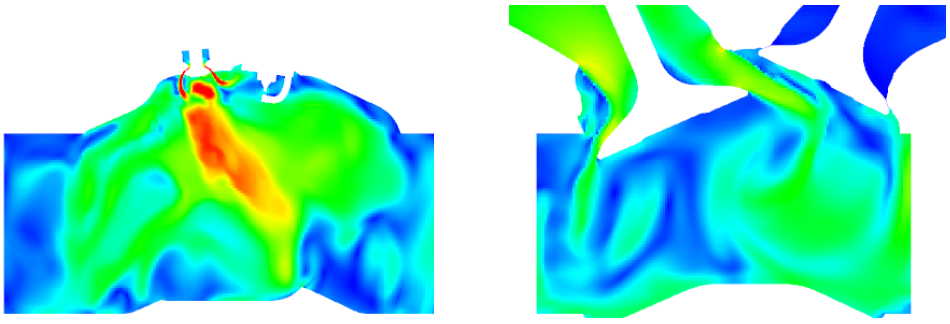

(d) 1 mm base size

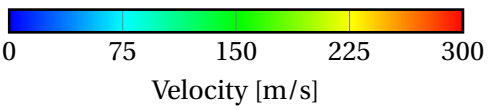

Figure 3.12: Visual effect of grid resolution on the velocity field at 430 degrees

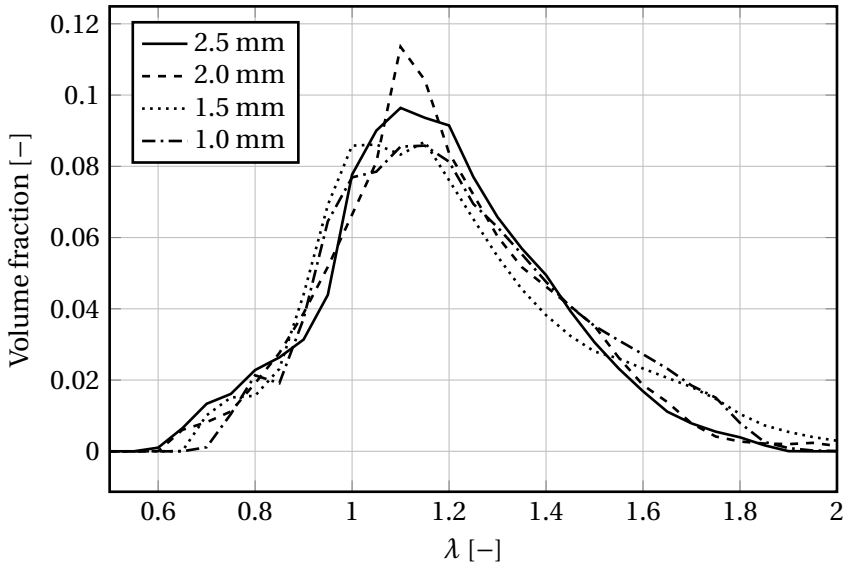

Figure 3.13: Distribution of air-fuel ratio in the cylinder at the start of combustion for different grid sizes

Table 3.3: Summary of grid convergence

Base size	Min cells	Max cells	Wall time	CPU	Rel. cost [%]	Error [%]	
						C2	C4
2.5 mm	400,000	850,000	46.2	72	7	3.23	32.33
2 mm	700,000	1.5 million	69.0	96	16	2.35	12.36
1.5 mm	1.4 million	3 million	118.3	144	34	1.28	1.29
1 mm	3.7 million	8.6 million	261.9	192	100	0	0

Table 3.3 provides a summary of the grid convergence procedure by including the grid sizes and the corresponding computational cost, calculated as the product of CPU and wall time, relative to the finest grid. The amount of minimum cells refers to the gas exchange top dead center, while the maximum amount of cells refers to the subsequent bottom dead center. The number of central processing units (CPUs) for each case was determined based on the amount of cells per CPU. For cases with large grids, having between 30,000 and 50,000 cells per CPU is the ideal choice to minimize inter-processor communication [Convergent Science, 2018]. For smaller grids where less CPU are needed, a smaller number of cells can be chosen for better speedup. Quantitative error measures for criteria 2 and 4 are given in the table as well. Both criteria are satisfied by the 1.5 mm grid when the 1 mm grid is chosen as baseline. Therefore there is no distinct advantage by choosing the 1 mm grid over the 1.5 mm, taking into account that the cycle-to-cycle variability in the simulation is most likely larger than this threshold. In addition, the threefold reduction in computational cost from the 1 mm to the 1.5 mm base size is an additional advantage.

3.3.3 Calibration of the injector

For intake or exhaust valves, the valve is considered in 'open' position when it exceeds 1 mm of lift, because there is only a relevant and measurable mass flow above this position. The injector has a maximum lift of only 0.36 mm, significantly below the measurement threshold. This means that a proper placement of the geometry in the simulation is crucial to obtain the correct mass flow from the injector. A injector profile has been approximated with reference to the valve profiles in Figure 3.3b. The ramp after the start of injection is assumed to have the same slope as the one of the air valves.

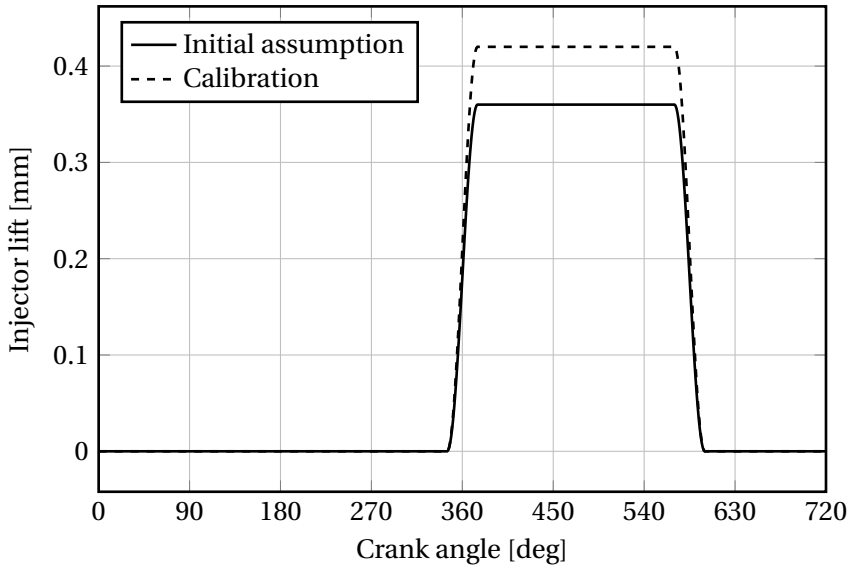

Figure 3.14: Assumed injector profile with original and calibrated lift

Figure 3.14 shows the initial assumption, indicated by the solid line.

As introduced in Section 3.2, the user is responsible for the proper placement of the valves in the geometry preparation phase. The valve should be positioned such that, at zero lift, the valve seat slightly intersects the cylinder head. CONVERGE then requires specification of a minimum lift value, and the valve event is opened as soon as the lift profile exceeds it. If the minimum lift is large enough, the valve is sufficiently far from the head to remove any intersections. The minuscule lift of the injector, however, introduces a significant risk on a wrong initial placement, as a slight misalignment has a large influence on the eventual valve lift. For this reason, the maximum valve lift was calibrated by monitoring the air-fuel ratio λ. It should be noted that the air-fuel ratio from the experiment is based on the amount of oxygen in the burned exhaust gases, and is thus measured downstream of the cylinder. The assumption is made that the same stoichiometric mixture is obtained in the cylinder.

The dashed line in Figure 3.14 shows the calibrated profile, which is just 60 microns larger than the initial value. It can be assumed that this difference is indeed a consequence of the initial misalignment of the valve.

3.4 Turbulence model setup

Referring back to Chapter 2, there are open questions regarding the choice of turbulence models, especially for direct-injection of gaseous fuels at high engine loads. In the present work, a comparative analysis is provided for two distinct modeling approaches: Reynolds-Averaged Navier-Stokes modeling and Large Eddy Simulation. The combination of both, leading to the hybrid Detached Eddy Simulation approach, is included as well for potentially providing LES accuracy at moderate computational cost. In the following, a motivation is given for the choice of the relevant submodels for this engine application, after which the configuration of the model and the computational grid is described.

3.4.1 Motivation

Ever since RANS and LES were first introduced, scientists have come up with a vast amount of submodels that are the best fit for a certain type of flow. It is not a straightforward task to find the most suitable model a priori, especially not when complex in-cylinder flows are considered. In the following, a series of arguments is presented that isolates the most promising modeling approach for each of the three turbulence models.

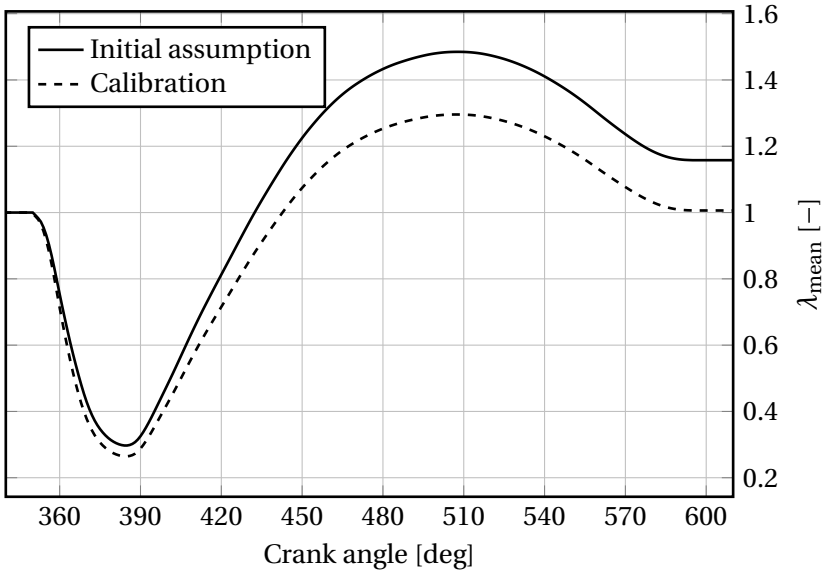

Figure 3.15: Air-fuel ratio during injection for the initial and calibrated injector lift

For the RANS simulations, the ReNormalization Group (RNG) formulation of the k-ε model was chosen [Yakhot *et al.*, 1992]. Chapter 2 introduced that the k-ε model is particularly suitable for high-Reynolds-number flows and performs well in the presence of free shear flows. The large velocities coming from the air intake and injection require such approach. It is important to resolve the energy-containing motions rather than the flow at the walls of the domain, such that the low-Reynolds-number k-ω and more expensive SST models are not considered. The RNG formulation is a good trade-off between computational time and accuracy for flows with a significant amount of swirling or tumbling motion [Fluent Inc., 2006; Han and Reitz, 1996].

The LES considered in this report uses the Dynamic Smagorinsky formulation. The dynamic form introduces a test filter on a lower wavenumber to locally change the model constant of the original Smagorinsky model. Since it is expected that the region downstream of the injector is slightly under-resolved, the model needs to be robust in case of anisotropic turbulence. As the Smagorinsky model assumes that the subgrid-scales are small enough such that their behavior resembles isotropic turbulence, the dynamic formulation was adopted to update the model constant under anisotropic effects, if necessary.

Finally, the Delayed formulation was adopted for the DES. This approach circumvents the largest drawback of the DES technique, namely grid-induced separation in the boundary layer, by including information on viscosity to make the transition from RANS to LES. It should be noted that the implementation of DDES in CONVERGE is based on the two-equation k-ω SST RANS model of Menter [1993].

3.4.2 Grid considerations

RANS and LES-like methods are based on different physical principles, and thus require special attention when constructing the grid. In general, an LES requires a grid size that is able to resolve all energy containing motions in the flow field, since most modeling approaches are based on the Kolmogorov scaling in the inertial subrange. A DES grid looks similar to the LES in detached flow regions, since it should provide sufficient dissipation in the microscales. In attached flow regions such as the walls of the domain, the spacing can be coarser for the DES. As mentioned before, for comparability of the results and restriction of the minimum time step, the base grid size was fixed to 1.5 mm for all models.

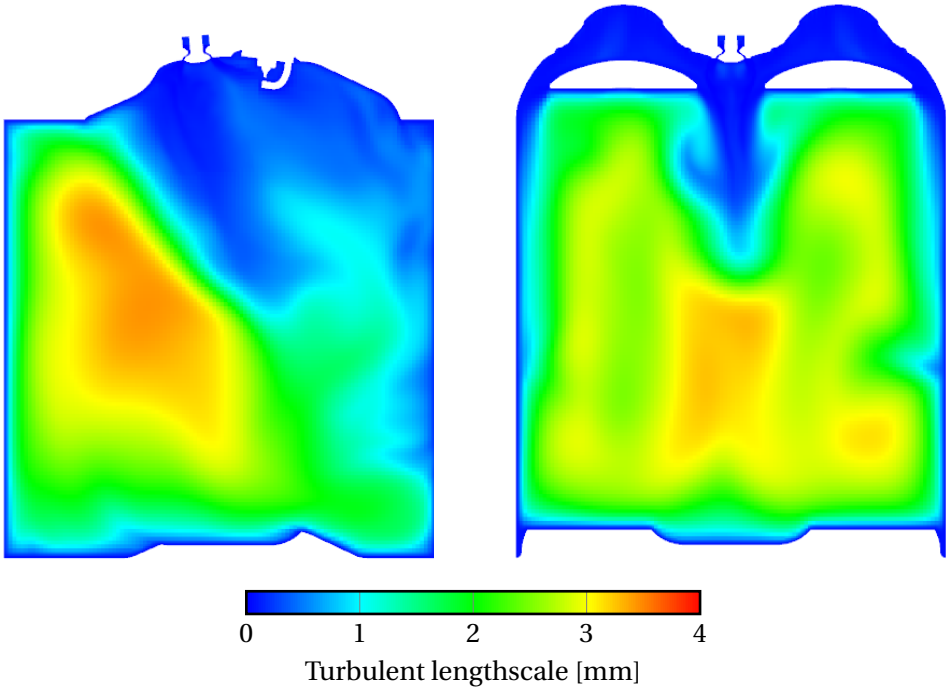

Figure 3.16: Turbulent lengthscales obtained from a RANS simulation during the intake stroke

An initial run of the grid-converged RANS simulation was used to determine the LES grid size a priori. The turbulent lengthscale in Figure 3.16 is obtained from the RANS model according to

$$\ell_{k\varepsilon} = C_{\mu}^{3/4} \frac{k^{3/2}}{\varepsilon}. \tag{3.11}$$

The turbulent lengthscale $\ell_{k\varepsilon}$ is directly proportional to the integral scale L for isotropic turbulence. For in-cylinder flows, however, the macroscopic turbulence is highly anisotropic due to the flow separation and the mixing layers. Han and Reitz [1996] performed a comparison of the $\ell_{k\varepsilon}$ lengthscale to an experimentally obtained integral lengthscale, and concluded that, even though the time-wise approximation was unsatisfactory, both values seemed to lie between the same limits.

In Figure 3.16, the largest eddies, representing the integral scales of the flow, have sizes of about 4.5 mm. Referring back to the definition of Pope [2000] in Equation (2.5), the lengthscale ℓ_{EI} demarcates the energy-containing range from the inertial subrange and is approximately one sixth of the integral scale. The ℓ_{EI} for this in-cylinder flow thus lies around 0.75 mm. According to the Nyquist-Shannon sampling theorem, one needs at least two cells within this wavelength in order to properly resolve its direction[(5)] [Ziemer *et al.*, 2013]. The corresponding cell size of 0.375 mm is obtained by applying an embedding with scale two to the entire computational domain. As opposed to the RANS, the LES grid is equidistant in all directions, such that the entire combustion chamber has the same cell size (apart from the extra embedding at the injector). The cells were coarsened by one level during the exhaust stroke since the turbulent lengthscale is larger and less accuracy is required.

The DDES requires a resolution that is similar to LES in the detached regions where the LES mode is activated. The assumption was made that the diffusive mixing is controlled by the smallest scales of the flow. Therefore, the mixing is dominant in the flow regions where there are steep velocity gradients due to the interaction of the smallest eddies. The AMR setting was activated with minimum grid size equal to the LES resolution in order to resolve those steep gradients with grid refinement, and to keep the mesh coarse away from the mixing layers. The AMR is triggered once the subgrid-scale velocity is

[(5)] For lower order spatial discretization schemes, more cells are required but could not be achieved due to computational constraints.

Table 3.4: Summary of embedding for each turbulence model

	RANS	**LES**	**DES**
Injector	4	4	4
Spark plug	4	4	4
Detached regions in cylinder	1	2	1-2
Walls	1-2	2	1-2

above 1 m/s. Flow regions outside the mixing layers thus remain coarse and the DES locally switches to its RANS mode. This way, the total grid size remains acceptable.

Table 3.4 provides a brief summary of the differences in embedding for the RANS, LES and DES setup. The most notable difference is observed in the detached regions, where the LES has half the cell size of the RANS simulation, leading to a steep increase in cell count.

3.4.3 Turbulent mixing

Apart from the use of turbulence models, the mixing of gases is determined by global transport parameters. In Chapter 2, the importance of the turbulent Schmidt number, defined in Equation (2.13), has already been indicated for in-cylinder flows. The dimensionless number is a measure for the relation between turbulent viscosity and eddy diffusivity in the flow. By default, a value of $Sc_t = 0.78$ is specified by CONVERGE, although the literature presented in Chapter 2 indicated that it is impossible to fix a universal value for the turbulent Schmidt number. The values are therefore lowered systematically to study the importance of molecular diffusion in the mixing layers.

3.5 Combustion model setup

CONVERGE offers a variety of combustion and chemistry models for different purposes. Based on the literature presented in Chapter 2, the relevant models for this engine configuration are selected. Next, a brief description is given for the variables used to judge the modeling of the combustion phase in Chapter 4. Finally, the construction of the Borghi diagram is treated according to the theory presented in Chapter 2 and a 1D premixed combustion simulation.

3.5.1 Motivation

For general combustion applications, CONVERGE recommends the SAGE detailed chemistry solver, introduced in Chapter 2, to calculate the chemical reaction rates based on the Arrhenius relation. In conjunction with the GRI-Mech 3.0 reaction mechanism for CH_4, the model should be able to provide an accurate prediction for the ignition delay and heat release rate, although the method may be more expensive than other combustion models.

To provide computationally less expensive alternatives, the comparison will be made between SAGE and the premixed G-equation combustion model. The method is very efficient in tracking the flame front, but can only be trusted when the turbulence is weak enough to prohibit flame quenching. As opposed to the SAGE chemistry model, it relies on calibration for a particular engine configuration.

Similarly to the grid convergence study presented in Section 3.3.2, the influence of grid resolution on the heat release was investigated for all models. Since the location of the flame front over time is unknown, the AMR method was used to locally refine the mesh at the flame surface based on steep gradients of temperature. The base size of the mesh had already been fixed to 1.5 mm, so the only way to study the accuracy of the methodology was by assessing different embedding levels for the AMR. It was found that an embedding level of 5 is necessary for both SAGE and G-equation to fully capture the flame propagation. This goes against the claims from Cornolti [2015] and Manz [2016], in which they stipulated that the G-equation can run on a coarser grid.

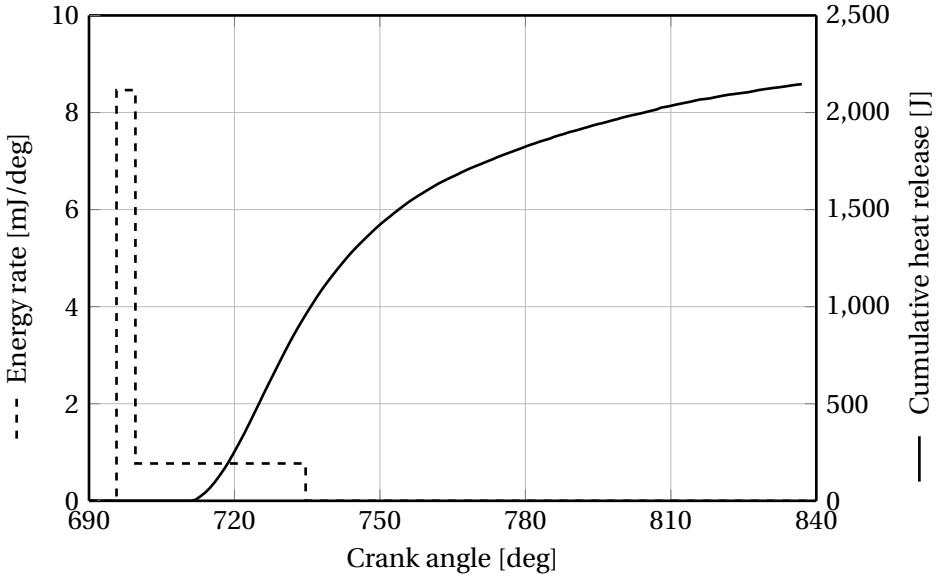

Figure 3.17: Pressure-based cumulative net heat release and corresponding spark profile

3.5.2 Calibration of pressure and heat release

The combustion is initiated by a spark, fixed by the measurement at 24.3 degrees before the ignition top dead center. Taking into account the time-delay of the measurement signal, as elaborated upon in Section 3.3, an additional forward shift of 3 degrees is taken into account, such that the spark timing is set to −27.3 degrees. The spark is modeled as a heat energy source with the rate profile specified in Figure 3.17 [Battistoni *et al.*, 2015; Mitianiec, 2012]. The total duration of the spark was taken as 1 ms (39 degrees), adding a total amount of energy of 60 mJ. The first peak of the profile, where half of the energy is added during 10% of the total duration, represents the arc phase of the plug, while the remainder of the discharge models the glow phase. It should be noted that the spark timing is the time of electronic discharge of the spark plug, and not the time when combustion starts. A critical evaluation of the ignition delay is thus necessary, as it might differ significantly between the models.

The accuracy of the combustion models is judged by evaluating the cumulative heat release from the moment the combustion starts. The gross heat release rate of combustion contains contributions from the internal energy of the fluid, the heat transferred to the engine walls and the work done by the fluid to the environment [Heywood, 1988]. It can be shown that the latter component, referred to as the net heat release rate, can be calculated based on the pressure and volume in the cylinder:

$$\frac{\mathrm{d}Q_{\mathrm{net}}}{\mathrm{d}\theta} = \frac{\gamma}{\gamma-1} p \frac{\mathrm{d}V}{\mathrm{d}\theta} + \frac{1}{\gamma-1} V \frac{\mathrm{d}p}{\mathrm{d}\theta}. \tag{3.12}$$

The data from the measurement are provided cumulatively in Figure 3.17 by the solid line.

The net heat release rate is closely connected to the lower heating value (LHV) of the fuel. The LHV is the amount of heat that is released by the chemical reaction in Equation (3.4), excluding the heat of vaporization of the water in the combustion chamber. The value of the measurement was fixed to 48.55 MJ/kg. In engine simulation, however, this quantity is commonly regarded as a calibration parameter, should the net heat release be poorly approximated.

3.5.3 Flame regime diagram

As mentioned earlier in this section, the G-equation model is not guaranteed to provide meaningful solutions when the turbulence around the spark plug is too dominant. Referring back to the Borghi diagram in Figure 2.2, this limit corresponds to the DNS by Meneveau and Poinsot [1991], above which none of the flamelet modeling approaches are valid. In order to justify the model choice, a Borghi

Table 3.5: Laminar flame properties at spark discharge, obtained with a 1D FlameMaster calculation

	2000 rpm	**6500 rpm**
In-cylinder pressure	6 bar	40 bar
In-cylinder temperature	730 K	720 K
Laminar flame speed	105 cm/s	45.9 cm/s
Laminar flame thickness	73.1 μm	21.0 μm

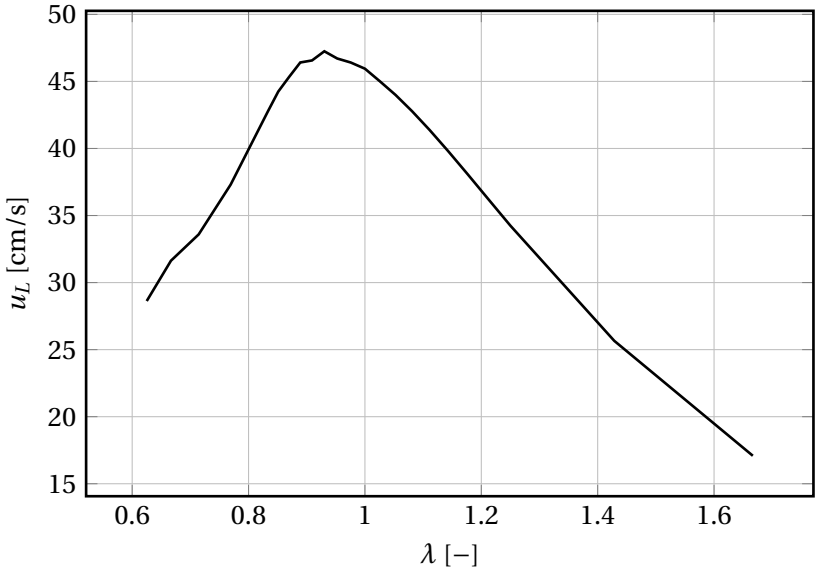

Figure 3.18: Laminar burning speed for different air-fuel ratios at peak power, obtained with a 1D FlameMaster calculation

diagram is therefore constructed based on the results of the SAGE detailed chemistry solver.

The turbulent intensity u' and the integral lengthscale L have been obtained directly from the RANS turbulence model. As outlined in Section 3.4, these quantities can in general not be compared since the calculation method assumes isotopric turbulence. However, the main purpose of the analysis is to get the correct order of magnitude rather than a precise value.

The 3D simulation in CONVERGE is however not able to capture the thickness of the flame ℓ_f and the corresponding laminar burning speed u_L at which the flame front propagates through the combustion chamber. The academic 1D code FlameMaster has been used to provide these values at the relevant pressure and temperature during the start of combustion. FlameMaster is developed by Pitsch [2018] at the Institute for Combustion Technology of the RWTH Aachen and uses chemical reaction mechanisms to calculate a vast amount of flame properties. For these particular calculations, the same GRI-Mech 3.0 mechanism with its corresponding thermal and transport properties has been used to provide consistency between the 1D and 3D simulations. A fully premixed and unstretched laminar flame was assumed with a stoichiometric air-fuel ratio. Table 3.5 shows the values of the pressure and temperature in the combustion chamber at the time the spark plug is discharged, and the corresponding flame speed and thickness.

Apart from the flame properties at the start of combustion, the sensitivity of the flame on the air-fuel ratio was studied. Local pockets of rich or lean mixtures around the spark plug have a significant influence on the burning speed of the flame, as Figure 3.18 indicates. The flame speed reaches its maximum at a slightly rich air-fuel ratio of 0.93. If the fuel mixture is inhomogeneous at the time of discharge, the distribution of the fuel will thus have an influence on the flame speed and position, and therefore also the heat release to the environment.

4

Results and discussion

The computational methodology for the simulation of direct-injection spark-ignition engines has been built up in Chapter 3. During the base model setup, careful attention was paid to the accurate representation of reality by calibrating the boundary conditions to measurements from the engine test bench. Whether or not those assumptions result in a predictive CFD model is evaluated in this chapter by looking at several model choices, stating the differences between them and indicating potential causes.

The present chapter is built up according to the flowchart in Figure 4.1. Starting with the computational methodology and corresponding considerations from Chapter 3, a variety of parameters have been analyzed, and their influence on the engine cycle have been noted in terms of three global phenomena: mixture formation, combustion and performance of the engine.

Referring back to the observations of Twellmeyer *et al.* [2017] from Chapter 2, the four criteria that affect the simulation of the mixture formation are grid refinement, the turbulence model, the turbulent Schmidt number and the initial turbulent field. Having done the grid convergence study of Chapter 3, the refinement criterion can be eliminated from the list. The remaining three are treated in Sections 4.1 to 4.3, respectively. Here it is assumed that adaptation of the initial turbulent field in the engine corresponds to the variability of several consecutive engine cycles. Some remarks on the use of different chemistry and combustion models are included in Section 4.4. The aforementioned sensitivity analyses are subsequently summarized in Section 4.5. With the final model setup, the 2000 rpm operating point is considered in Section 4.6. The analysis aims to generalize the findings and draw conclusions regarding the predictivity of the methodology for CH_4 combustion.

4.1 Turbulence model study

Perhaps the most critical element that affects the mixture formation is the choice of turbulence model. In Chapter 3, three different models based on three different underlying physical principles were introduced and configured in CONVERGE along with the proper grid considerations. This section presents the resulting flow field, considering clip planes of velocity, fuel concentration and the distribution of air-fuel ratio to assess the quality of the mixture formation. Furthermore, the differences in flame speed and heat release during combustion are elaborated upon based on the available measurement data.

4.1.1 Mixture formation analysis

The grid convergence study in Chapter 3 already indicated that the large velocity gradients induced by the outward-opening injector are difficult to capture. The same clip planes, this time showing the difference between the RANS, LES and DES models at 480 degrees, can be found in Figure 4.2. The rightmost cut shows how the fast-traveling stream of air from the intake port passes the upper side

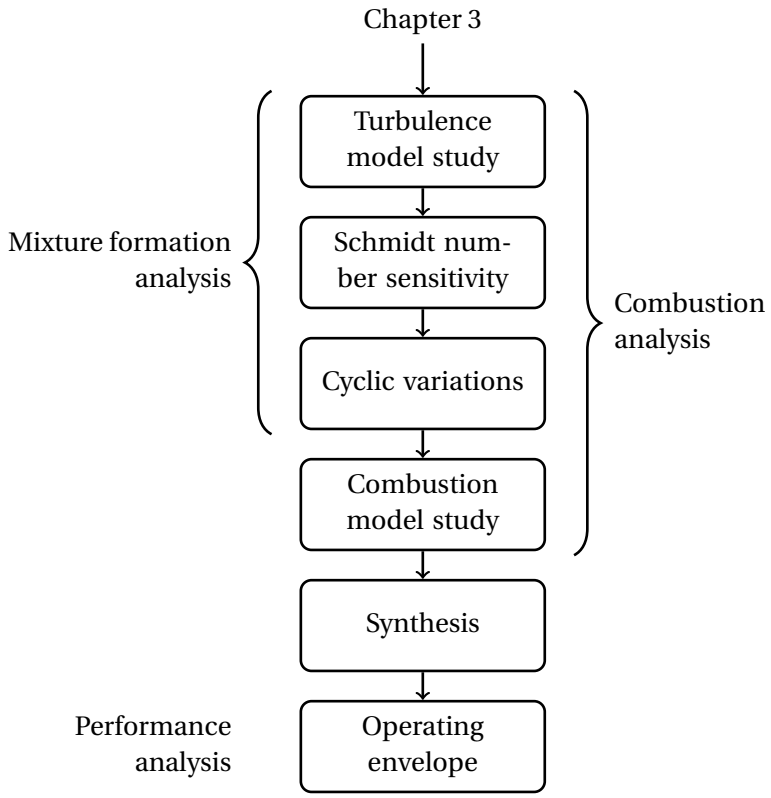

Figure 4.1: Breakdown of Chapter 4

of the valve and separates at its trailing edge. The absence of flow on the lower side of the valve creates a rotating motion in the combustion chamber, often referred to as tumble. All three turbulence models show a similar visual approximation of the mean velocity of the vortex core, although the LES and DES contain more instantaneous velocity fluctuations in the separated wake downstream of the valve. When assessing Figure 4.3, however, it becomes clear that there exists a large difference between the tumble ratio of the scale-resolving and the RANS simulations. The tumble ratio presented here is the magnitude of rotational velocity due to the flow separation over the valve, normalized by the rotational speed of the crankshaft. The fluctuations of the scale-resolving simulations capture a tumble ratio that is as much as 30% larger in magnitude than the RANS at 480 degrees, and an equal underestimation at 640 degrees. Even though macro effects are not responsible for the turbulent diffusion and therefore the mixing process, they control the location of rich and lean zones at the start of combustion which may, in turn, influence the burning speed of the flame.

As the discussed literature showed a consistent disagreement between RANS and LES for the penetration of the spray in the combustion chamber, the fuel concentration clip planes for the three turbulence models are depicted in Figure 4.4. It was found that at the start-up of the fuel jet at 350 degrees there is a slight difference between both jets, but as the long-term characteristics of the fuel jet are more dominant for the mixing, the choice was made to show the clip planes at 480 degrees where the tumble ratios for RANS and LES are significantly different. The picture shows that the jet is inclined towards the exhaust ports under influence of the circulation in the combustion chamber. The shape of the streams is nevertheless very similar, and the same penetration length and spray cone angle are obtained despite the claims from literature.

The fuel mixing is best investigated by means of the air-fuel ratio λ. Figure 4.5 provides the time history of the λ distribution in the combustion chamber during the intake stroke and the majority of the compression stroke. For a clear comparison at time the spark is ignited, the volume fractions at 690 degrees have additionally been plotted in Figure 4.6. When the fuel injection starts at 345 degrees,

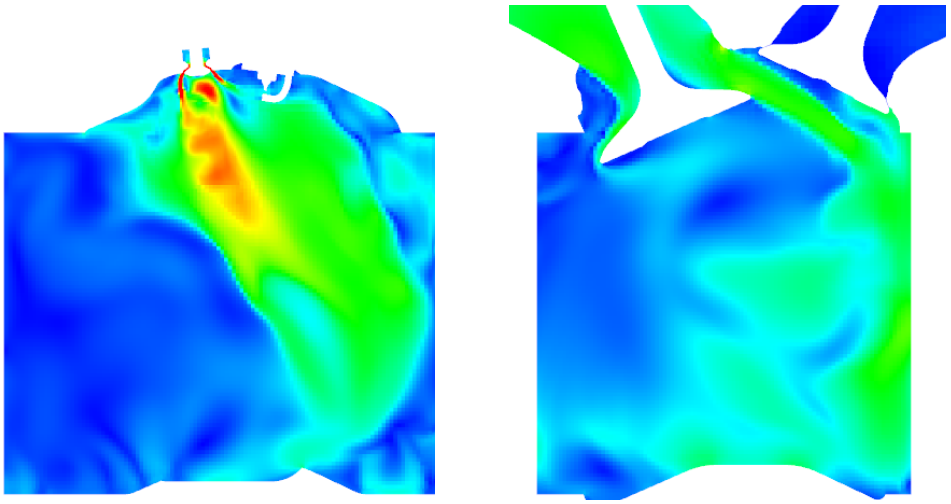

(a) RANS RNG k-ε

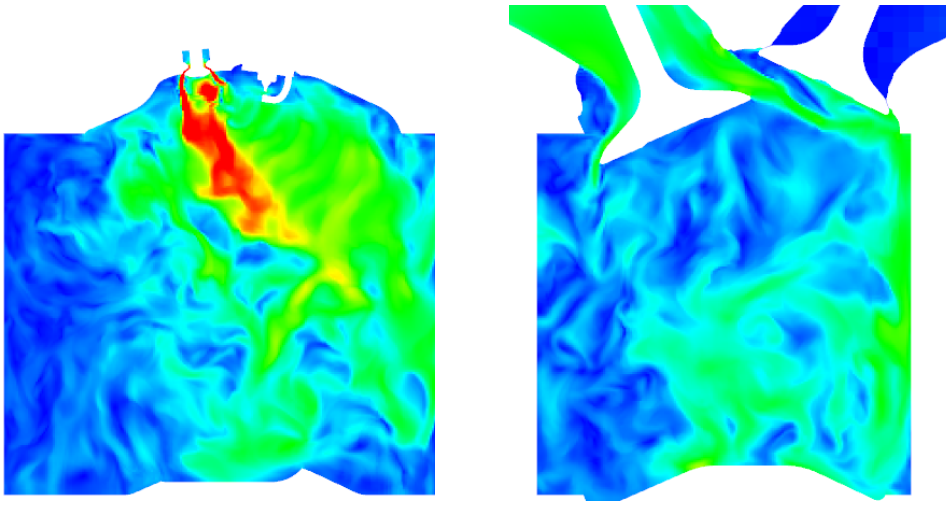

(b) Dynamic Smagorinsky LES

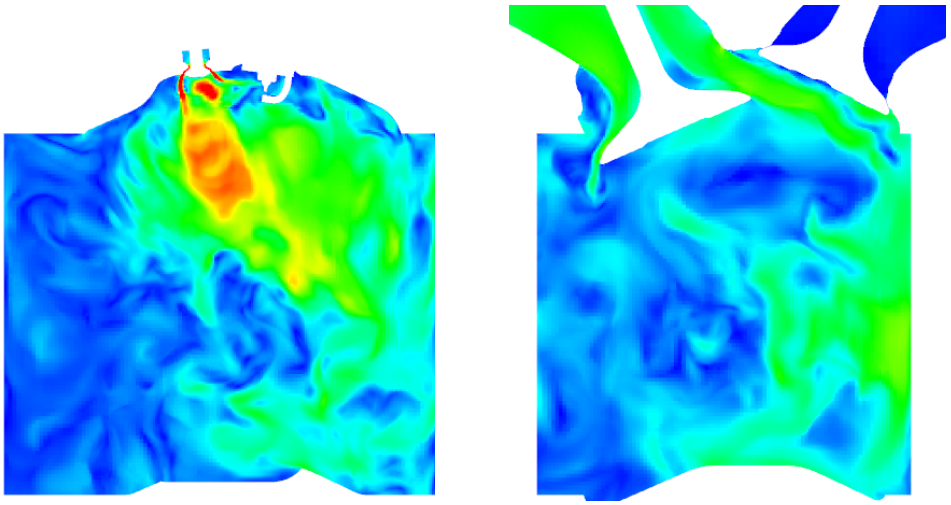

(c) Delayed DES

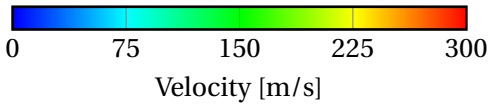

Figure 4.2: Comparison of resolved velocity fields at 480 degrees produced by different turbulence models

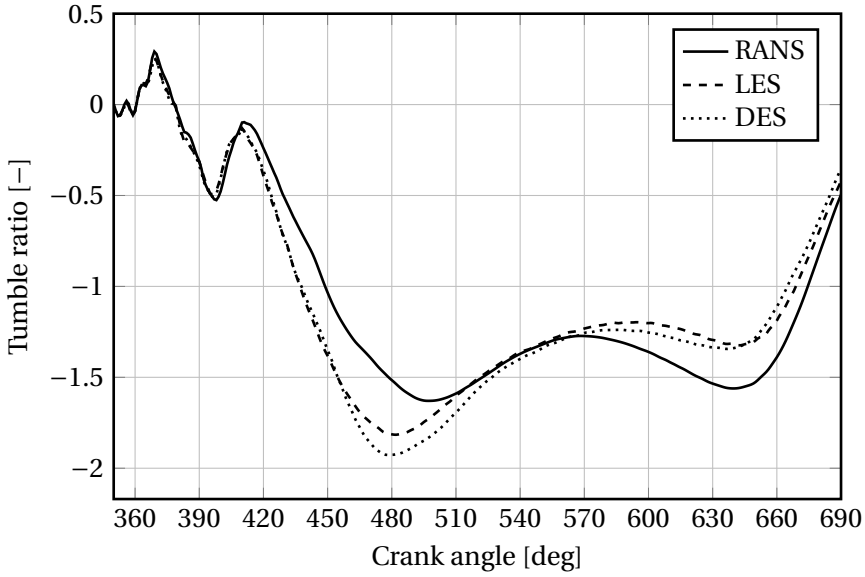

Figure 4.3: Comparison of tumble ratio for different turbulence models

the combustion chamber is entirely filled with residual exhaust gases[6]. As soon as the injector opens, large quantities of fuel enter the combustion chamber, locally resulting in a very rich volume for a short amount of time. Shortly after the start of injection also the intake valve is opened, which brings the air-fuel ratio back towards unity. The intake valve and injector effectively close around 580 degrees and 600 degrees, respectively, after which the mean air-fuel ratio stays constant, but the distribution of the volume approaches 1 as the fuel mixes further with the air. Ideally, one wants to obtain a completely homogeneous mixture at end of the graph, such that the flame is not restricted by local pockets of rich or lean zones.

A large difference between the RANS and LES simulations is immediately apparent. Figure 4.5b depicts a gradual and smooth transition over time, and it produces a near stoichiometric mixture at the start of combustion with a small spread. The RANS in Figure 4.5a features a discontinuity between roughly 450 and 520 degrees that is not present in the LES, and the eventual distribution is less ideal. This confirms the recurring hypothesis from the literature study that the RANS is less capable of predicting turbulent mixing, as modeling of the entire turbulence spectrum results in an underestimated dissipation rate.

The prediction of the DES is similar to the LES for the majority of the time, although the solution starts to diverge from 650 degrees onward. The reason for this is the decreasing amount of velocity fluctuations as the piston reaches top dead center. The adaptive mesh refinement is not triggered anymore since the velocity gradients disappear, and the coarse cell size locally switches to RANS mode. As Figure 4.5a clarified earlier, the final stage of the mixing is thus worsened, resulting in a larger spread to the lean regime compared to the LES.

Taking a closer look at the Figure 4.5a, the discontinuity can be explained by considering the local distribution of air-fuel ratio inFigure 4.7. The ensemble-averaged flow field shows a rich zone that is mostly centered in the plane underneath the injector and partially downstream of the valves. The edges of the combustion chamber are hardly visited by methane. The resolved fluctuations in the LES, on the other hand, result in a more homogeneous distribution of rich and lean zones, and the dispersion of the fuel to the chamber walls is considerably more symmetric. The contact area between mixed and unmixed regions is thus larger, and a more gradual development of the mixture formation is promoted. The DES preserves the symmetry, although the location of the rich pockets is moved downward.

[6] As a convention, the initial value of the air-fuel ratio is equal to 1, assuming that the combustion of the previous engine cycle is completely stoichiometric.

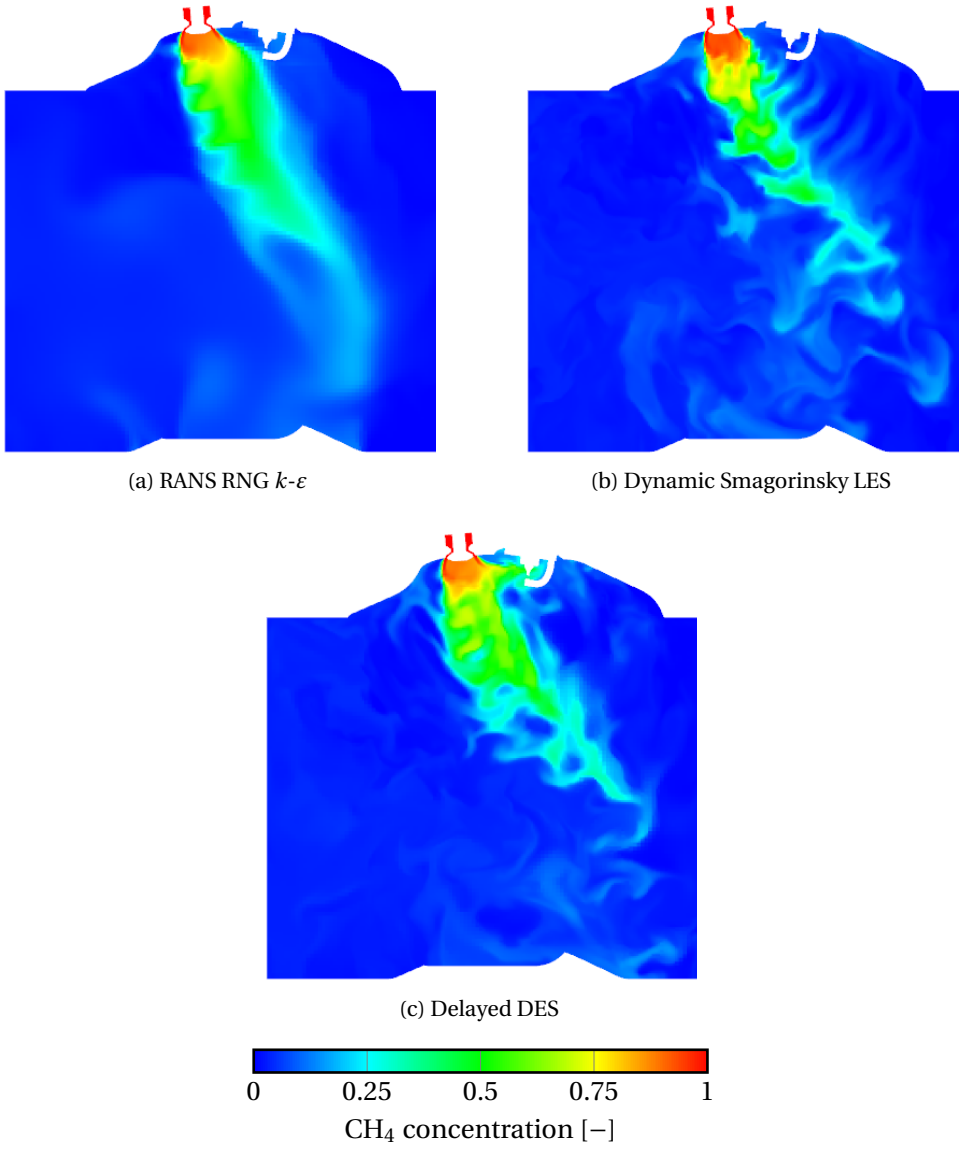

(a) RANS RNG k-ε

(b) Dynamic Smagorinsky LES

(c) Delayed DES

Figure 4.4: Comparison of fuel penetration at 480 degrees produced by different turbulence models

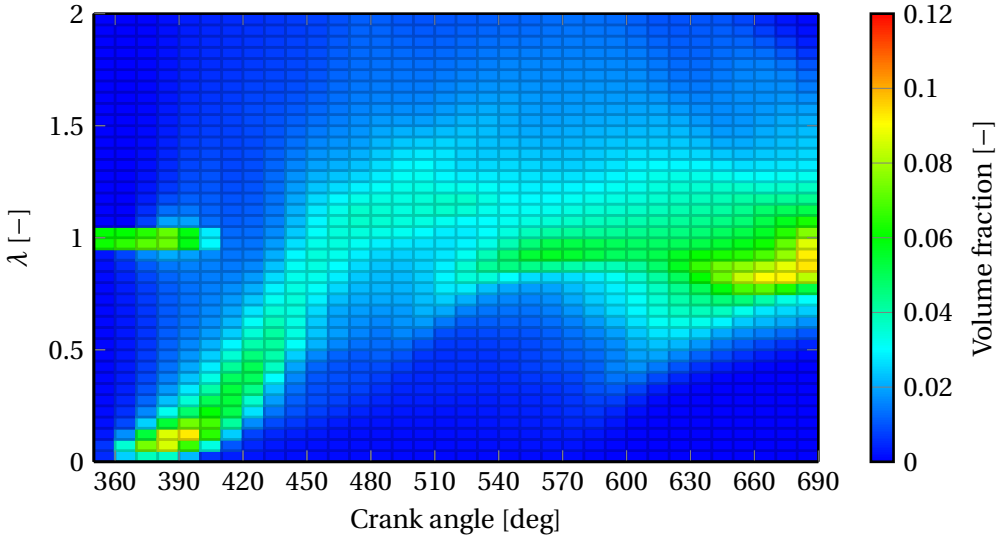

(a) RANS RNG k-ε

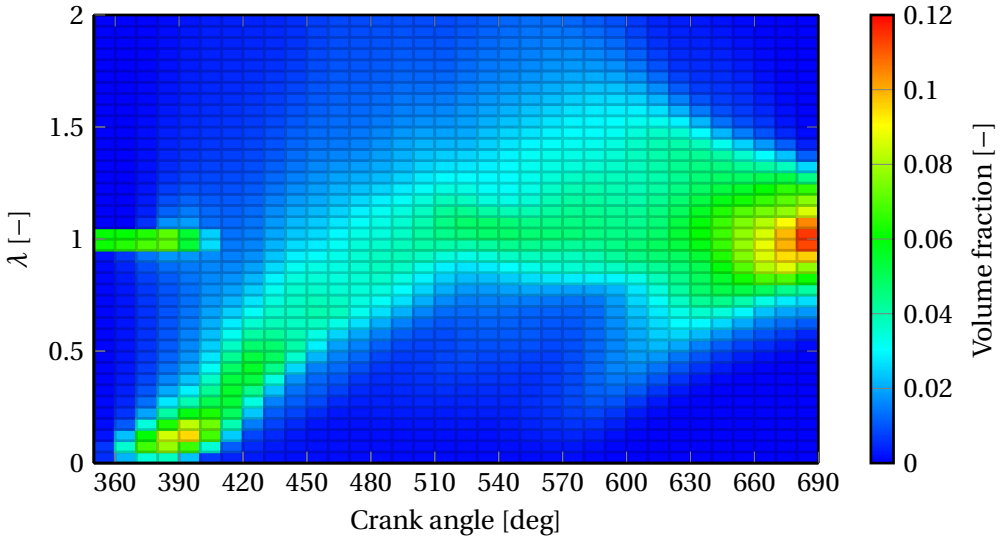

(b) Dynamic Smagorinsky LES

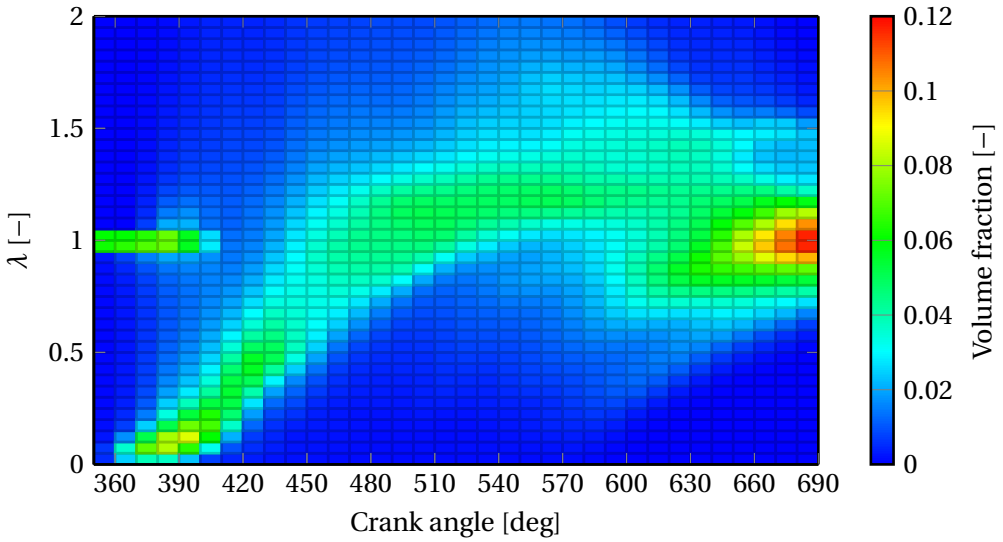

(c) Delayed DES

Figure 4.5: Contour plot of λ distribution during the intake and compression stroke

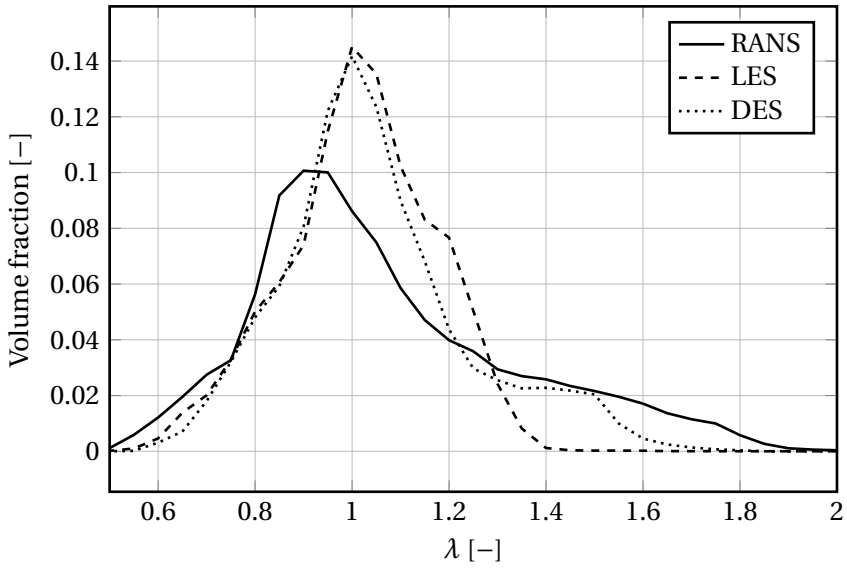

Figure 4.6: Distribution of air-fuel ratio at spark discharge for different turbulence models

Table 4.1: Time consumption of turbulence models during gas exchange (120 to 690 degrees)

Model	**Maximum cells**	**Maximum CFL**	**Wall time [h]**	**CPU**	**Rel. cost [%]**
RANS	3.0 million	1.0	125.6	144	100
LES	12.4 million	0.7	355.4	240	470
DES	5.7 million	0.7	230.4	192	250

Whether or not the LES produces a more reliable mixture formation is hard to justify without additional measurements of the flow field in the engine. The more realistic λ distribution in Figure 4.7b however suggests that the presence of fluctuations indeed improves the predictivity of the simulation. The accuracy of LES however comes at a price. The large cell count increases the computational cost of the gas exchange by almost five times compared to RANS, as Table 4.1 indicates. Compared to the article of Som *et al.* [2012] that was presented in Chapter 2, this increase is smaller than expected. The limiting factor for simulation time is thus not the cell count, but rather the injection duration, leading to very small time steps when the (convective) CFL condition is activated. Even though the accuracy is potentially improved by the LES, the current resources do not yet allow the fast generation of results. The best alternative is still given by the DES, yielding LES accuracy while preserving a moderate computational cost of 2.5 times the one of the RANS model.

4.1.2 Combustion analysis

In contrast to the mixture formation, the combustion can in fact be validated by means of the pressure trace from the measurement data. The integrated net heat release, obtained from said pressure trace according to Chapter 3, is provided in Figure 4.8 for the RANS, LES and DES simulations.

The RANS model provides accurate results for the ignition delay. The slope of the graph between 720 and 740 degrees is however slightly underestimated. The LES, on the other hand, predicts a more realistic slope for the heat release compared to the experiment. This suggests that the more uniform and stoichiometric mixture formation positively influences the burning speed of the flame. Both values significantly overestimate the total heat release at 840 degrees by as much as 20%. This disagreement is revisited further on in the report.

As the LES resolves most of the fluctuations instead of modeling them, the model is able to better predict the turbulent burning speed of the flame. This is visible in Figure 4.9, where the flame fronts

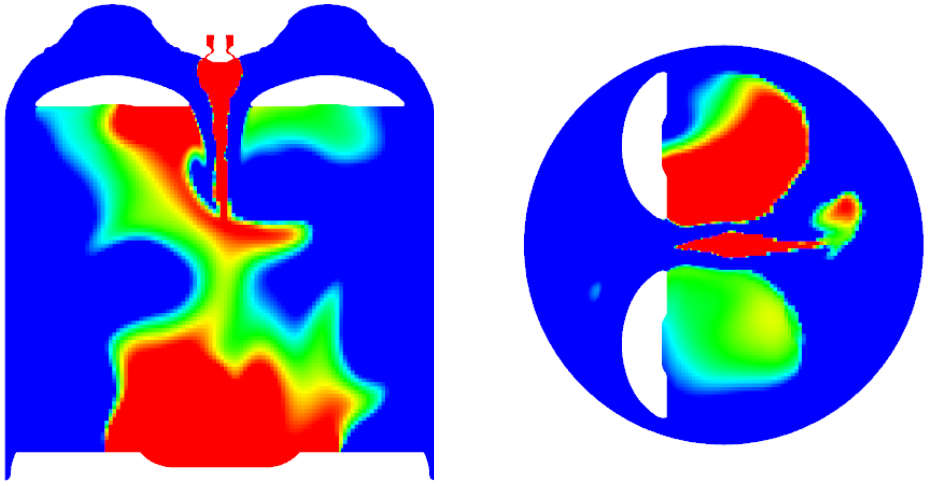

(a) RANS RNG k-ε

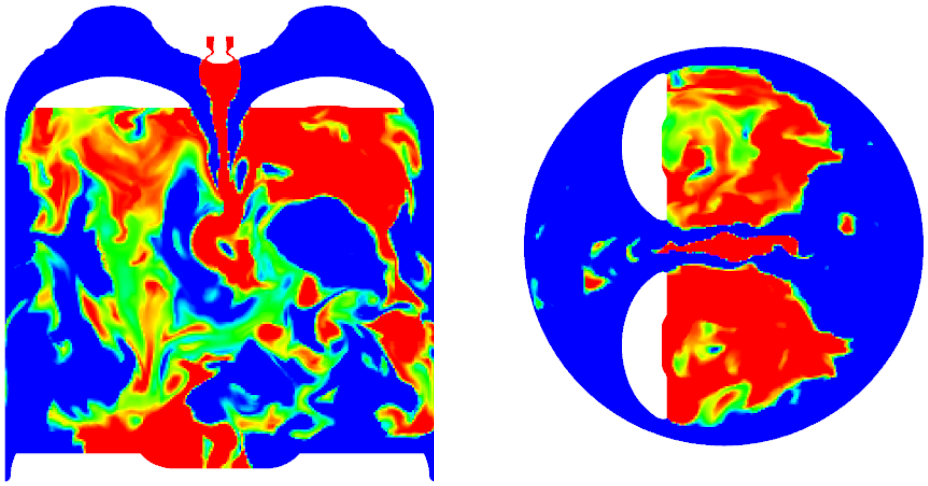

(b) Dynamic Smagorinsky LES

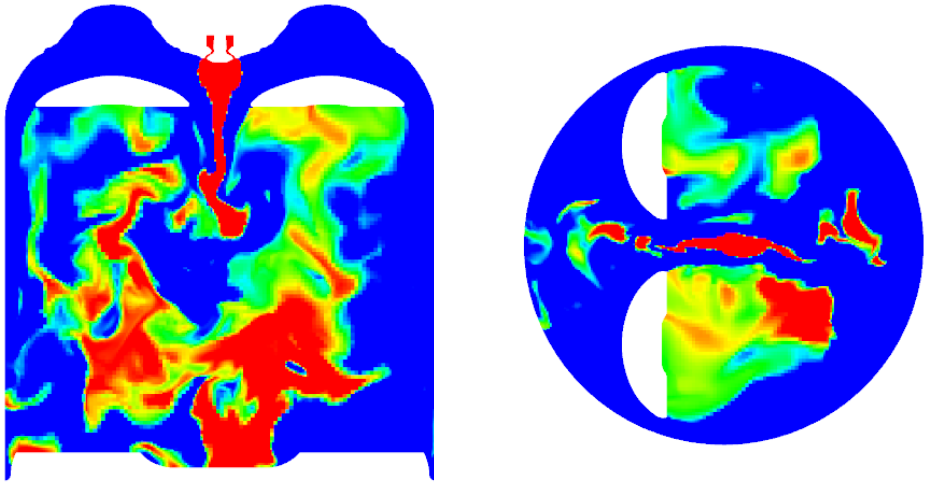

(c) Delayed DES

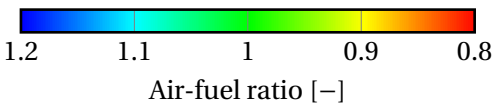

Figure 4.7: Comparison of spatial λ distribution at 480 degrees produced by different turbulence models

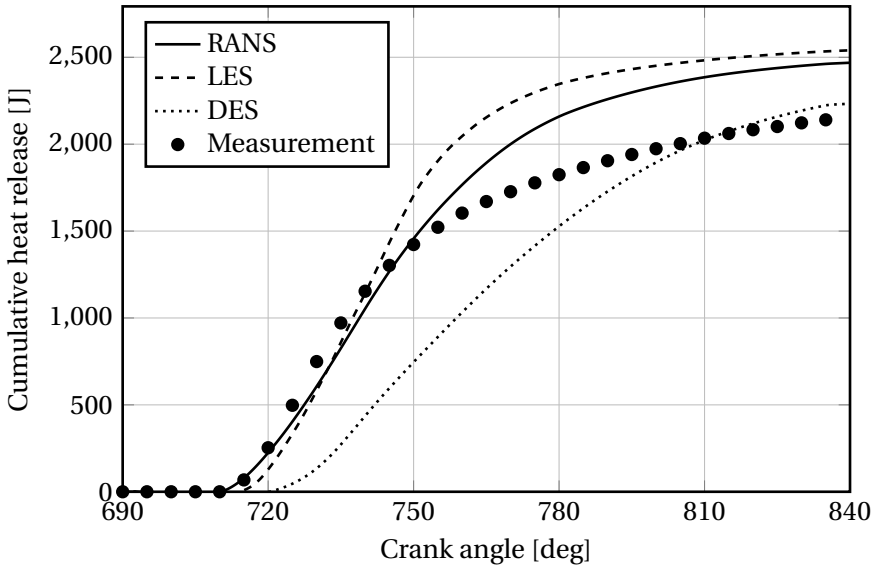

Figure 4.8: Cumulative net heat release for different turbulence models

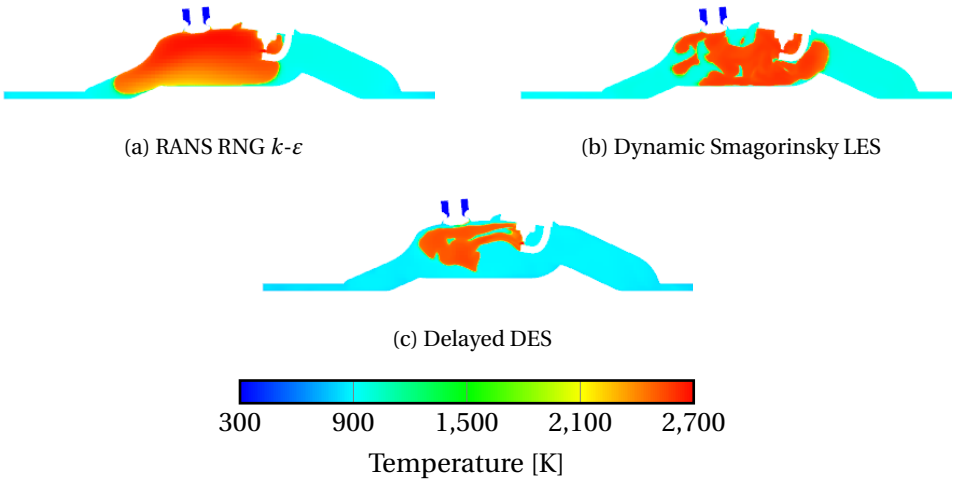

(a) RANS RNG k-ε

(b) Dynamic Smagorinsky LES

(c) Delayed DES

Figure 4.9: Comparison of flame wrinkling at 720 degrees for different turbulence models

produced by the three turbulence models are shown. The flames in Figures 4.9a and 4.9b are almost equal in size, suggesting that they both predict the same laminar flame speed. A wrinkled flame however burns faster than a laminar one, suggesting that the RANS model again underestimates the presence of small scale structures.

The DES proved to be an advantageous choice for the mixture formation, but in terms of combustion it does not predict the correct trend. Both the ignition delay and the heat release are poorly estimated, and the large difference at the end of combustion suggests that not all the fuel mass has been consumed. The flame front in Figure 4.9c does not correspond to the other two turbulence models, and the flame only propagates to the left of the spark plug. This unexpected result is most probably due to the way the model switches between RANS and LES. Figure 4.10 shows a section of the combustion chamber in which the LES mode has been indicated. Red areas in the plot refer to the zones in which the DES model switches to LES, while the blue regions refer to RANS. Intermediate values of the LES mode are determined by Equation (2.12) based on the information of viscosity, in order to postpone the transition in boundary layers and prohibit grid-induced separation. It seems, though, that the model misinterprets several regions in the flow domain, and the DES thus triggers transition from RANS to LES in very odd places. After investigation of the results, it can be concluded

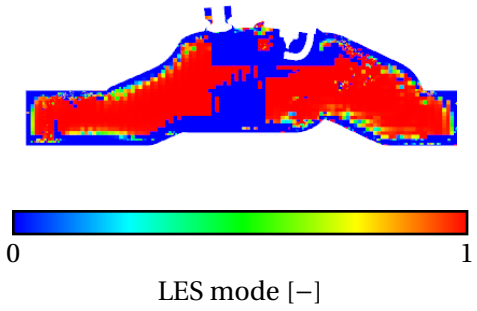

Figure 4.10: Local LES regions for the DDES turbulence model (0 is full RANS, 1 is full LES)

Table 4.2: Time consumption of turbulence models during combustion (690 to 840 degrees)

Model	**Wall time [h]**	**CPU**	**Rel. cost [%]**
RANS	57.7	144	100
LES	207.9	240	601
DES	81.3	192	188

that the switches are not connected to the AMR regions, nor to the flame position. The mismatch between RANS and LES on the flame dynamics are however large enough to render the model useless for the prediction of the combustion in this particular case.

Computational times for all three models during the combustion are given in Table 4.2. Similarly to the gas exchange simulation, the LES is several times more expensive than the RANS model. In conclusion, the best model choice for the simulation of both mixture formation and combustion is the RANS RNG k-ϵ model, as it predicts the combustion reasonably well and consumes less than 20% of the total wall time of the LES. The Delayed DES, although designed to control the switch between RANS and LES, produces abrupt transitions that lead to a poor prediction of the heat release and is therefore neglected for further use.

4.2 Schmidt number sensitivity

The turbulent Schmidt number, introduced in Chapter 3, is a parameter that relates the turbulent eddy viscosity to the eddy diffusivity. The results from the turbulence model study in Section 4.1 suggest that the RANS model is not able to predict the turbulent mixing as well as the scale-resolving simulations. Modifying the turbulent Schmidt number, and therefore altering the dominance of the diffusion occurring in the smallest scales of the flow, influences the mixture formation and, eventually, also the combustion. A sensitivity analysis was carried out, where Sc_t was varied from CONVERGE's default value of 0.78 in a decreasing fashion, thus promoting the turbulent mixing. The results for the λ distribution at the start of combustion are shown in Figure 4.11. Note that the solid line, representing the original value, corresponds to the solid line in Figure 4.6.

It is immediately apparent that the lowest Schmidt number of 0.4 produces a much more homogeneous mixture, having a large peak exactly at $\lambda = 1$, and a smaller spread into the lean and rich regimes. The value of $Sc_t = 0.6$ is fairly similar to the default for the rich regions, and shows less lean pockets. The spread is reduced from $\lambda = 1.9$ to $\lambda = 1.7$, but the magnitude and position of the peak (aside from a small dip at 0.95) is mostly unaffected.

The influence of the same turbulent Schmidt numbers on the combustion is shown in Figure 4.12. The close-to-stoichiometric mixture of $Sc_t = 0.4$ shows a peculiar trend that reminds of engine knock, where the heat release from the burned to the unburned region is so large that the mixture auto-ignites. Indeed, when examining Figure 4.13, the position of the flame at the three given time steps indicates the presence of knock. Consider the left part of each subfigure, which is located in the

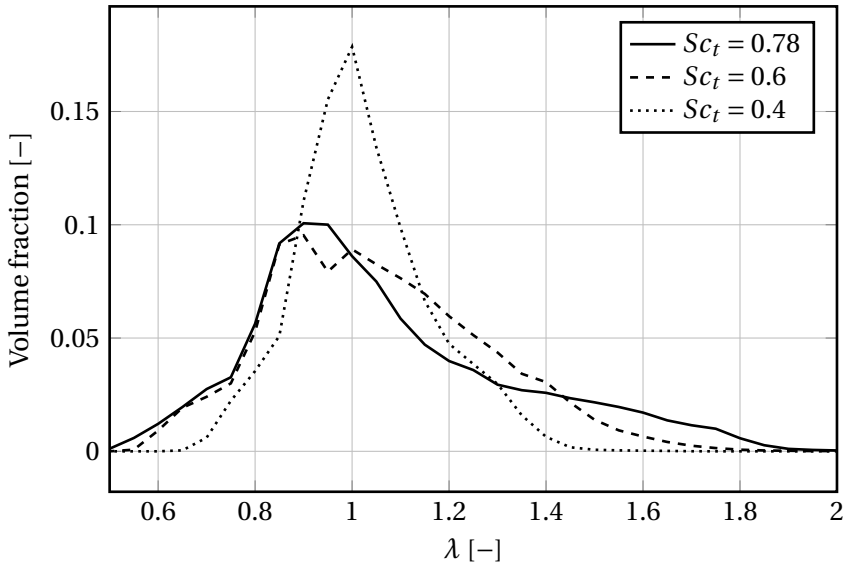

Figure 4.11: Distribution of air-fuel ratio at spark discharge for different values of the turbulent Schmidt number

crevice between the piston and the cylinder head at the intake side. At this location, the flame propagates in a gradual fashion, and the combustion behaves normally. The right part, referring to the crevice on the exhaust side, shows a gradual increase from 718 to 720 degrees, but the flame rapidly expands until it has filled the entire cross-section at 722 degrees. The abrupt increase in flame surface is related to the steep heat release profile in Figure 4.12. It is known that engine knock is accelerated with increased stiochiometry [Gallo, 2016], and the large difference between the mixture formation of $Sc_t = 0.4$ and $Sc_t = 0.6$ suggests that the threshold for knock has indeed been reached.

While the difference in mixture formation influences the burning speed, the difference between the curves in Figure 4.12 is however too large for the stoichiometry to be the only reason. Consider Figure 4.14, where the flame surface for the three turbulent Schmidt numbers is made visible and colored by air-fuel ratio. The position of the flame is expanding rapidly as the turbulent Schmidt number decreases, but the local distribution of fuel in Figure 4.14b is still very inhomogeneous. It was shown before that the flame speed is maximum at a slightly rich air-fuel ratio of $\lambda = 0.93$, and deteriorating fast in lean regions. The larger value of Sc_t in Figure 4.14a has a more favorable distribution with less lean zones, but the flame propagates much more slowly.

Referring back to the definition of gradient transport in turbulent flames, the turbulent Schmidt number does indeed have an influence on the turbulent transport term in Equation (2.22). The underlying assumptions for these premixed combustion models are single-step chemistry and a linear relation between temperature and the mass fractions of the reactive species [Veynante *et al.*, 1997]. Even though the SAGE model does not rely directly on the modeling of gradient transport of the progress variable, the fact that it is related to the turbulent transport of reactive species could be the reason why the turbulent Schmidt number influences the combustion so significantly.

The question remains if the turbulent transport in the engine occurs based on gradient or countergradient diffusion. Equations (2.23) and (2.24) allow to calculate a preliminary estimate of the Bray number based on the turbulent intensity u', integral lengthscale L, laminar flame speed u_L and thickness ℓ_f. The former two are known from the RANS turbulence model, the latter two from the 1D FlameMaster calculation. The heat release parameter τ can be computed by assuming a burned gas temperature of 2600 K and an unburned gas temperature between 700 and 900 K[(7)]. The value for the flame heat release factor thus ranges between $1.89 \leq \tau \leq 2.71$, with the largest one being critical.

[(7)] The unburned gas temperature changes between the spark discharge and the end of the cycle due to both compression of the gas by the piston and heat exchange from the burned to the unburned region.

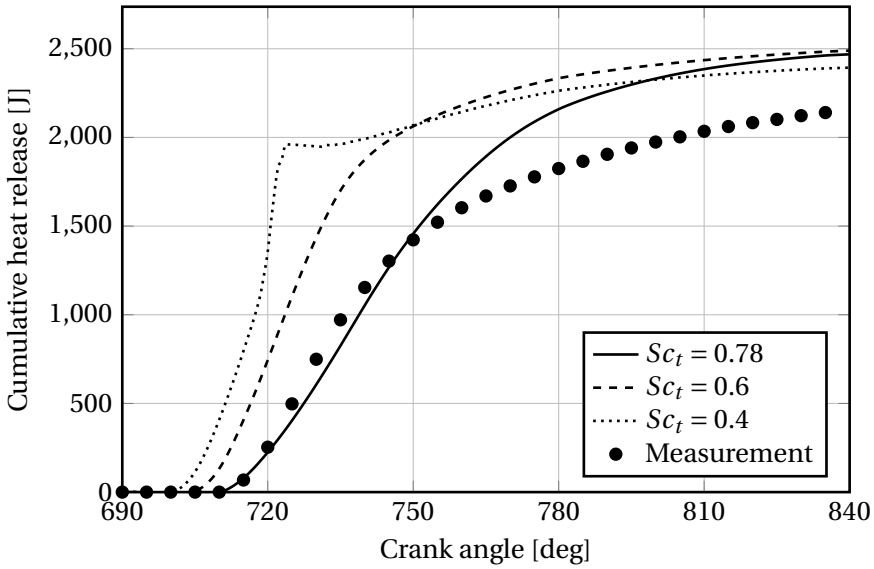

Figure 4.12: Cumulative net heat release for different values of the turbulent Schmidt number

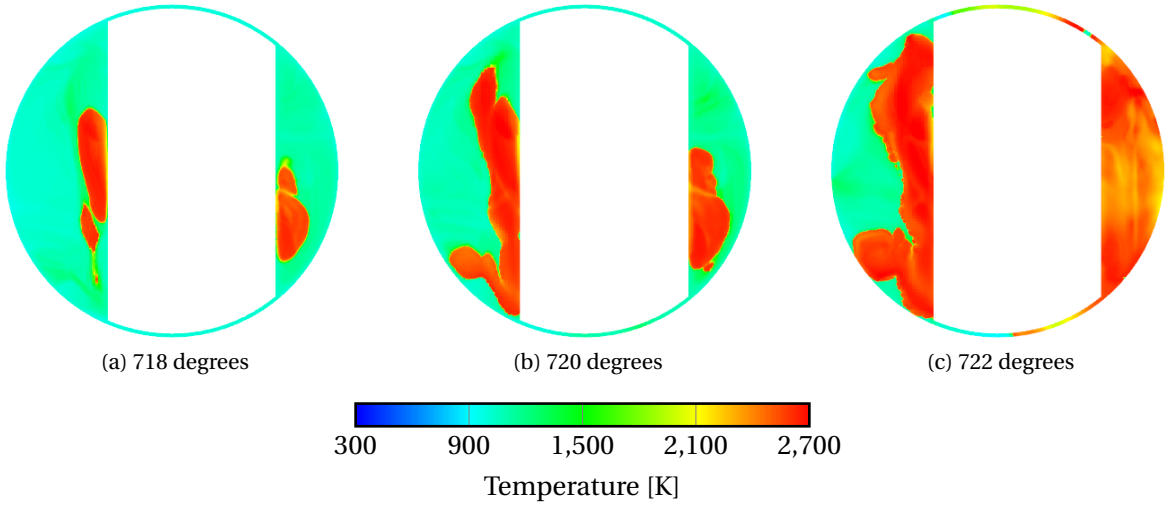

(a) 718 degrees (b) 720 degrees (c) 722 degrees

Figure 4.13: Flame position at different crank angles for $Sc_t = 0.4$ (the white region indicates volume outside the combustion chamber)

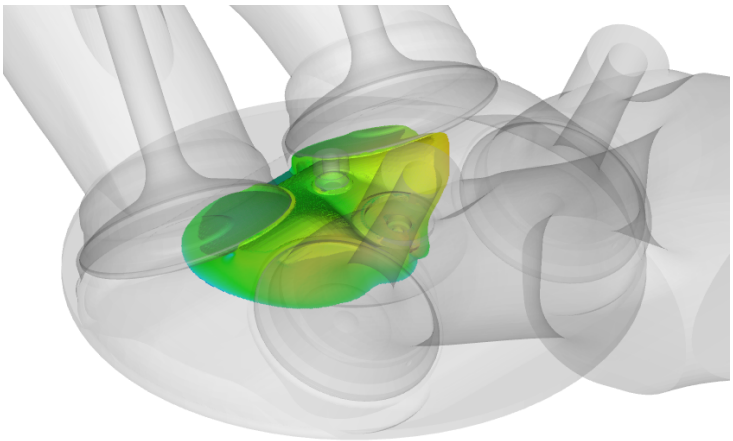

(a) $Sc_t = 0.78$

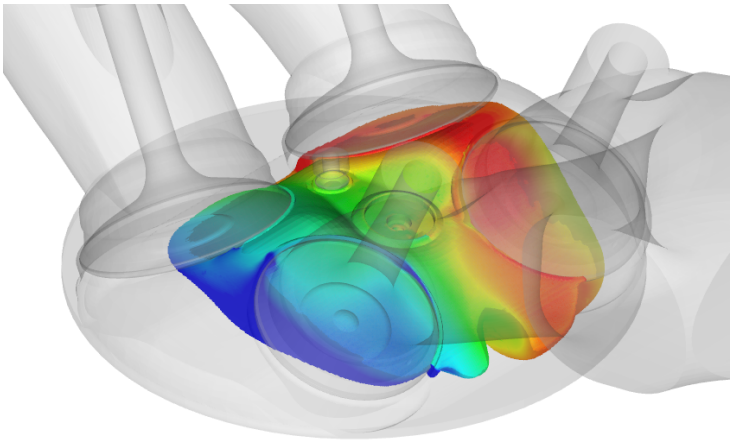

(b) $Sc_t = 0.6$

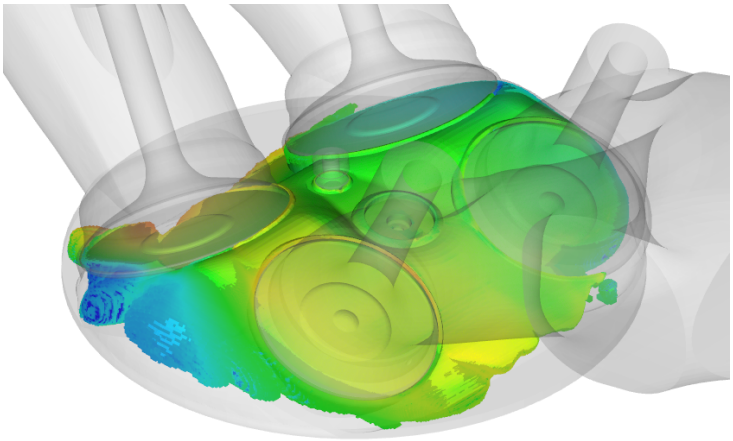

(c) $Sc_t = 0.4$

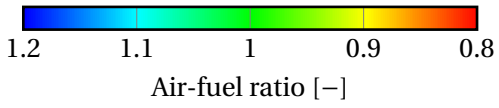

Figure 4.14: Flame position at 720 degrees for different values of the turbulent Schmidt number

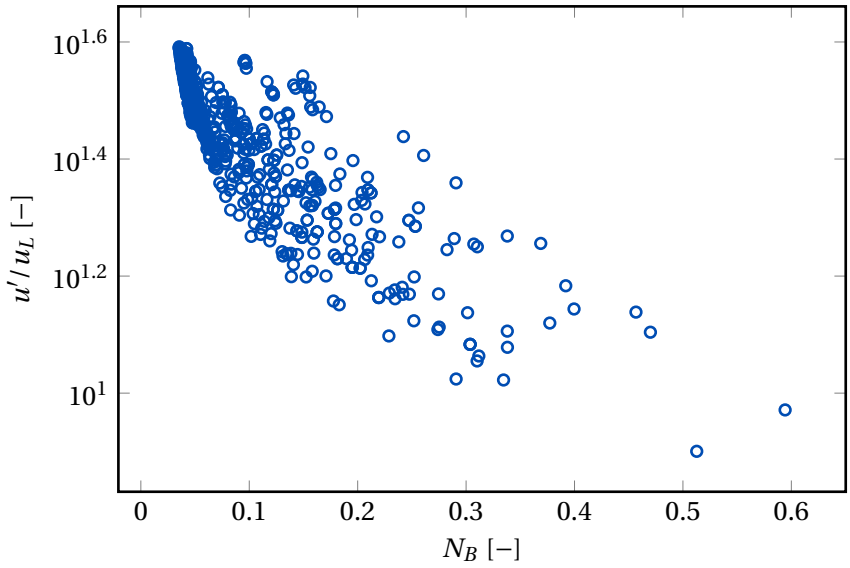

Figure 4.15: Bray number distribution at spark discharge

The resulting distribution of Bray numbers can be seen in Figure 4.15, where the ordinate was made consistent with the Borghi diagram. It can be seen that, in particular for this operating condition, the Bray number is very low, indicating the prevalence of gradient transport, and thus the confirmation that the turbulent Schmidt number affects the burning speed of the flame. It will however be shown that this is not the case for the entire engine envelope such that, at lower rpm, countergradient transport is prevalent and the influence of the turbulent Schmidt number on the combustion speed might be reduced.

At this point it is impossible to establish the 'correct' value of the Schmidt number for this particular engine configuration and operating condition without additional experimental data. The heat release trace of the LES in Figure 4.8 indicated that the LES is able to predict a realistic flame speed, and therefore the choice of 0.78 seems to be valid. The RANS results however underpredicted the slope of the heat release, suggesting that the predictivity of the model can be optimized by choosing a lower Schmidt number. The value of $Sc_t = 0.6$ shows an increase in slope compared to the default one, and the prediction can possibly be further enhanced by calibration of the lower heating value.

In conclusion, this analysis has shown that the turbulent Schmidt number is a very sensitive parameter, and extreme values of 0.2 and 3.5 are not uncommon in literature [Gualtieri *et al.*, 2017; Tominaga and Stathopoulos, 2007]. Even though it is unsure whether the mixture formation is improved by altering it, the pattern in the change of flame speed suggests that the turbulent Schmidt number can be used as a calibration parameter for in-cylinder simulations to obtain the correct heat release rate. This topic is revisited in Section 4.5.

4.3 Cyclic variations

As described by Twellmeyer *et al.* [2017], the initial flow field of the simulation (or experiment, for that matter) greatly influences the turbulence during the induction events and, eventually, also the mixture formation. The effect of initialization was analyzed by running three consecutive cycles with the RANS turbulence model and SAGE active.

The results for the in-cylinder pressure during gas exchange are identical for all cycles. Larger discrepancies can be found in the λ distribution, as shown in Figure 4.16. All three cycles have approximately the same spread, but the maximum volume fractions and their corresponding air-fuel ratio differ substantially. For an increasing amount of cycles, the mixture formation is more concentrated, forming a sharper peak. The value of the air-fuel ratio at this maximum is however not consistent.

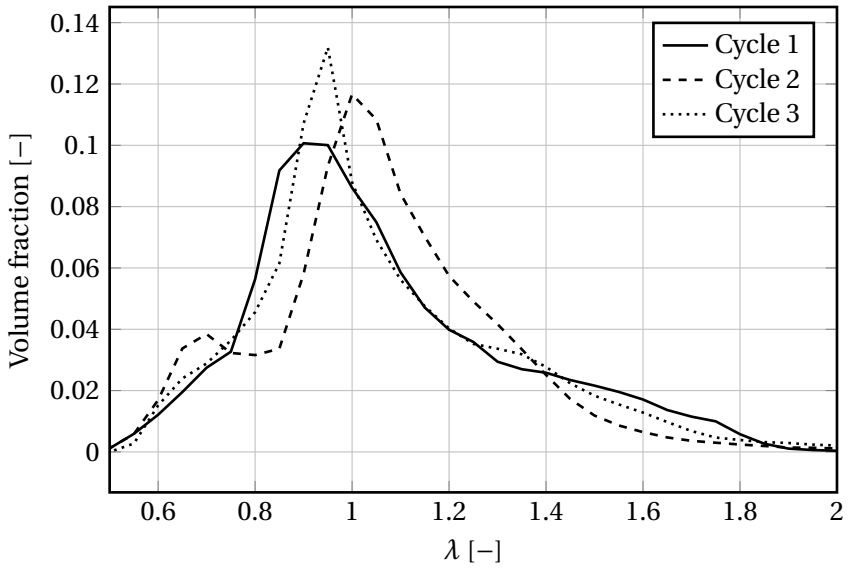

Figure 4.16: Distribution of air-fuel ratio at spark discharge for three consecutive RANS cycles

The difference in mixture formation leads to a difference in combustion. In Figure 4.17, the net heat release of the three cycles is shown against the measurement data. The simulated total heat release at the end of each cycle is almost identical, indicating that the initialization of the field is not the reason for the overestimation of the heat release.

Two major differences between the cycles can be noticed in the heat release trace. First of all, the second and third cycle have a longer ignition delay than the first one. The second and perhaps most apparent difference is the change in slope between cycle one and two between 730 and 750 degrees. Interestingly, the second and third cycle are almost identical, showing very little disagreement over the power expansion stroke. In fact, the difference is smaller than the cyclic variability from Figure 3.4.

The best way to look at the difference in ignition delay is by considering the spatial distribution in air-fuel ratio at the moment the heat release trace becomes non-zero. Figure 4.18 shows the distribution in three different clip planes at 710 degrees, corresponding to the last 10 degrees before ignition top dead center is reached. The deviations between the first cycle and the two remaining ones are much more apparent. Especially the region around the spark plug for cycle one is dominated by a large stoichiometric zone. The second and third cycle show a spark plug on the edge of a very rich pocket that, under the influence of the tumbling motion, propagates to the right. Referring back to Figure 3.18, the stoichiometric zone features a faster laminar burning speed, explaining why the ignition delay is slightly shorter for the first cycle. By the time the piston moves to 730 degrees, the flame has grown and traveled far enough to reach zones with a sufficient amount of mixing such that the overall distribution from Figure 4.16 becomes more important, which is in favor of the second and third cycle.

The similarity of the air-fuel ratio in the second and third cycle is reflected in the flame position. The clip planes colored by temperature in Figure 4.19 show that flame has a similar shape and temperature. More importantly, it can be noticed that the flame in the first cycle is propagating in an odd fashion. The flame travels towards the intake port, rather than expanding uniformly from the spark plug in cycle two and three.

Aside from the laminar burning speed, the air-fuel ratio also influences the temperature of the burned gases and, again, also the heat release to the environment. Consider the flame position in Figure 4.19b and the λ distribution in Figure 4.20. The contour between the stoichiometric and rich zone in the latter can clearly be discerned in the temperature of the burned gas. This happens because the rich zone does not possess enough oxidizer to completely burn all the fuel. The part of the fuel that remains acts as a coolant for the burned gases and takes up some of the expelled heat without igniting [Heywood, 1988]. The result is a locally colder flame.

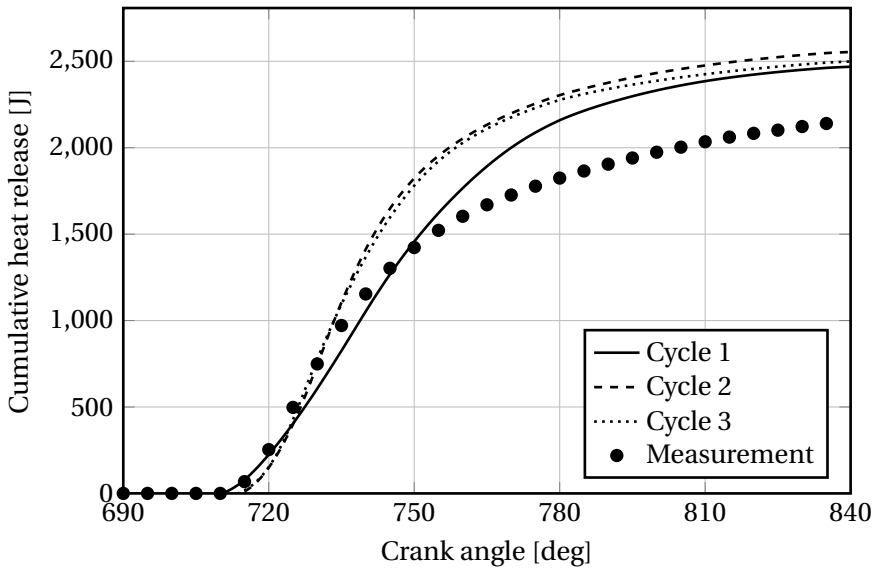

Figure 4.17: Cumulative net heat release for three consecutive RANS cycles

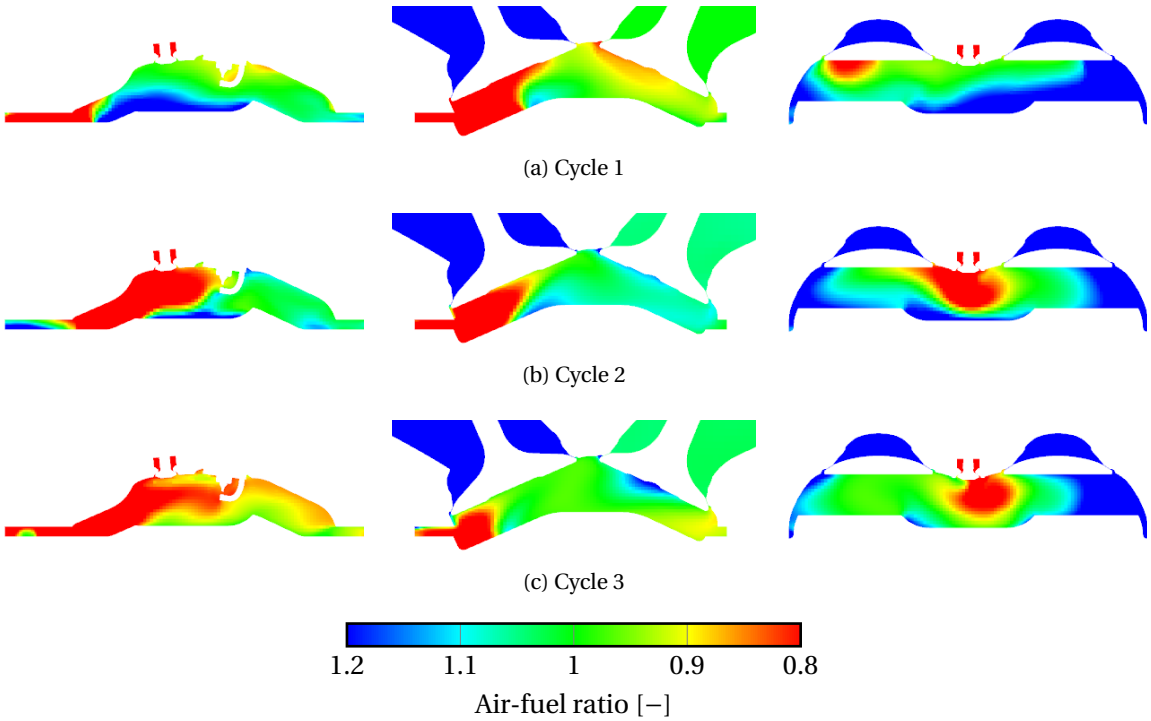

Figure 4.18: Comparison of spatial λ distribution at 710 degrees for three consecutive RANS cycles

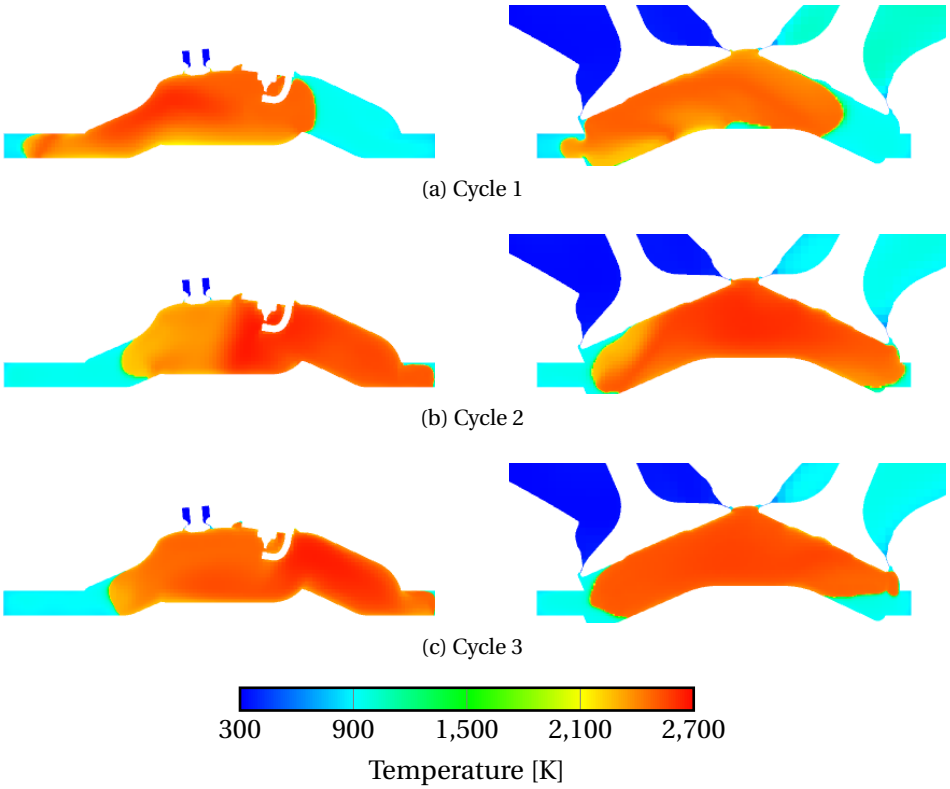

Figure 4.19: Flame position at 740 degrees (20 degrees after TDC) for three consecutive RANS cycles

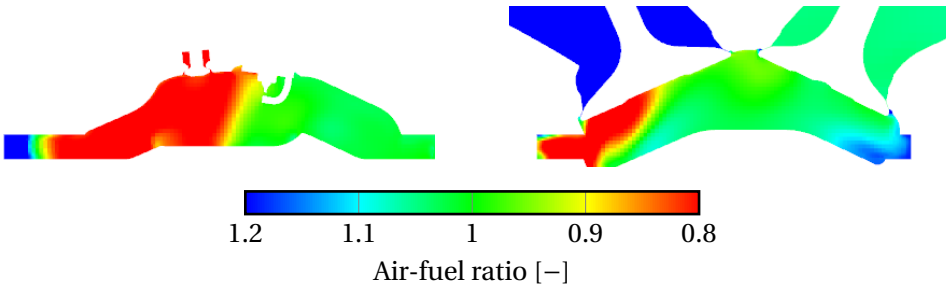

Figure 4.20: Distribution of stoichiometry for the second cycle at 740 degrees

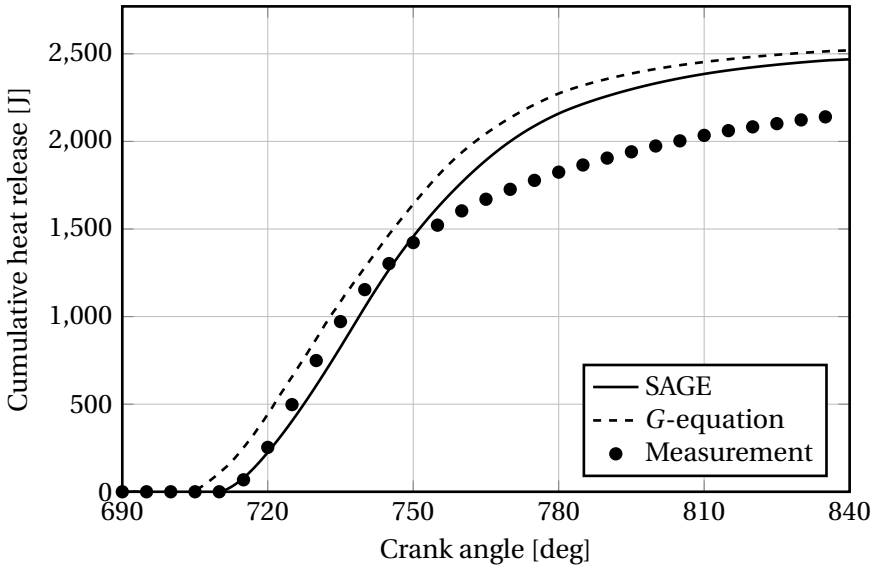

Figure 4.21: Cumulative net heat release for SAGE and *G*-equation combustion

In conclusion, it has been proven that the first cycle still contains some effects of initialization. As the second cycle uses the results of the first one, the predictions are improved and the pressure trace converges to its nominal value within the cyclic variability of the engine. In addition, the latter cycles produced a longer ignition delay and a faster laminar flame speed, but it is unclear if this can be generalized to other cases.

4.4 Combustion model study

The characteristics of a predictive combustion model should include a correct estimate of the ignition delay and the burning speed of the flame. Both properties can be judged by looking at the heat release trace. Ideally, the spark timing and fuel properties should thus be left unaltered with respect to the measurement.

The analyses in the previous sections consistently used the SAGE detailed chemistry solver rather than the *G*-equation. Figure 4.21 shows why this choice has been made at the start of the chapter. The net heat release trace shows that the ignition delay of the *G*-equation method is greatly underestimated. The flame speed of both methods is however fairly similar. The reason for this could be an improper setting of the *G*-equation coefficients prior to the simulation. Although, a second and perhaps more logical explanation is given by Figure 4.22. Here, the flame regime diagram is depicted using the results from a SAGE run at the time of discharge. The scatterplot refers to the cells contained in a sphere of 1 cm diameter around the spark plug. The high rotational speed of the engine results in such strong turbulence at the time of discharge that the points lie deep into the thin reaction zones. Part of the data even exceeds the quenching limit of Meneveau and Poinsot [1991], such that the eddies locally reach into the flame front and affect the burning speed. As introduced in Chapter 2, the assumptions behind the mathematical formulation of the *G*-equation are not valid in this region. There is no characteristic burning velocity that can be used by the model, potentially leading to the underestimation of the ignition delay.

Aside from the position of the data on the diagram, the shape of the scatterplot also entails information about the turbulent structures at the time of discharge. As mentioned before, the data have been plotted for all cells that lie within 5 mm of the spark plug, thus influencing the start-up of the flame. As the distance from the spark plug becomes larger, the lengthscale increases and the scatterplot expands towards and across the quenching limit. Over the entire range of points, the vertical spread is quite large, indicating that the turbulence is very anisotropic and might influence the initial flame propagation.

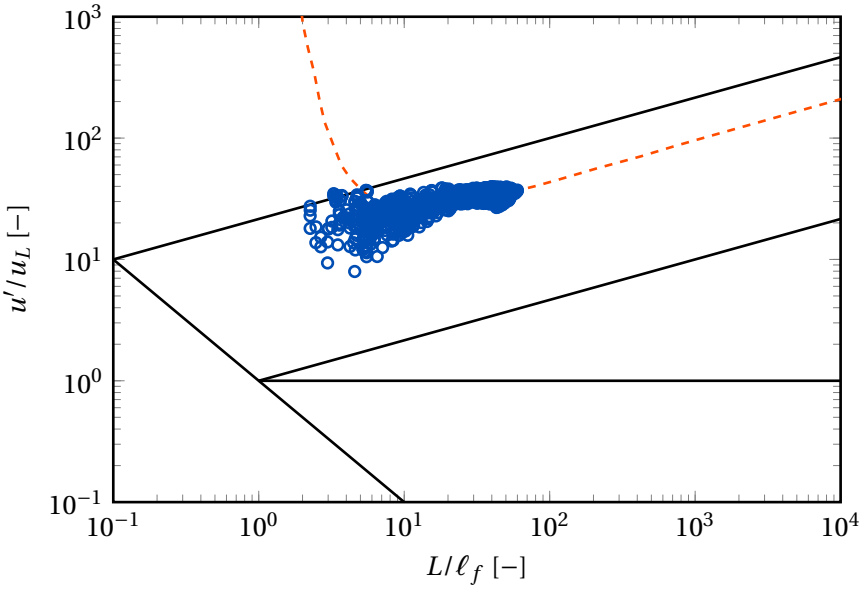

Figure 4.22: Premixed flame regime diagram at spark discharge obtained with SAGE

Table 4.3: Time consumption of combustion models

Model	**Wall time [h]**	**CPU**	**Rel. cost [%]**
SAGE	57.7	144	100
G-equation	95.1	144	165

Despite the claims from literature that the *G*-equation model requires less computational time, the opposite is in fact true. Both combustion models used the same setting for the computational grid, but the time spent on the combustion window is 60% longer than the one of SAGE using the same number of CPU, as is indicated in Table 4.3. It should be noted that this is probably a consequence of the implementation of the *G*-equation in CONVERGE. The model activates the Chemical Equilibrium solver inside the flame to calculate the species concentrations of the burned gas. The formulation is however known to be more expensive than the SAGE solver, and the adaptive mesh refinement within the flame probably causes the Chemical Equilibrium to be active in too many cells.

This brief combustion model analysis leads to the conclusion that the *G*-equation model is error-prone for the current operating conditions of the engine. It is safer to assume that the SAGE model, being a detailed chemistry solver, in conjunction with the GRI-Mech 3.0 reaction mechanism provides accurate results in a computationally efficient manner.

4.5 Synthesis

Sections 4.1 to 4.4 provided important information on several parameters that largely affect the simulation of mixture formation and combustion. This section aims to summarize all findings and use them to construct an ad hoc calibration of simulation methodology for the heat release trace.

It was shown that the RANS turbulence model is optimal in terms of accuracy and computational cost, but lacks some of the molecular diffusion that could be achieved by more expensive turbulence models. A way to compensate this problem, influencing the homogeneity of the mixture and thus the burning speed of the flame, is the modification of the turbulent Schmidt number. The samples should be taken from the second cycle, as it was shown that the first one can still contain initialization errors. Finally, the best choice for combustion modeling is the SAGE detailed chemistry solver, as its prediction for the ignition delay is very similar to the measured value.

A persisting issue in the simulation results that have been shown so far is the value of the total heat release at the end of the simulated cycle (840 degrees). Since the calibration of the boundary conditions in Chapter 3 was performed such that the simulation closely matches the experiment, it is unclear where the large deviation comes from. A possible error source could be the temperature condition imposed at the intake boundary. The value used in the simulation was established based on a reference 1D-CFD simulation. If, in reality, the temperature of the measurement turned out to be different, this would affect the amount of mass going into the cylinder[8]. As the mixture was calibrated for a stoichiometric air-fuel ratio, an excess mass of air would result in an excess of fuel as well. Consequently, the heat release is larger than expected. It should be noted, however, that the difference in heat release of 20% is so large that a drastic change in temperature is necessary. As the reference 1D-CFD simulation is closely related to this particular engine configuration, it is not likely that this is the only reason for the difference.

Another possible cause is an erroneous measurement of the lower heating value of the fuel. The LHV of natural gas fluctuates significantly between its dry and saturated states. On top of that, different ratings of the fuel exist throughout the world, and the species composition differs substantially between the different versions. Consequently, also the lower heating value is affected, introducing the risk of an inconsistent measurement.

Rather than investigating the effect of inlet temperature on the combustion, the choice was made to provide an ad hoc solution for the peak power operating point by calibrating the LHV until the proper heat release is reached. In fact, the lower heating value is commonly regarded as a calibration parameter for the simulation of combustion. The spark timing is preferably unaltered, as it is modified for each operating condition and would thus rely on calibration repeatedly. Instead, the LHV is a global parameter and remains unaltered between two engine speeds. The question however remains if the calibration at one particular engine speed is consistent with another one.

Figure 4.23 contains the heat release trace of the calibration. It shows the first and second cycle of a simulation with RANS turbulence, SAGE combustion, a turbulent Schmidt number equal to $Sc_t = 0.6$ and a lower heating value of 44.5 MJ/kg. The reduction in LHV allowed to decrease the total value of the net heat release, but as a consequence it also affected the slope of the trace between 720 and 750 degrees. A lower Schmidt number was therefore chosen to improve the mixing and increase the eddy diffusivity during combustion. A good agreement is obtained, that could potentially be further enhanced by slightly lower the turbulent Schmidt number even further. It is also interesting to note that the differences between the first and the second cycle, being a longer ignition delay and a steeper slope between 720 and 750 degrees, are consistent with the analysis of Section 4.3.

In order to judge the accuracy of the ad hoc solution, the species concentration can be assessed and compared to the measurement of CO_2 from Table 3.1. The change in species during combustion is depicted for the simulation in Figure 4.24. N_2, being an inert gas, is not shown in the diagram. It can be seen that the amount of CO_2 accounts for 10.7% of the total species mass, which is a very good estimate for the 10.9% that was obtained in the measurement. Furthermore, it can be noticed that not all oxygen and fuel is consumed, meaning that the combustion is incomplete. This means that the burning speed of the flame is inaccurately obtained, again suggesting that the turbulent Schmidt number could be slightly lowered as compensation.

While studying the results of the calibration, one should however keep in mind that, with modification of the LHV and Schmidt number, the underlying physical assumptions in the simulation move away from reality and the methodology should be considered less predictive. The sole purpose of the calibration in this section is therefore to underline that a meaningful estimate of the flame position and concentration of emissions can be obtained by providing an ad hoc solution. Whether or not this modification is consistent for other operating conditions is discussed in the next section.

[8] Assuming the ideal gas law ($p = \rho RT$) and the fact that the pressure is fixed by the measurement, a decrease in temperature implies an increase in density and thus species mass.

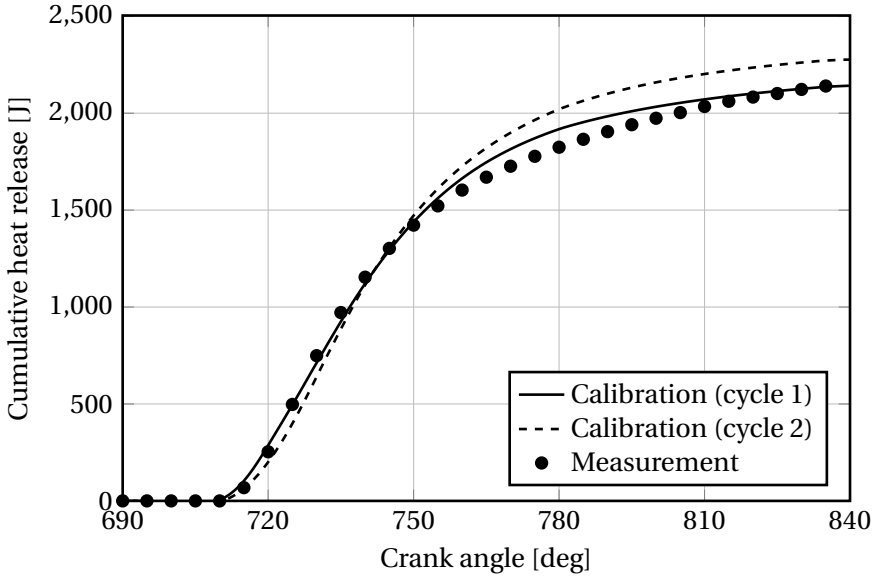

Figure 4.23: Calibration of the net heat release during combustion

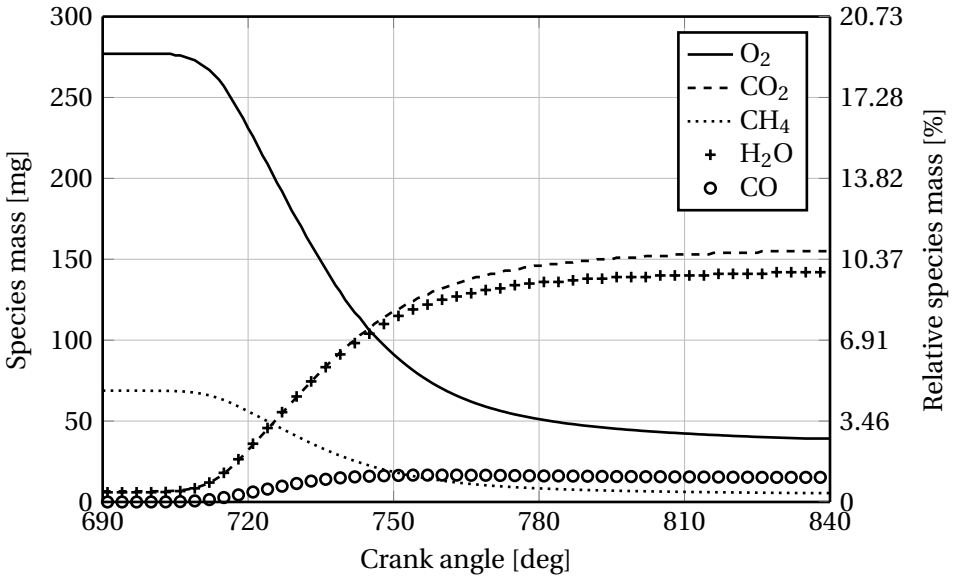

Figure 4.24: Change in species concentration during combustion of the second calibrated cycle

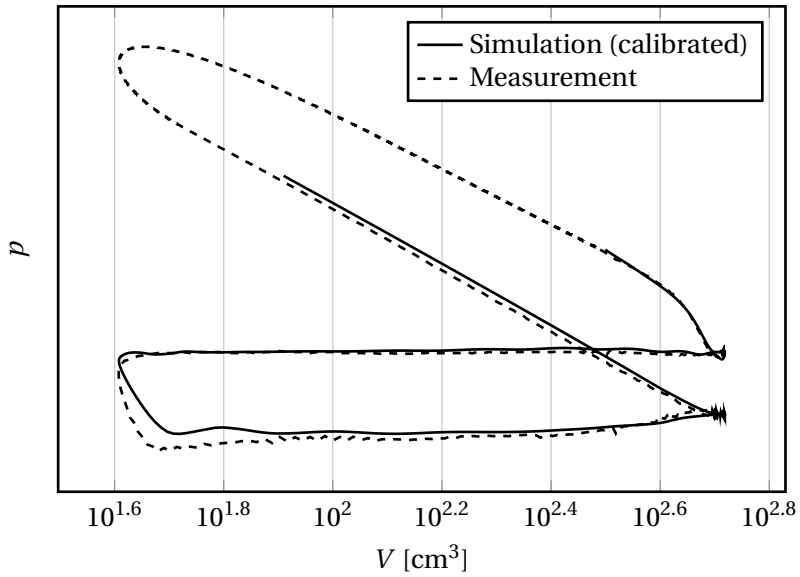

Figure 4.25: Calibrated log-log diagram of the in-cylinder pressure at 2000 rpm

4.6 Operating envelope

For the simulation of the second operating point at 2000 rpm and 2 bar mean effective pressure, the same sequence of steps was repeated as it was performed for the 6500 rpm engine speed. Figure 4.25 shows the measured and calibrated in-cylinder pressure trace. The modification of the intake pressure at 2000 rpm was consistent with the one of Chapter 3. Instead, the exhaust pressure required a different scaling. It should be noted that the logarithmic scale of the graph exaggerates the difference between simulation and measurement. The same criteria, namely the pressures at top dead center, bottom dead center and during compression, were used to modify the boundary conditions. Even though a close match was obtained for these parameters, the eventual pressure at the start of combustion is slightly too large. In addition, a time delay was measured also for this operating point, influencing the slope of the compression stroke on the diagram. After correction, a good agreement of the slope was obtained.

Other considerations for the 2000 rpm condition included modification of the measurement conditions in Table 3.1. In addition, the model of the spark in Figure 3.17 was altered such that the total time of 1 ms was retained[(9)]. As a consequence, the length was changed from 39 to 12 crank angle degrees. Finally, due to a shift in valve timings, the simulation was started at 90 degrees instead of 120 to fully capture the exhaust valve opening.

The evolution of the mixture formation is presented in Figure 4.26, and compared against the 6500 rpm run at the spark discharge in Figure 4.27. Even though the mean value of the air-fuel ratio moves to its stoichiometric value, the mixture stays predominantly rich from 600 degrees onward. Compared to the 6500 rpm point, the mixture is more homogeneous, which can be explained by the fact that there is more physical time for the air and fuel to be fully premixed. The less dominant tumble ratio in the chamber and the higher pressure ratio between injector and combustion chamber also imply that the fuel jet, rather than being inclined along the flow direction, goes straight down and impinges on the piston. This is visible in Figure 4.28, and the difference with Figure 4.4a is very clear. After impinging on the piston, the fuel jet breaks up and mixes with the air. As a consequence, the mixture is smooth and gradual at 2000 rpm, while the peak power case featured a discontinuity in the temporal development of the mixture formation.

The combustion simulation, including the modified Schmidt number of 0.6 and the LHV of the 6500 rpm case, is visualized in Figure 4.29. Indeed, as most claims from literature already indicated,

[(9)] The length of the spark discharge does in general not change with the rotational speed of the engine.

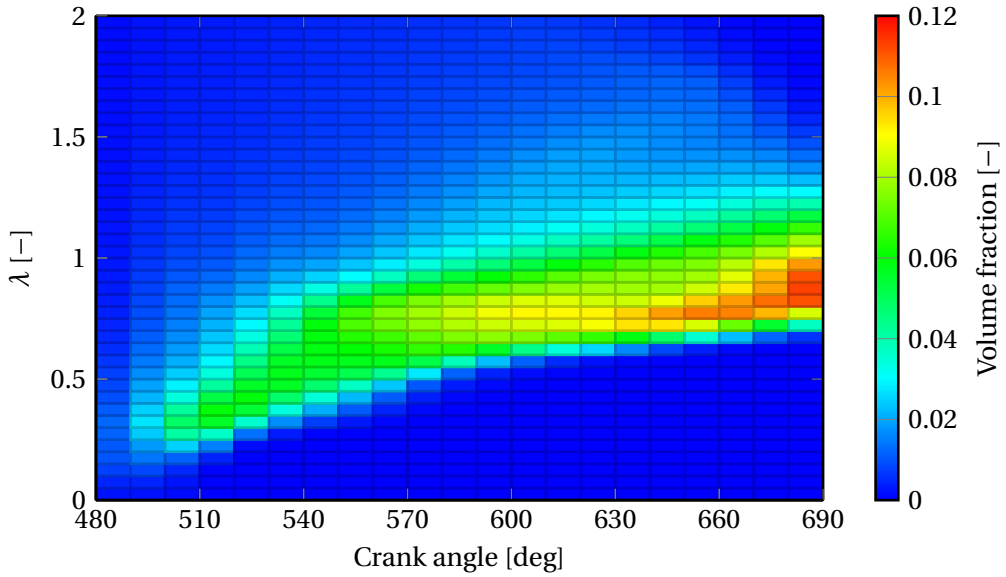

Figure 4.26: Contour plot of λ distribution obtained with RANS turbulence modeling during the intake and compression stroke at part load

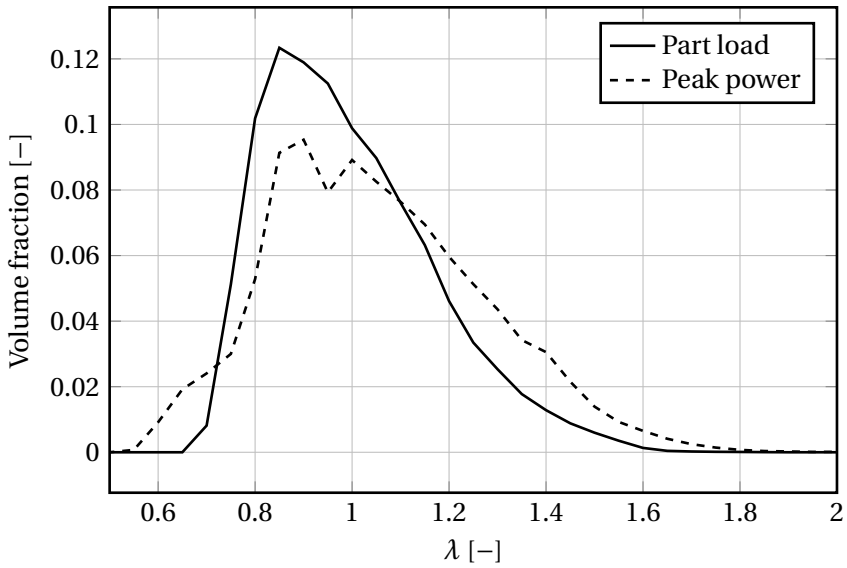

Figure 4.27: Distribution of air-fuel ratio at spark discharge for the two operating points

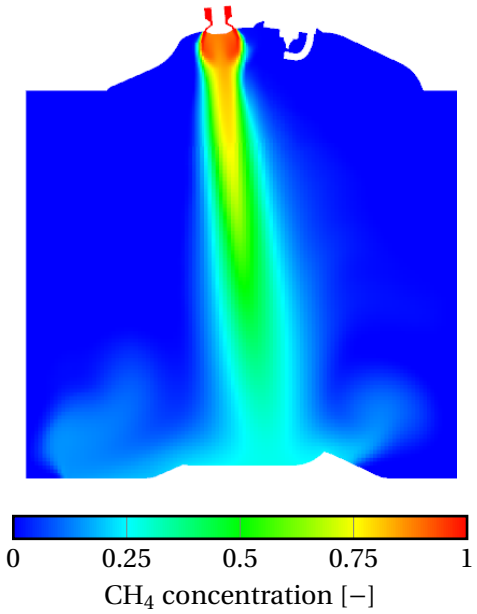

Figure 4.28: Fuel penetration at 490 degrees at part load

the calibration is not consistent for different engine speeds. While the SAGE model provided good approximations for the ignition delay at peak power, the one of the part load condition is significantly underestimated. Furthermore, the flame speed is too high, and the heat release is overestimated as well. In order to obtain a close approximation of the flame position and emissions of this operating condition, the calibration needs to be revisited.

Finally, a comparison is provided for the flame regimes of the 2000 rpm case against the data in Figure 4.22. The flame front at part load is clearly less influenced by the turbulence around the spark plug. Most of the data can be classified as corrugated flamelets. The closer to the spark plug, though, the more the cells move towards the wrinkled flamelets, and the cluster of cells at the electrode boundary even penetrates into the laminar flame regime. The same spread of the data however, remains, such that the turbulent fluctuations are still quite inhomogeneous at the time of spark discharge. It is interesting to note that, with all data points below the quenching limit, the implementation of the G-equation combustion model would make more sense at this particular operating point. Indeed, Cornolti [2015] investigated the G-equation at 1500 rpm and found that it produced excellent agreement for his engine test case. Hence, there exists a limit for the rotational speed at which the model can be used.

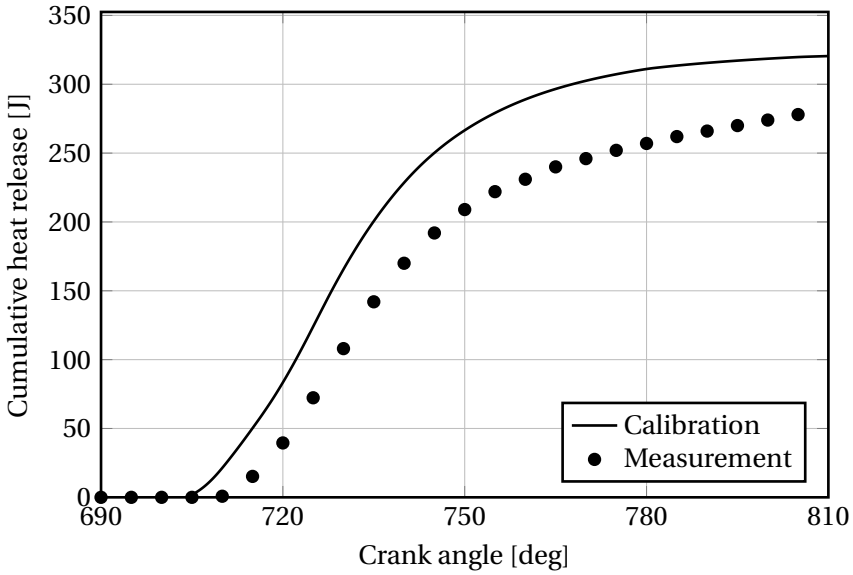

Figure 4.29: Cumulative net heat release at part load

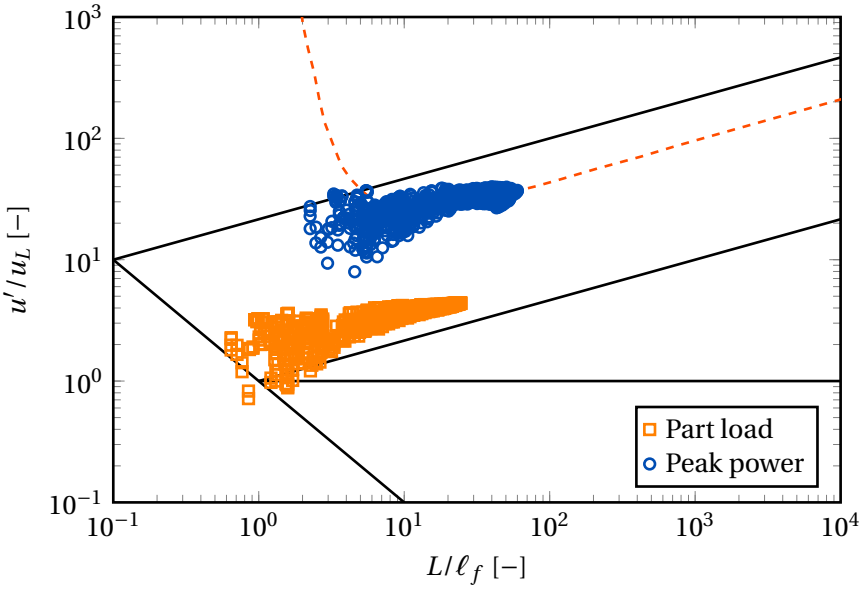

Figure 4.30: Premixed flame regime diagram at spark discharge comparing the two operating points

5

Conclusions and recommendations

After having seen all the results in Chapter 4, the main findings of the project can now be stated. In Section 5.1, the main conclusions are presented and used to provide an answer to the research questions of Section 2.4. The open questions are addressed in Section 5.2, where recommendations are given for the continuation of this particular project, or the start-up of a similar one.

5.1 Conclusions

Three different conditions that affect the mixture formation of CNG direct-injection have been investigated. The choice of turbulence model proved to be an important factor in the simulation. The Reynolds-Averaged Navier-Stokes model underestimated the diffusion on molecular level, resulting in a mixture that was less homogeneous than the other model choices. The Large Eddy Simulation and the hybrid Detached Eddy Simulation models provided more plausible results for the air-fuel mixing. It was not possible to validate the fuel distribution with measurement data, but the more realistic trend of the LES for the heat release trace suggests that the model provides a better estimate than the RANS model. The DES provided LES accuracy while greatly reducing the computational time, such that it became the preferred choice for the development of the mixture formation. During combustion, however, the DES limiter made very abrupt changes between RANS and LES-like regions, such that the results for the pressure trace were compromised. The conclusion, as well as the answer to the the first subquestion of research question 1, is thus that, even though the DES is the best option for the mixture formation, it does not provide reliable results for the entire combustion cycle, and the RANS approach should still be preferred.

The turbulent Schmidt number, controlling the relation between turbulent viscosity and eddy diffusivity, influenced the homogeneity of the mixture formation and the combustion speed to a large extent. Literature already suggested that the range of the turbulent Schmidt number is very large and locally varying, such that it is impossible to establish a universal value. It was found that lowering the value by too much increases the knock tendency of the engine in the simulation, while large values underestimate the homogeneity of the mixture in conjunction with RANS simulations. Finally, it was shown that RANS simulations can be calibrated by choosing an optimal value of the turbulent Schmidt number that approximates the correct flame speed and ignition delay. It is however not possible to generalize this value to other operating conditions.

Cyclic variability was investigated by running three consecutive cycles with the same boundary condition settings. It can be concluded that the first cycle still contains initialization errors, while the second and third cycle converge to a similar state within the allowed variability of the measurement. The local distribution of air and fuel in the combustion chamber resulted in a longer ignition delay for the latter cycles, but also an increased burning speed. The same trend was observed for the cyclic variability of a calibrated simulation, which leads to the assumption that it can be generalized.

The choice of combustion model was limited by the interaction between the turbulence around the spark plug and the laminar flame properties at peak power. An initial run with the SAGE detailed chemistry model showed that the data exceeded the quenching limit of Meneveau and Poinsot [1991], such that the laminar flamelet assumption, being the basis of many simplified premixed combustion models, is not valid. Indeed, the *G*-equation combustion model proved to be ineffective to predict the correct ignition delay at peak power compared to SAGE. In addition, due to the coupling of the *G*-equation with the Chemical Equilibrium model inside the flame, the simulation was significantly slower than the chemistry model with 53 species and 325 elementary reaction, such that there was no reason to prefer the *G*-equation model over SAGE. It should be noted that this conclusion is made for the peak power operating point, while it was shown that at lower engine speeds the *G*-equation might be justified due to the more favorable level of turbulence.

After obtaining the results at the peak power condition, the same settings were applied to the part load condition at 2000 rpm. It was found that any calibration of the turbulent Schmidt number and the lower heating value of the fuel performed at 6500 rpm was not consistent with the 2000 rpm engine speed. Individual ad hoc calibrations can be performed per operating condition, although being very time consuming for the simulation engineer. Rather than providing ad hoc fixes for the turbulent Schmidt number, Large Eddy Simulations could potentially provide better, more predictive results, although computational requirements come to play in this case.

The main conclusion of the report is that the several simplified modeling approaches for turbulence and combustion modeling in the engineering industry may be able to provide adequate results, but the accuracy relies on calibration of the simulation against measurement data. When, in the future, there is easier access to computational resources, more sophisticated models can be used to further improve the predictivity of the methodology.

5.2 Recommendations

For readers who wish to investigate a similar engine configuration using 3D-CFD, a few recommendations are included. These suggestions are related to both the methodology development outlined in Chapter 3, as well as potential improvements to the engine geometry.

5.2.1 Improving the methodology

While constructing a converged grid in Chapter 3, it was found that the in-cylinder pressure trace was hardly influenced by the grid size. Even with base sizes of 4 mm, very precise results could be obtained. Indeed, the pressure is a global variable rather than a local one, and it is relatively independent of the geometrical features of the engine chamber such that coarse grids can be used. In fact, engine performance simulations employing a 1D-CFD approach are most often used to predict engine characteristics. They discretize the computational domain using pipes in one direction only, and the reduction of computational time allows to compute several engine loads in just a few minutes.

Knowing this, the calibration of the boundary conditions in Chapter 3 could be improved and accelerated. The calibration procedure in this report is susceptible to the relation between exhaust pressure and rotational speed. For the purpose of the analysis, it was sufficient to capture the fluctuations in the signal during the time the valves were open. It was however shown that the calibrations of the exhaust pressure for the two operating points were inconsistent with each other. The coupling of a 1D-CFD model to CONVERGE could improve the prediction of the pressure trace and therefore improve the predictivity of the 3D-CFD model.

5.2.2 Improving the engine

As mentioned earlier, the engine that is studied in this report is a converted gasoline engine that is currently in series production. In the gasoline version, the injector was originally placed between the intake valves rather than sitting next to the spark plug. The piston bowl in Figure 5.1 has been

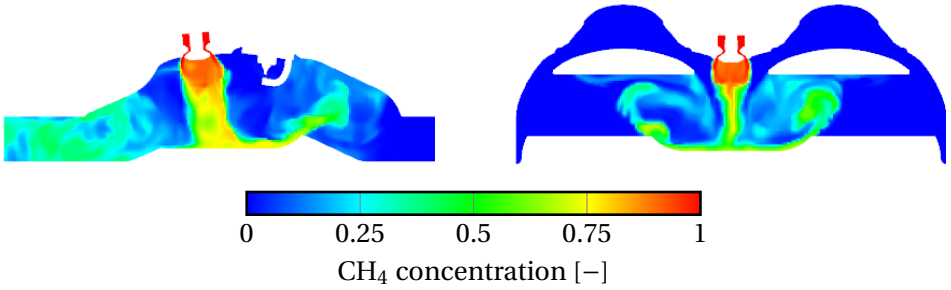

Figure 5.1: Influence of the piston geometry on the impinging fuel jet at 390 degrees (LES)

designed correspondingly to direct the impinging fuel jet upwards, thus promoting mixing by stirring the fuel with the tumbling air. For practicality, the injector for this prototype was placed elsewhere, such that the shape of the piston does not assist the mixing anymore. The homogeneity of the air and the fuel could thus possibly be influenced by redesigning the bowl shape in favor of the current injector placement, or by mounting the injector in the original series production location.

After repositioning the injector, the location of the spark plug could potentially be optimized as well. When considering Figures 4.19b and 4.19c, the flame position reveals that the fuel in the left-most part of the combustion chamber underneath the intake port is not consumed yet. The high temperatures of the unburned gas increase the risk on engine knock in that particular location. Since the flame speed of CNG is lower than the one of gasoline, this problem was not present yet in the series production gasoline engine. The risk on knock could be alleviated by mounting the spark plug centrally in the chamber, such that the flame propagates evenly in all directions.

Bibliography

Ameen, M. M., Yang, X., Kuo, T.-W., and Som, S. (2017). Using LES to simulate cycle-to-cycle variablity during the gas exchange process. *Proceedings of the ASME 2017 Internal Combustion Engine Division Fall Technical Conference*.

Banerjee, S. and Rutland, C. (2012). On LES grid criteria for spray induced turbulence. *SAE Technical Paper*, **2012-01-0141**.

Bardina, J., Ferziger, J., and Reynolds, W. (1980). Improved subgrid models for large eddy simulation. In *13th Fluid and Plasmadynamics Conference. Snowmass, CO, U.S.A.*

Battistoni, M., Mariani, F., Risi, F., and Poggiani, C. (2015). Combustion cfd modeling of a spark ignited optical access engine fueled with gasoline and ethanol. *Energy Procedia*, **82**, 424–431.

Boger, M., Veynante, D., Boughanem, H., and Trouvé, A. (1998). Direct numerical simulation analysis of flame surface density concept for large eddy simulation of turbulent premixed combustion. *Symposium on Combustion*, **27**(1), 917–925.

Boretti, A. (2017). The future of the internal combustion engine after "diesel-gate". *SAE Technical Paper*, **2017-28-1993**.

Borghi, R. (1985). *Recent advances in the aerospace sciences*, chapter 7: On the structure and morphology of turbulent premixed flames. Plenum Press.

Brandl, A., Pfitzner, M., Mooney, J. D., Durst, B., and Kern, W. (2005). Comparison of combustion models and assessment of their applicability to the simulation of premixed turbulent combustion in IC-engines. *Flow, Turbulence and Combustion*, **75**, 335–350.

Bray, K. N. C. (1995). Turbulent transport in flames. *Proceedings: Mathematical and Physical Sciences*, **451**(1941), 231–256.

Buhl, S., Dietzsch, F., Buhl, C., and Hasse, C. (2017). Comparative study of turbulence models for scale-resolving simulations of internal combustion engine flows. *Computers and Fluids*, **156**, 66–80.

Cant, S. (2011). *Turbulent combustion modeling*, chapter 4: RANS and LES modeling of premixed turbulent combustion. Springer Science.

Catania, A. E., Dongiovanni, C., Mittica, A., Negri, C., and Spessa, E. (1996). Turbulence spectrum investigation in a di diesel engine with a reentrant combustion bowl and a helical inlet port. *SAE Technical Paper*, **962019**.

Chala, G. T., Aziz, A. R. A., and Hagos, F. Y. (2017). Combined effect of boost pressure and injection timing on the performance and combustion of CNG in a DI spark ignition engine. *International Journal of Automotive Technology*, **18**(1), 85–96.

Choi, M., Song, J., and Park, S. (2016). Modeling of the fuel injection and combustion process in a CNG direct injection engine. *Fuel*, **179**, 168–178.

Cokljat, D., Caridi, D., Link, G., Lechner, R., and Menter, F. R. (2009). Embedded LES methodology for general-purpose CFD solvers. *Proceedings of the 6th International Symposium on Turbulence and Shear Flow Phenomena*, pages 1191–1196.

Convergent Science (2018). Applications: Internal combustion engines. Retrieved on 22/05/2018 at `https://convergecfd.com/about/company-profile`.

Cornolti, L. (2015). *CFD modelling of turbulent premixed combustion in spark-ignition engines*. Ph.D. thesis, Politecnico di Milano.

Deardorff, J. (1970). A numerical study of three-dimensional turbulent channel flow at large Reynolds numbers. *Journal of Fluid Mechanics*, **41**(2), 453–480.

Fluent Inc. (2006). FLUENT 6.3 user's guide. Unpublished user manual retrieved on 30/04/2018 at `https://www.sharcnet.ca/Software/Fluent6/index.htm`.

Gallo, A. (2016). *Development of a methodology for the knock prediction in highly charged SI engines by the use of 3D-CFD simulation*. Master's thesis, Politecnico di Torino. Graduate project at Porsche Engineering Services GmbH.

Gatsky, T. B. and Bonnet, J.-P. (2009). *Compressibility, turbulence and high-speed flow*. Elsevier Science.

Germano, M., Piomelli, U., Moin, P., and Cabot, W. H. (1991). A dynamic subgrid-scale eddy viscosity model. *Physics of Fluids*, **3**, 1760–1765.

Gualtieri, C., Angeloudis, A., Bombardelli, F., Jha, S., and Stoesser, T. (2017). On the values of the turbulent schmidt number in environmental flows. *Fluids*, **2**.

Halstead, M. P., Kirsch, L. J., and Quinn, C. P. (1977). The autoignition of hydrocarbon fuels at high temperatures and pressures - fitting of a mathematical model. *Combustion and Flame*, **30**, 45–60.

Han, Z. and Reitz, R. D. (1996). Interpretation of k-ε computed turbulence length-scale predictions for engine flows. *Twenty-Sixth Symposium (International) on Combustion/The Combustion Institute*, pages 2717–2723.

Heywood, J. B. (1988). *Internal combustion engine fundamentals*. McGraw-Hill, Inc.

Hickel, S. (2016). CFD for aerospace engineers. Unpublished lecture slides, Faculty of Aerospace Engineering, Delft University of Technology.

Hickel, S. and Hulshoff, S. (2017). CFD 3: Large eddy simulation. Unpublished lecture slides, Faculty of Aerospace Engineering, Delft University of Technology.

Idicheria, C. A. and Pickett, L. M. (2007). Quantitative mixing measurements in a vaporizing diesel spray by Rayleigh imaging. *SAE Technical Paper*, **2007-01-0647**.

Joelsson, T., Yu, R., and Bai, X. S. (2011). Large eddy simulation of turbulent flows in a laboratory reciprocating engine. In *Progress in hybrid RANS-LES modelling*, pages 461–470. Springer.

Jones, W. P. and Launder, B. E. (1972). The prediction of laminarization with a two-equation model of turbulence. *International Journal of Heat and Mass Transfer*, **15**(2), 301–314.

Kawai, S. and Larsson, J. (2012). Wall-modeling in large eddy simulation: length scales, grid resolution, and accuracy. *Physics of Fluids*, **24**.

Khan, M. I., Yasmin, T., and Shakoor, A. (2015). Technical overview of compressed natural gas as a transportation fuel. *Renewable and Sustainable Energy Reviews*, **51**, 785–797.

Kolmogorov, A. (1941). The local structure of turbulence in incompressible viscous fluid for very large Reynolds' numbers. *Doklady Akademiia Nauk SSSR*, **30**, 301–305.

Kong, S., Han, Z., and Reitz, R. (1995). The development and application of a diesel ignition and combustion model for multidimensional engine simulation. *SAE Technical Paper*, **950278**.

Lin, W. (2010). *Large-eddy simulation of premixed turbulent combustion using flame surface density approach*. Ph.D. thesis, University of Toronto.

Lund, C. M. (1978). *HCT - a general computer program for calculating time-dependent phenomena involving one-dimesnional hydrodynamics, transport, and detailed chemical kinetics*. Lawrence Livermore Laboratory, University of California.

Magnussen, B. F. and Hjertager, B. H. (1976). On mathematical models of turbulent combustion with special emphasis on soot formation and combustion. *Proceedings of the Combustion Institute*, **16**(1), 719–729.

Manz, A. (2016). *Modeling of end-gas autoignition for knock prediction in gasoline engines*. Ph.D. thesis, Technische Universität Brandenburg.

Marble, F. E. and Broadwell, J. E. (1977). The coherent flame model for turbulent chemical reactions. Technical report, Purdue University. Project Squid (TRW-9-PV).

Meneveau, C. and Poinsot, T. (1991). Stretching and quenching of flamelets in premixed turbulent combustion. *Combustion and Flame*, **86**, 311–332.

Menter, F. R. (1993). Zonal two-equation k-ω turbulence models for aerodynamic flows. In *23rd Fluid Dynamics, Plasmadynamics, and Lasers Conference. Orlando, FL, U.S.A.*

Menter, F. R. and Egorov, Y. (2005). A scale-adaptive simulation model using two-equation models. In *43rd AIAA Aerospace Sciences Meeting and Exhibit. Reno, Nevada, U.S.A.*

Menter, F. R., Kuntz, M., and Langtry, R. (2003). Ten years of industrial experience with the SST turbulence model. *Turbulence, Heat and Mass transfer*, **4**, 625–632.

Menter, F. R., Schtuetze, J., and Gritskevich, M. (2011). Global vs. zonal approaches in hybrid RANS-LES turbulence modelling. In *Progress in hybrid RANS-LES modelling*, pages 15–28. Springer.

Merker, G. P., Schwarz, C., Stiesch, G., and Otto, F. (2006). *Simulating combustion*. Springer.

Mitianiec, W. (2012). Ignition of cng mixtures in spark ignition engines. *Journal of KONES Powertrain and Transport*, **19**(3), 297–304.

Nguyen, T. M., Proch, F., Wlokas, I., and Kempf, A. M. (2016). Large eddy simulation of an internal combustion engine using an efficient immersed boundary technique. *Flow, Turbulence and Combustion*, **97**, 191–230.

NGV Depot (2018). Cng tank type 1. Retrieved on 29/11/2018 at `http://www.ngvdepot.com/cng-tank-type-1-d-o-t-13-5-gge-3600-psi-56-7x16-ngv/`.

Nicoud, F. and Ducros, F. (1999). Subgrid-scale stress modelling based on the square of the velocity gradient tensor. *Flow, Turbulence and Combustion*, **62**(3), 183–200.

Nicoud, F., Toda, H. B., Cabrit, O., Bose, S., and Lee, J. (2011). Using singular values to build a subgrid-scale model for large eddy simulations. *Physics of Fluids*, **23**.

Peters, N. (2000). *Turbulent combustion*. Cambridge University Press.

Pickett, L. M., Manin, J., Genzale, C. L., Siebers, D. L., Musculus, M. P. B., and Idicheria, C. A. (2011). Relationship between diesel fuel spray vapor penetration/dispersion and local fuel mixture fraction. *SAE Technical Paper*, **2011-01-0686**.

Pitsch, H. (2006). Large-eddy simulation of turbulent combustion. *Annual Review of Fluid Mechanics*, **38**, 453–482.

Pitsch, H. (2018). FlameMaster: A C++ computer program for 0D combustion and 1D laminar flame calculations.

Pope, S. B. (2000). *Turbulent flows*. Cambridge University Press.

Pope, S. B. (2004). Ten questions concerning the large-eddy simulation of turbulent flows. *New Journal of Physics*, **6**, 35–58.

Reynolds, O. (1895). On the dynamical theory of incompressible viscous fluids and the determination of the criterion. *Philosophical Transactions of the Royal Society of London A: Mathematical, Physical and Engineering Sciences*, **186**, 123–164.

Seboldt, D., Lejsek, D., Wentsch, M., and Chiodi, M. (2016). Numerical and experimental studies on mixture formation with an outward-opening nozzle in a SI engine with CNG-DI. *SAE Technical Paper*, **2016-01-0801**.

Sellmann, J., Lai, J., Kempf, A. M., and Chakraborty, N. (2016). Flame surface density based modelling of head-on quenching of turbulent premixed flames. *Proceedings of the Combustion Institute*, **36**, 1817–1825.

Sethian, J. A. (1996). A fast marching level set method for monotonically advancing fronts. *Proceedings of the National Academy of Sciences USA*, **93**, 1591–1595.

Shur, M. L., Spalart, P. R., Strelets, M., and Travin, A. (2008). Direct numerical simulation of large-eddy-break-up devices a boundary layer. *International Journal of Heat and Fluid Flow*, **29**(6), 1638–1649.

Smagorinsky, J. (1963). General circulation experiments with the primitive equations. *Monthly Weather Review*, **91**(3), 99–164.

Smith, G. P., Golden, D. M., Frenklach, M., Moriarty, N. W., Eiteneer, B., Goldenberg, M., Bowman, C. T., Hanson, R. K., Song, S., Gardine, W. C., Lissianski, V. V., and Qin, Z. (2018). Gri-mech. Retrieved on 16/10/2018 at `http://www.me.berkeley.edu/gri_mech/`.

Som, S., Senecal, P. K., and Pomraning, E. (2012). Comparison of RANS and LES turbulence models against constant volume diesel experiments. *ILASS Americas*. 24th conference on liquid atomization and spray systems.

Spalart, P. R. and Allmaras, S. R. (1994). A one-equation turbulence model for aerodynamic flows. *Recherche Aerospatiale*, **1**, 5–21.

Spalart, P. R., Jou, W. H., Strelets, M., and Allmaras, S. R. (1997). Comments on the feasibility of LES for wings, and on a hybrid RANS/LES approach. *Advance in DNS/LES, 1st AFOSR International Conference on DNS/LES*.

Spalart, P. R., Strelets, M., and Travin, A. (2006a). Direct numerical simulation of large-eddy-break-up devices in a boundary layer. *International Journal of Heat and Fluid Flow*, **27**, 902–910.

Spalart, P. R., Deck, S., Shur, M. L., and Squires, K. D. (2006b). A new version of detached-eddy simulation, resistant to ambiguous grid densities. *Theory of Computational Fluid Dynamics*, **20**, 181–195.

Spina, E. F., Smits, A. J., and Robinson, S. K. (1994). The physics of supersonic turbulent boundary layers. *Annual Review of Fluid Mechanics*, **26**, 287–319.

Stolz, S. and Adams, N. A. (1999). An approximate deconvolution procedure for large-eddy simulation. *Physics of Fluids*, **11**, 1699–1701.

Tominaga, Y. and Stathopoulos, T. (2007). Turbulent schmidt numbers for cfd analysis with various types of flowfield. *Atmospheric Environment*, **41**, 8091–8099.

Twellmeyer, A., Kopple, F., and Weigand, B. (2017). Evaluating different measures to improve the numerical simulation of the mixture formation in a spark-ignition cng-di-engine. *SAE Technical Paper*, **2017-01-0567**.

Veynante, D., Trouvé, A., Bray, K. N. C., and Mantel, T. (1997). Gradient and counter-gradient scalar transport in turbulent premixed flames. *Journal of Fluid Mechanics*, **332**, 263–293.

Vreman, A. W. (2004). An eddy-viscosity subgrid-scale model for turbulent shear flow: algebraic theory and applications. *Physics of Fluids*, **16**(10), 3670–3681.

Wilcox, D. C. (1988). Reassessment of the scale determining equation for advanced turbulence models. *American Institute of Aeronautics and Astronautics Journal*, **26**(11), 1299–1310.

Williams, F. A. (1985). *The mathematics of combustion*, chapter Turbulent combustion. SIAM, Philadelphia.

Yakhot, V., Orswag, S. A., Tangham, S., Gatski, T. B., and Speziale, C. G. (1992). Development of turbulence models for shear flows by a double expansion technique. *Physics of Fluids*, **4**(7), 1510–1520.

Zanforlin, S. and Boretti, A. (2015). Numerical analysis of methane direct injection in a single-cylinder 250 cm^3 spark ignition engine. *Energy Procedia*, **81**, 883–896.

Ziemer, R. E., Tranter, W. H., and Fannin, D. R. (2013). *Signals and systems - continuous and discrete*. Pearson Education.

Zimont, V. L. and Biagioli, F. (2006). Gradient, counter-gradient transport and their transition in turbulent premixed flames. *Combustion Theory and Modeling*, **6**(1), 79–101.

Cover image courtesy of the Porsche AG Press Database